國 立 交 通 大 學

電信工程學系

博 士 論 文

使用標準矽製程整合 $90°$ 和 $180°$ 分合波器之
吉伯特微混頻器

Gilbert Micromixer with Integrated 90°/180°
Hybrids in Standard Si IC Process

研究生：曾聖哲

指導教授：孟慶宗

中 華 民 國 九 十 七 年 七 月

使用標準矽製程整合 90°和 180°分合波器之吉伯特
微混頻器

Gilbert Micromixer with Integrated 90°/180° Hybrids in Standard Si IC Process

研究生：曾聖哲　　　　　　　Student: Sheng-Che Tseng

指導教授：孟慶宗　博士　　　Advisor: Dr. Chinchun Meng

國立交通大學

電信工程學系

博士論文

A Dissertation
Submitted to Institute of Communication Engineering
College of Electrical Engineering
National Chiao Tung University
in Partial Fulfillment of the Requirements
for the Degree of Doctor of Philosophy
in
Communication Engineering
Hsinchu, Taiwan

2008 年 7 月

使用標準矽製程整合90°和180°分合波器之吉伯特微混頻器

學生:曾聖哲　　　　　　　　　　　　　　指導教授:孟慶宗博士

國立交通大學

電信工程學系博士班

摘　　　　　要

此論文中，以 0.35 毫米矽鍺雙載子互補式金氧半導體製程展示單端輸入輸出吉伯特微混頻器。因應寬頻操作，在微混頻器中頻級使用電阻回授式轉阻放大器，而在本地震盪級使用寬頻巴倫或是鼠徑耦合器來產生寬頻差動訊號。在研究中，這些微波被動元件儘管實作在具損耗、低阻抗(~10 歐姆·公分)的矽基板上，仍可產生很平衡的訊號。在第二章中，提出系統化的量測方式來評量混頻器每一級的頻率響應。

第三章中提出可調式、電抗式正交相位產生器，其具有定值阻抗、低損耗、雙頻帶實作和高正交相位精確度的特性。在所有頻率中，皆可達成正交相位輸出與輸入匹配；而在設計的兩個頻段中，達成相同振幅輸出。實作的 2.4/5.2 GHz 正交相位降頻器之輸出振幅差小於 1 %、相位差小於 1°；而實作的 2.4/5.7 GHz 單端頻譜升頻器具有高達 50 dB 單端頻譜抑制比。

第四章中，使用標準矽製程實作一個具有相位反轉器之寬頻鼠徑耦合器，並詳細地分析損耗狀態下的耦合器。將相位反轉器應用在鼠徑耦合器，不僅能增加頻寬，亦可提供等損耗的輸出路徑，以保持輸出平衡；而對稱式螺旋形共平面帶狀傳輸線不僅可以縮小耦合器大小，還可利於建造相位反轉器於其中一個螺旋形共平面帶狀傳輸線上。無失真具損耗的共平面帶狀傳輸線具有實數特性阻抗，使

得耦合器在中心頻率可達成匹配。此外,展示了應用此型態鼠徑耦合器之 2.5 到 13 GHz 寬頻微混頻器。

第五章中,實現整合本地震盪器級馬爾尚巴倫之寬頻混頻器,具有 15 dB 轉換增益,操作頻率在 3.5 到 14.5 GHz,此外,縮小化成塊元件馬爾尚之降頻器展示於超寬頻系統中,具有 15.5 dB 轉換增益。而第六章中,以耦合指數和特性阻抗來分析與設計傳統平面式馬爾尚巴倫與其變化型,此兩種型態在結構上具有雙重性,然而當兩種巴倫以相同特性阻抗設計時,新型態巴倫會較寬頻。此外,而在此章節分析中,發現只要實作在均質材料中,其輸出在所有的操作頻率皆會具有相同的振幅與相反的相位,所以這兩種巴倫即使在具有損耗的環境中,仍可正常運作。在實作結果中,改良式的馬爾尚巴倫明顯地具有較好的效能,其輸出在 4 到 25 GHz 相位差約 180±5°、振幅差約 ±0.5 dB,而其分數頻寬大於 140 %。為了進一步比較,將此兩型態巴倫整合在微混頻器的本地訊號級,而相較於傳統馬爾尚巴倫,改良型巴倫多提供 30 %操作頻寬。即使在具損耗的基板上,巴倫消耗損耗大約只有 2~3 dB。

關鍵字:耦合指數、雙頻帶、馬爾尚巴倫、微混頻器、相位反轉器、正交、鼠徑耦合器、矽鍺雙載子互補式金氧半導體、矽基板、寬頻。

Gilbert Micromixer with Integrated 90°/180° Hybrids in Standard Si IC Process

Student: Sheng-Che Tseng   Advisor: Chinchun Meng

Department of Communication Engineering
National Chiao Tung University

Abstract

In this dissertation, all single-ended Gilbert micromixers are demonstrated using 0.35-μm SiGe BiCMOS technology. For wideband operation, a transimpedance amplifier with resistive feedback is utilized in the IF stage while a broadband balun or a rat-race coupler is employed to generate wideband differential local oscillator (LO) signals. These microwave passive components in our study can generate truly balanced signals even in the presence of a lossy low-resistivity (~10 Ω·cm) silicon substrate. A systematic approach to measure the frequency response of each individual stage in a Gilbert mixer is developed in Chapter 2.

In Chapter 3, adjustable and reactive in-phase/quadrature (I/Q) generators with constant resistance are proposed with the properties of low loss, dual-band implementation, and high quadrature accuracy. The quadrature phase property and input matching of the I/Q generator can be achieved at all frequencies simultaneously. However, the magnitude balance of the dual-band I/Q generator is achieved at two designed frequencies. A 2.4/5.2 GHz I/Q down-converter and a 2.4/5.7 GHz single-sideband up-converter are demonstrated.

In Chapter 4, this dissertation realized a broadband uniplanar phase-inverter rat-race coupler using a standard silicon process, and then analyzed this coupler under

a lossy condition. A phase inverter is employed in this coupler, not only to extend the operation bandwidth, but also to generate balanced outputs, while symmetrical spiral-shaped coplanar striplines (CPSs) are also utilized to shrink the coupler size, as well as to construct a phase inverter in the middle of one of spiral CPSs. The distortionless lossy CPS has a real characteristic impedance, and thus, perfect port matching of the coupler can be achieved. A wideband Gilbert micromixer with an LO rat-race coupler is demonstrated and works from 2.5 to 13 GHz.

In Chapter 5, the wideband mixer with an integrated LO Marchand balun has the conversion gain of 15 dB and works from 3.5 to 14.5 GHz. In addition, a 15.5-dB conversion gain Gilbert mixer with a miniaturized lumped-element Marchand balun is demonstrated for UWB applications. In Chapter 6, a planar Marchand balun and its modification are analyzed and designed with a coupling factor and a corresponding characteristic impedance. The modification has duality with the original Marchand balun in structure. However, this proposed alteration has a much larger operation bandwidth than the prototype. Additionally, based on our analysis, the fact is found that the balun's outputs are always equal in magnitude and opposite in phase within all frequency ranges, as long as the material is homogeneous. Namely, these baluns, even in a lossy material, still function well. The implemented modified Marchand balun has a better performance with outputs of an 180±5° phase difference and a ±0.5-dB magnitude imbalance from 4 to 25 GHz. The fractional bandwidth is more than 140%. Also, the modified Marchand balun integrated at the LO stage of the mixer offers more than 30%-operation bandwidth.

Keywords: Coupling factor, dual-band, Marchand balun, micromixer, phase inverter, quadrature, rat-race coupler, SiGe BiCMOS, silicon substrate, wideband.

Acknowledgements

五年來的歡笑與淚水，將成為我人生最美好回憶。

　　感謝爸爸、媽媽、阿姨、姊姊、大哥與二哥的支持，讓我在求學的路途平順、衣食無憂；要感謝的人太多了，今日的成果，因為有大家，才如此豐碩，願此榮耀與大家共享。

Shenglhe Tseng

NCTU, July 2008

Table of Contents

Table of Contents

List of Figures

Chapter 5

Chapter 6

Chapter 7

Appendix C

List of Tables

List of Abbreviations and Symbols

Abbreviations

BiCMOS	Bipolar Complementary Metal Oxide Semiconductor
CG	Conversion Gain
CPS	Coplanar Stripline
CPW	Coplanar Waveguides
EM	Electromagnetic
FGCPW	Finite-Ground Coplanar Waveguide
GSGSG	Ground–Signal–Ground–Signal–Ground
HBT	Hetero-junction Bipolar Transistor
I/OP$_{1dB}$	Input/Output 1-dB Gain Compression Point
I/OIP$_3$	Input/Output Third-Order Intercept Point
I/Q	In-Phase/Quadrature
IC	Integrated Circuit
LO	Local Oscillator
NF	Noise Figure
pMOS	p-channel MOSFET
RFICs	RF Integrated Circuits
SiGe	Silicon-Germanium
SSB	Single Side-Band
TCA	Transconductance Amplifier
TIA	Transimpedance Amplifier
UWB	Ultra-Wideband
WiMAX	Worldwide Interoperability for Microwave Access
WLAN	Wireless Local Area Network
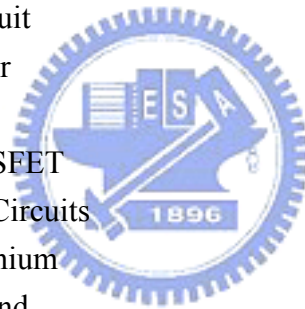
Symbols

α	Attenuation constant
β	Propagation constant
γ	Complex propagation constant
λ	Wavelength
ω_0	Operating frequency, resonant frequency
$\omega_{transition}$	Transition frequency
$\omega_{h,l}$	Operating frequency for each high(h)/low(l) band

f_T	Cut-off frequency
gm	Transconductance of a transistor
k	Coupling factor
z	Normalized characteristic impedance with respect to Z_0
$\hat{z}$	Complex normalized characteristic impedance with respect to Z_0
Q	Quality factor
R_0, L_0, G_0, C_0	Per-unit-length resistance, inductance, conductance, and capacitance
R, I, C, T	Reflection, isolation, coupling, and through coefficients of the coupled line
Y_0e	Even-mode characteristic admittance
Y_0o	Odd-mode characteristic admittance
Z_0	Terminal impedance
Z_0e	Even-mode characteristic impedance
Z_0o	Odd-mode characteristic impedance
Z_C	Characteristic impedance

Chapter 1 Introduction

1.1 MILLIMETER-WAVE AND MICROWAVE IN SILICON

High data rate and wide bandwidth wireless communication systems are easily feasible in millimeter-wave and microwave frequencies. Recently, many applications are booming in millimeter-wave and microwave bands thanks to the advance of the semiconductor technologies and wireless communication techniques, such as the high-speed wireless local area network, automotive collision avoidance radar, image sensing, and so on. The demand of the wireless communication services stimulates the researches of the millimeter-wave and microwave circuit design.

The more than 30-GHz millimeter-wave band has a broad bandwidth and low interference, because of the high absorption rate in the air, as shown in Fig. 1-1. In the past, the applications in this band were not popular due to the device characteristics and integration techniques. However, up to now, many studies and techniques have been developed for the millimeter-wave and microwave applications, for instance, device and package technologies. In Europe, America, and Japan, the frequency resource is also planed. Now, applicable bands include 24 GHz for microwave Doppler sensors, 38 GHz for short-haul transmission-links, 57-66 GHz for WiHD, 76-77 GHz for automotive radars, 77-81 GHz for automotive short-haul radars, 71-76, 81-86, 92-95 GHz for wireless wideband communications, as shown in Fig. 1-2. The applications cover livelihood, satellite communication, astronomy, and national defense. The profits from the millimeter-wave and microwave applications are more than one hundred million dollars in the whole world. Therefore, the millimeter-wave and microwave researches should be at the high priority.
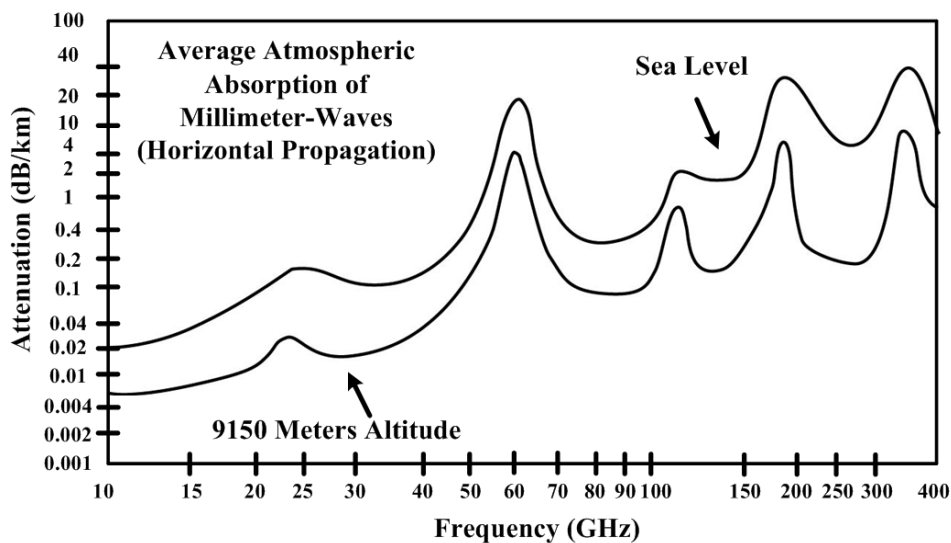
Fig. 1-1   Average atmospheric absorption rate of millimeter-waves.
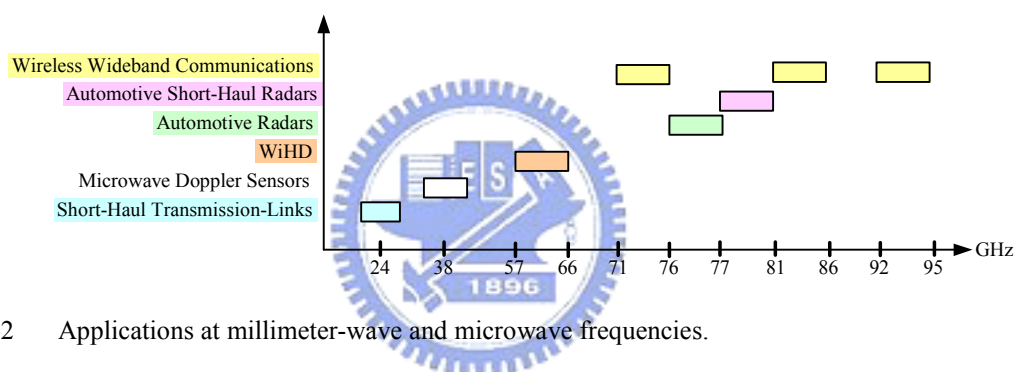
Fig. 1-2   Applications at millimeter-wave and microwave frequencies.

Three solutions are shown in Fig. 1-3 for the millimeter-wave and microwave applications. In the past, the front-end was fabricated only using GaAs processes due to device performances. However, the reliability and productivity of GaAs technology are low. Moreover, the GaAs front-end cannot be integrated into the CMOS baseband IC. Fig. 1-4 describes the silicon evolution and reveals that chip size is getting bigger while device operation frequency is getting high. Advanced deep sub-micron silicon-based technologies have made the silicon devices with > 100-GHz cut-off frequency possible and thus the era of silicon millimeter wave is impending. Millimeter-wave system-on-chip (SOC) will become a reality because of the high integration and low-cost production of the silicon fabrication processes. Even,

77-GHz antennas are also integrated on chips in Fig. 1-5.
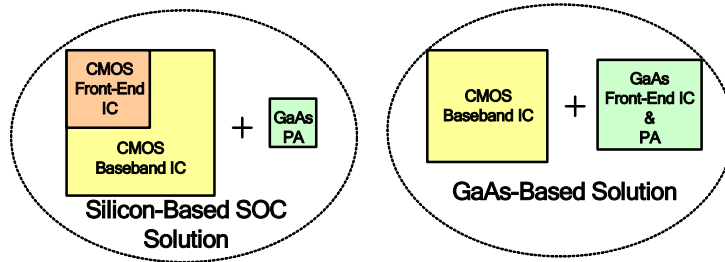
Fig. 1-3   Millimeter-wave and microwave solutions.
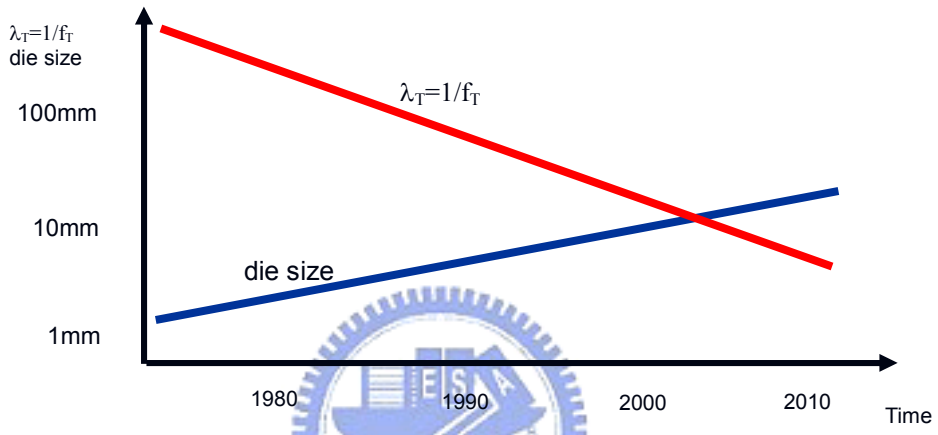
Fig. 1-4   Evolution of chip size, device performance, and operation frequency in silicon.
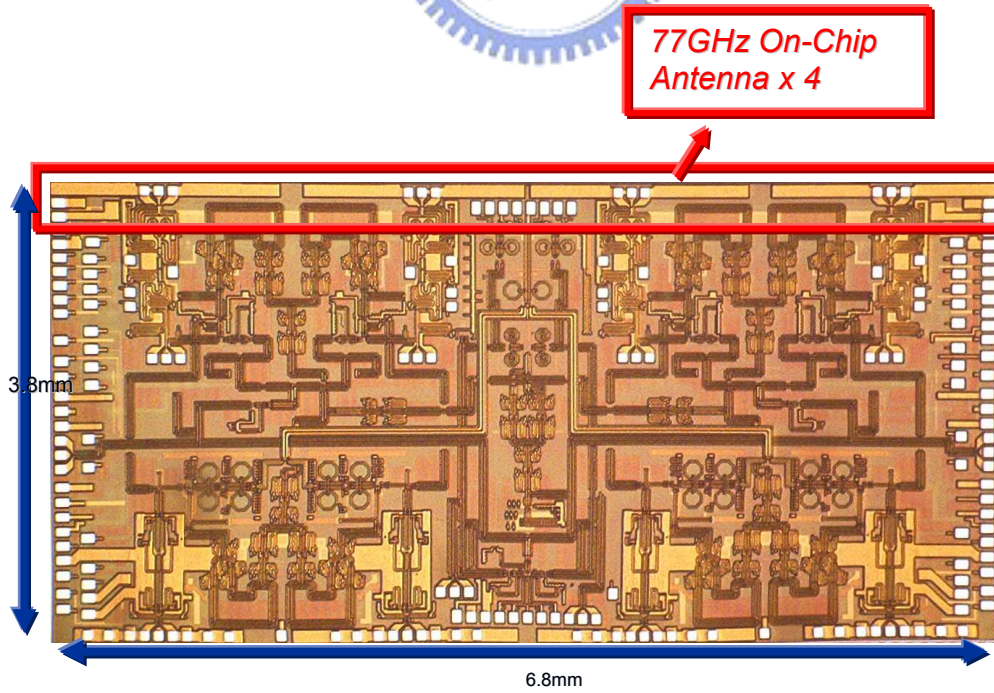
Fig. 1-5   77-GHz phase-array antenna system [Hajimiri, ISSCC 2006].

According to the TSMC technology development in Fig. 1-6, the 32-nm process is developing now and the 45-nm is at the production level for logic circuits, whereas the RF circuits can be fabricated using advanced technologies like a 65-nm CMOS process. Fig. 1-7 describes the throughput of each TSMC CMOS technology. The R&D cost is the most important issue when the mask cost increases tremendously for the advanced technologies, as shown in Fig. 1-8. Nevertheless, the advance in silicon processes is not good for scale-down of the front-end chips since passive components in front-end circuits dominate chip size. As shown in Fig. 1-9, the area of the RF front-end does not shrink obviously with the technology advance and the ratio of the front-end part is getting higher. Therefore, the passives affect not only the front-end performances but also the entire cost, and the research topic in this dissertation is the size and performance of the passive components.
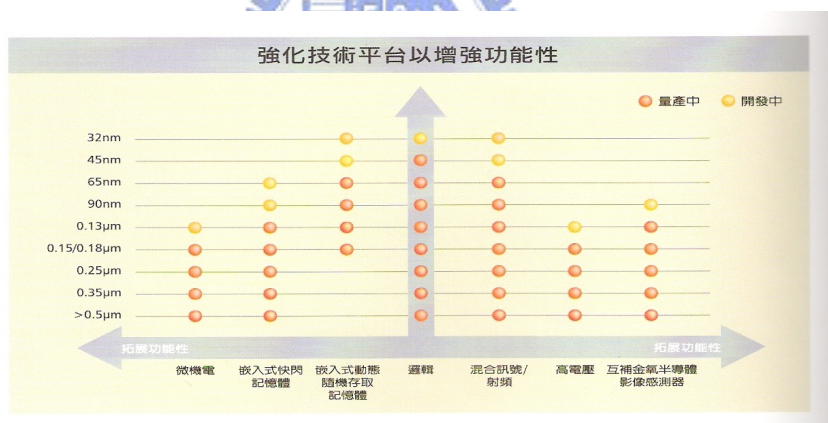
Fig. 1-6   Silicon technology development in TSMC.
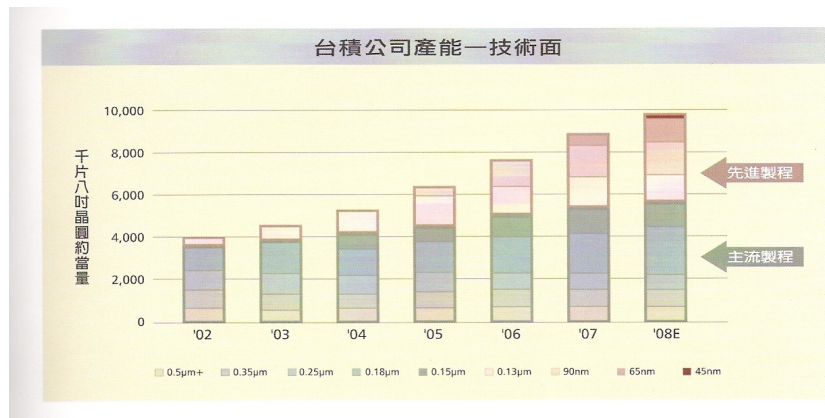
Fig. 1-7   Throughput of each TSMC CMOS technology.

Tech.	Cost (Wafer/Mask set)
0.18 μm	1.4K/120K
0.13 μm	1.8K/300K
90 nm	2.5K/900K
64 nm	3.8K/1400K
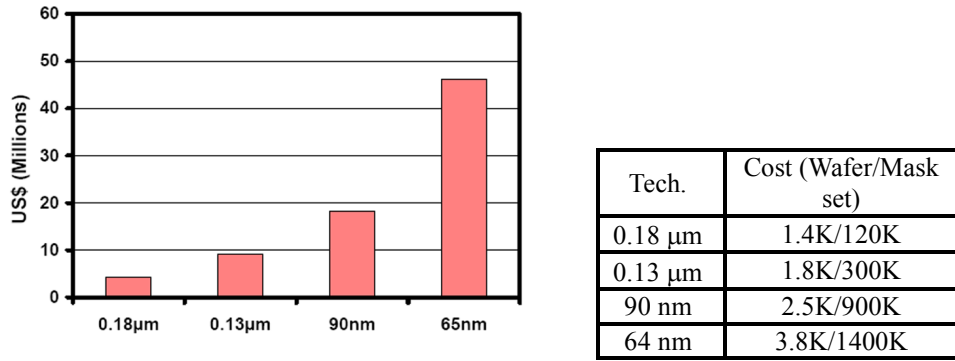
Fig. 1-8   R&D cost for silicon processes [Morris Chang, "Foundry Future: Challenges in the 21st Century", in ISSCC 2007].

(a)   (b)   (c)
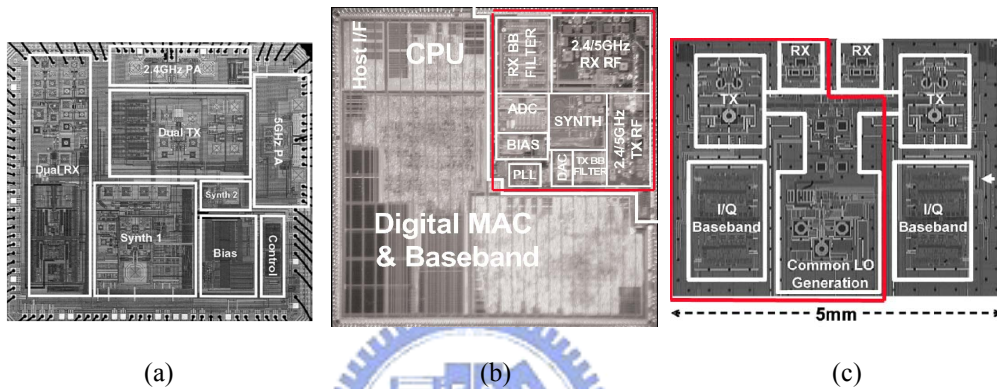
Fig. 1-9   Silicon-based   system-on-chips   (a)Atheros[JSSC2004]   0.25um   (RF:23mm^2) (b)Atheros[ISSCC 2006] 0.18um (RF:13.5mm^2) (c)DICE[JSSC2006] 90nm (RF:12mm^2).

1.2 SILICON-BASED PASSIVE COMPONENTS

The era of the wireless applications with high data-rate transmission and multiple functions is coming, e.g., the IEEE 802.11a/b/g combo system [1], ultra-wideband (UWB) system [2], and WiMAX system [3]. The range of carrier frequencies and their bandwidth constantly increase. The obligation of the complicated data processing belongs to the baseband design, while the RF integrated circuit (IC) design takes responsibility for the wide range frequency and broad bandwidth operation. Nevertheless, the design of the high-frequency and wideband RF circuits is a big challenge in the overall solution implementation. For an active mixer, the transistors have natural instinct to perform wide range and broad bandwidth frequency translation. Due to the input/output matching networks, narrowband passive

components, and loading effects, the mixer's wideband ability is restricted. Hence, microwave broadband passive components, such as Marchand baluns and rat-race couplers, can be integrated into ICs for wideband applications.

The silicon radio-frequency/microwave integrated circuit revolution has brought inductors and transformers into integrated circuits. As the silicon circuit reaches the millimeter-wave regime, new circuit design concepts arise. In our researches, a *CR-LR* quadrature generator takes the place of a polyphase filter while inductors and transformers along with parasitic capacitance operate as a transmission line and a coupled line, respectively, as shown in Fig. 1-10. The inductor absorbing parasitic capacitors to form a transmission line enables the high frequency operation. It is now feasible to integrate passive components based on quarter-wavelength transmission lines in the integrated circuits.
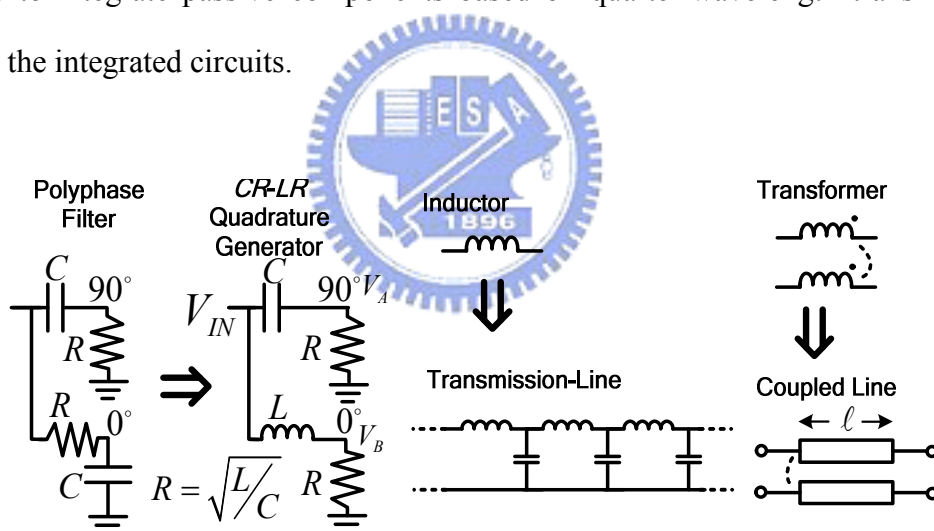
Fig. 1-10   New design concepts for high-frequency applications.

Silicon-based technologies have the properties of high integration and low-cost production. Active devices have advanced in possession of the cut-off frequency of more than 100 GHz, and they are suitable for microwave and millimeter-wave applications [4]. Today, passive components are largely implemented using silicon-based technologies in the RFICs. For example, inductors and transformers are

applied in oscillators, low-noise amplifiers, and mixers [5]. However, the standard silicon substrate with a resistivity of approximately 10 Ω·cm deteriorates signals, causes crosstalk between two adjacent passives, and influences the functions of passive components. Thus, it is a big challenge to form useful RF passive components on a silicon substrate for microwave and millimeter-wave applications [6], [7].

To reduce the substrate loss, many solutions have been developed, such as micromachining, high-resistivity substrate, silicon-on-insulator (SOI) process and shielding. Abidi *et al.* applied the front-side micromachining to form a suspended inductor in a CMOS RF amplifier. Thus, this inductor has higher self-resonance frequency and quality factors and can work at higher frequencies [8]. The backside micromachining is also employed to eliminate the unpredictable pattern-dependent etching behavior of front-side micromachining [9], [10]. Besides this, the high-resistivity (~1 kΩ·cm) silicon substrate is also employed, but the entire substrate with high resistivity is not compatible with active devices, due to the latch-up issue [11]. The local high-resistivity substrate can be obtained by proton-damaged ion implantation with high energy (15 MeV) before the backend process, or with low energy (~4 MeV) after the backend process [12]. The substrate resistivity increases significantly to ~1 MΩ·cm. The performances of the transmission lines and spiral inductors on the proton-damaged high-resistivity silicon substrate are enhanced [12], [13]. Shielding, like patterned ground shields [14] and floating shields [7], is inserted between the signal path and the silicon substrate, to resist the substrate loss without any extra process. This method is adequate for the process with multiple metal layers.

In this dissertation, our passive components function well in standard silicon-based IC processes because of the new design concepts such as balanced path loss and distortionless transmission lines. The implementation directly on the silicon

substrate is good for size compactness thanks to the high dielectric constant. Meander lines compress the size while stepped-impedance and lumped-element techniques shrink the transmission-line length further as well as reducing the loss. In this dissertation, it shows that passive components such as *CR-LR* reactive quadrature generators, ring hybrids, and Marchand baluns could be successfully integrated into standard silicon-based ICs.

As shown in Fig. 1-10, the proposed reactive quadrature generator is derived from the conventional *C-R* and *R-C* sections. The low-pass session, *R-C* section, is substituted by the *L-R* network. The truly balanced quadrature signals are generated when $R=\omega_0 L=(\omega_0 C)^{-1}$. Regardless of frequencies, the input impedance equals *R* and the output signals are always in quadrature. When compared with a polyphase filter, this reactive quadrature generator has three advantages. 1) The generator has low loss thanks to the absence of resistors and is suitable for high-frequency applications. 2) The input impedance is constant and the wideband matching is achievable. 3) A multi-band quadrature generator can be established by increasing the order of the *L-C* networks.

A wideband phase-inverter rat-race coupler and a broadband Marchand balun are presented to demonstrate the new design concept of the transmission lines and coupled lines for silicon-based millimeter-wave ICs, respectively. Our microwave passives are directly implemented on a lossy silicon substrate. The transmission-line length of passive components reduces with operation frequency increase and so does the loss, as shown in Fig. 1-11. Therefore, the rat-race coupler and Marchand balun operate better at millimeter-wave frequencies. The passive components and the proposed design approaches can be applied for the millimeter-wave regime.
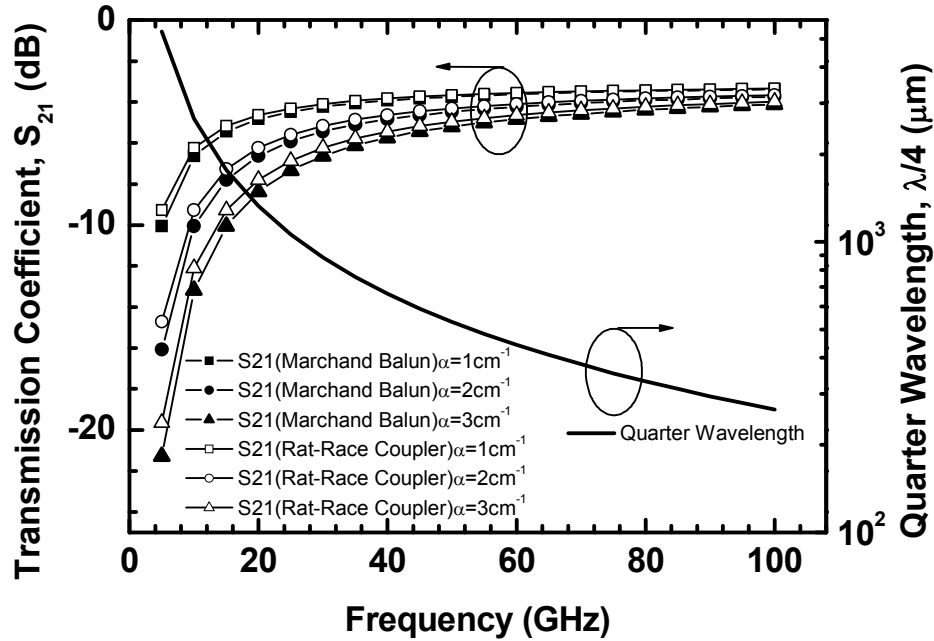
Fig. 1-11   Quarter-wavelength and transmission coefficient with respect to operation frequencies with assumption of $\varepsilon_{eff} = 8$.

1.3 RESEARCH WORKS

Chapter 2 depicts a wideband micromixer and monitors the frequency response of each stage of the mixer. Chapter 3 offers a novel adjustable and reactive quadrature generator for wideband or dual-band applications. Chapter 4 analyzes and designs a phase-inverter rat-race coupler with spiral-shaped coplanar striplines (CPSs) in the present of loss. The Marchand balun design concept and the measured results of a monolithic planar Marchand balun are represented in Chapter 5. The optimal design of the lossy Marchand balun and its modification are proposed in Chapter 6. The implemented circuits are described as follows:

● Wideband Gilbert micromixer

● Dual-band I/Q down-converter with an adjustable and reactive LO quadrature generator

● Dual-band SSB up-converter with an adjustable and reactive LO quadrature generator

- Phase-inverter rat-race coupler with spiral-shaped CPSs

- Wideband Gilbert micromixer with a phase-inverter rat-race coupler

- Planar Marchand balun

- Lumped-element Marchand balun

- Modified Marchand balun

- Wideband Gilbert micromixer with an integrated LO Marchand balun

- Wideband Gilbert micromixer with a lumped-element Marchand balun

- Wideband Gilbert micromixer with a modified Marchand balun

Chapter 2 Wideband Micromixer

2.1 INTRODUCTION

For the wideband circuit design, the wideband matching of the input/output ports is a significant issue. The common implemented active mixer is a Gilbert mixer using the emitter-coupled differential input stage. Owing to the high input impedance of the common-emitter-configured transistors, the reactive or resistive matching is needed at the input port. For the reactive matching, the matching bandwidth relates to the orders of the passive matching network. Increasing the order of the matching network can expand the operation bandwidth, but also takes more area. Although the resistive matching can perform wideband matching, it also introduces loss. The variant of the Gilbert mixer, the so-called micromixer, which is defined as a microwave mixer in [15], has the properties of the wideband input matching and single-ended input. Those properties facilitate the realization of the wideband and single-ended mixer. In this work, the input stage of the mixer is made up of the micromixer.

High impedance resistors or active pMOS loads are usually employed to obtain high conversion gain. In addition, the pMOS current mirror is used to effectively combine the differential IF output current signals of the mixer and establish a single-ended output. However, the high impedance causes a low-frequency pole at the output stage, which slows down the IF response. The transimpedance amplifier (TIA) with resistive feedback is, hence, utilized at the output stage to reduce the output impedance and extend the bandwidth in this work [16], [17]. A single-ended wideband Gilbert down-converter is fabricated in the 0.35-μm SiGe BiCMOS technology and demonstrated in this chapter. A technique to measure the RF, LO, and IF stages of a Gilbert mixer is developed as well.

2.2 CIRCUIT DESIGN

The entire schematic of the single-ended wideband down-converter is shown in Fig. 2-1. This down-converter is formed by the micromixer and the TIA output buffer. Each element has the broadband property. The micromixer can be considered as the combination of two single-balanced mixers. One mixer is formed by the common emitter-configured RF amplifier Q_2; the other is composed of the common-base-configured RF amplifier Q_3. The LO switch quad is made up of the transistors Q_5, Q_6, Q_7, and Q_8. The current mirror pair Q_1 and Q_2 provides the balance dc currents in the RF input stage and then these two RF amplifiers have equal magnitude and opposite phase transconductance gain to obtain good mixer balance. Moreover, the diode-type transistor Q_1 reduces the input impedance of Q_2 and enhances the speed of the common-emitter-configured input stage. The input impedance is controlled by the transistors Q_1 and Q_3 and the resistors r_1 and r_3. It is easy to achieve wideband matching so this micromixer can act as a wideband mixer [18].
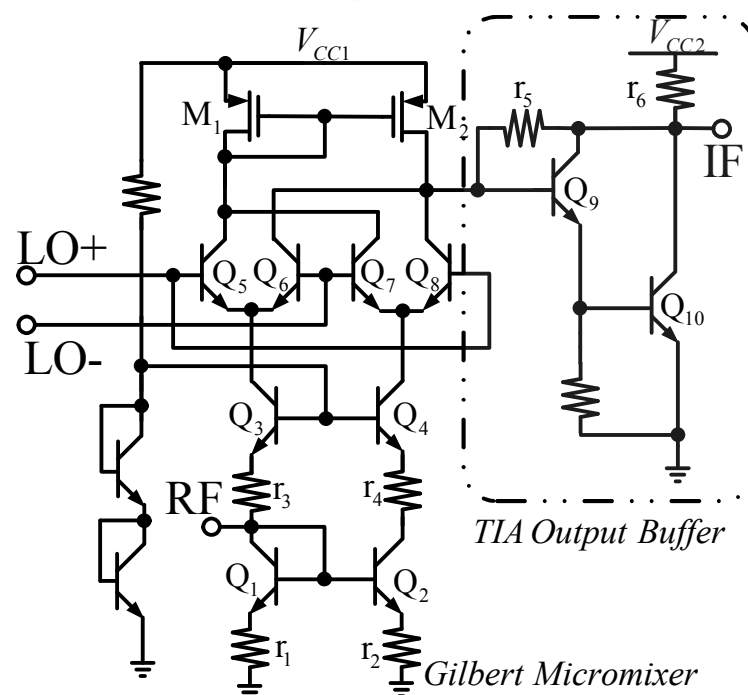
Fig. 2-1   Schematic of the micromixer with a TIA output buffer.

To establish a single-ended output, the pMOS current mirror is applied to combine the differential output current signals of the mixer. Furthermore, a TIA amplifier is used in the output stage of this mixer. The frequency response of the input stage is dominated by the common-emitter-configured transistor Q_2. As shown in Fig. 2-2, in the critical path, the RF input stage is viewed as a transconductance amplifier (TCA), the IF output stage is a TIA, while the LO switch quad is inserted in the middle and performs the frequency translation. The topology is very similar to the well-known Cherry–Hooper amplifier—a TCA stage in cascade with a TIA stage[16].

$$\boxed{TCA}\ \frac{i_{o2}}{V_{in}} = \frac{-g_{m2}}{1+g_{m2}R_e}$$

$$A_{vo} = \frac{i_{o2}}{V_{in}} \times \frac{V_{out}}{i_{o2}}$$

$$\boxed{TIA}\ \frac{V_{out}}{i_{o2}} = -R_f$$
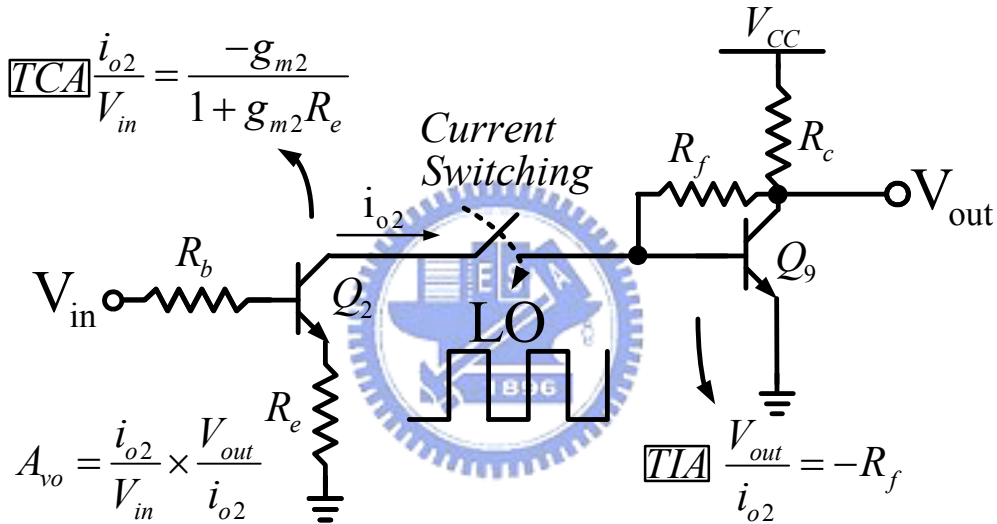
Fig. 2-2   Cherry Hooper technique employed in the micromixer.

The LO current commutation quad Gilbert mixer cell is used to switch the connecting current between the TCA and TIA stages. Thus, the conversion gain and frequency response can be analyzed as a TCA for the RF stage and a TIA for the IF stage. The TIA output buffer employs a resistive feedback to enlarge the output bandwidth. In addition, a Darlington pair is also utilized to enhance the speed of transistors. Therefore, this output stage of the mixer has single-ended and wideband properties. To analyze the frequency response, the small-signal model is split into two parts, as shown in Fig. 2-3. For simplicity, the base–emitter resistance and base–collector

capacitances are neglected in the frequency response analysis. The complete transfer functions of the TCA and TIA stages from exact circuit analysis are denoted as

$$A_v(S) = \frac{i_{o2}}{V_{in}}(S) \cdot \frac{V_{out}}{i_{o2}}(S) = \frac{G_{m2}}{1 + S\big/\omega_{P2}} \times \frac{R_{m9}}{1 + S\big/\omega_{P9}} \tag{2.1}$$

where

$$\begin{cases} G_{m2} = \dfrac{g_{m2}}{1 + g_{m2}R_e} \\[2mm] R_{m9} = -R_f \\[2mm] \omega_{P2} = \dfrac{1}{C_{\pi 2}\dfrac{R_e + R_b}{1 + g_{m2}R_e}} \\[4mm] \omega_{P9} = \dfrac{1}{C_{\pi 9}\dfrac{R_f + R_c}{1 + g_{m9}R_c}} \end{cases} \tag{2.2}$$
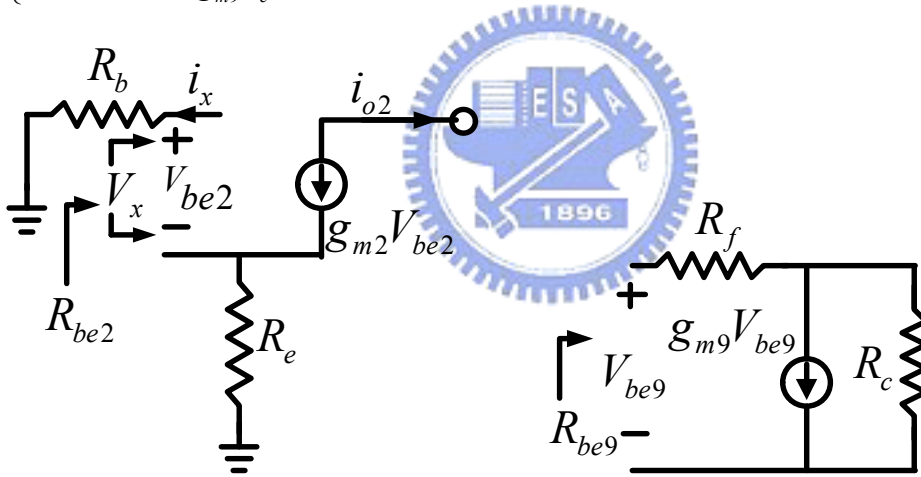
(a) TCA   (b) TIA

Fig. 2-3   Small signal models of (a) the transconductance amplifier (TCA) and (b) the transimpedance amplifier (TIA).

From the open-circuit time-constant analysis, the poles of the TCA and TIA stages in Fig. 2-3 are

$$\omega_{P2} = \frac{1}{R_{be2}C_{\pi 2}} \tag{2.3}$$

and

$$\omega_{P9} = \frac{1}{R_{be9}C_{\pi 9}} \tag{2.4}$$

where

$$R_{be2} = \frac{R_e + R_b}{1 + g_{m2}R_e} \tag{2.5}$$

and

$$R_{be9} = \frac{R_f + R_c}{1 + g_{m9}R_c} \tag{2.6}$$

are the resistances looking into the base–emitter terminals of Q_2 and Q_9 in Fig. 2-3, respectively [19]. As a result of a resistive feedback, the poles are extended by the feedback factor of $1+g_mR$. The overall voltage gain can be calculated as

$$A_{vo} = G_{m2} \cdot R_{m9} \simeq \frac{g_{m2}R_f}{1 + g_{m2}R_e} \ . \tag{2.7}$$

2.3 MEASUREMENT RESULTS

The wideband micromixer was fabricated using 0.35-μm SiGe BiCMOS technology [20], [21]. Fig. 2-4 illustrates the die photograph of the implemented mixer. The chip size is to approximately 0.75 mm × 0.75 mm. The measurement results give excellent agreement with the wideband operation of the micromixer.
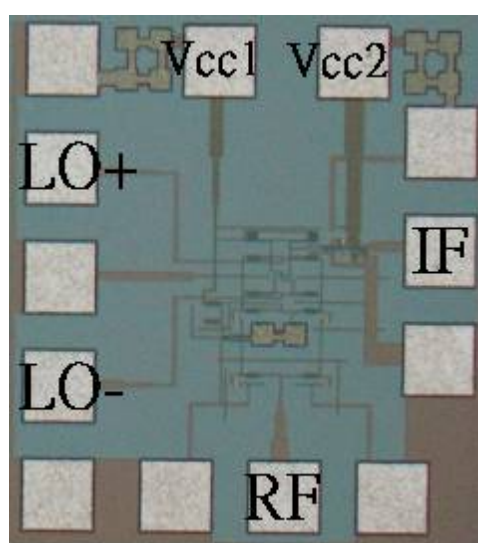
Fig. 2-4   Die photograph of the micromixer.

The wideband property of the micromixer is shown in Fig. 2-5. For the micromixer without an LO balun, an external single-to-differential balun is employed to generate differential LO signals. Five external baluns in different frequency range (0.002-to-2 GHz, 2-to-4 GHz, 4-to-8 GHz, 8-to-12.4 GHz, and 12.4-to-18 GHz baluns) are employed to perform the measurements in each band. Obviously, the mixer has the broad band property. Its input return loss is below -14 dB at overall operating frequencies. The conversion gain is approximately 15 dB. The mixer works up to 15 GHz. The conversion gain is approximately 15 dB and the 3-dB IF bandwidth is approximately 400 MHz, as shown in Fig. 2-6.
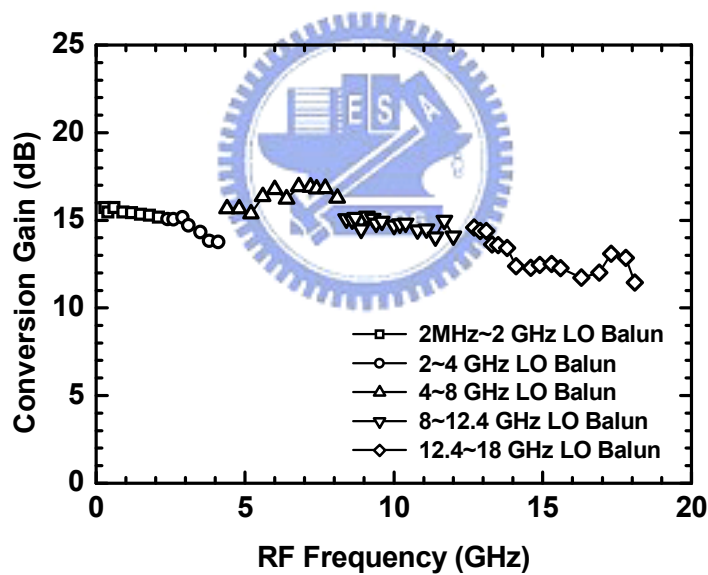
Fig. 2-5   Conversion gain of the micromixer with respect to RF frequencies.
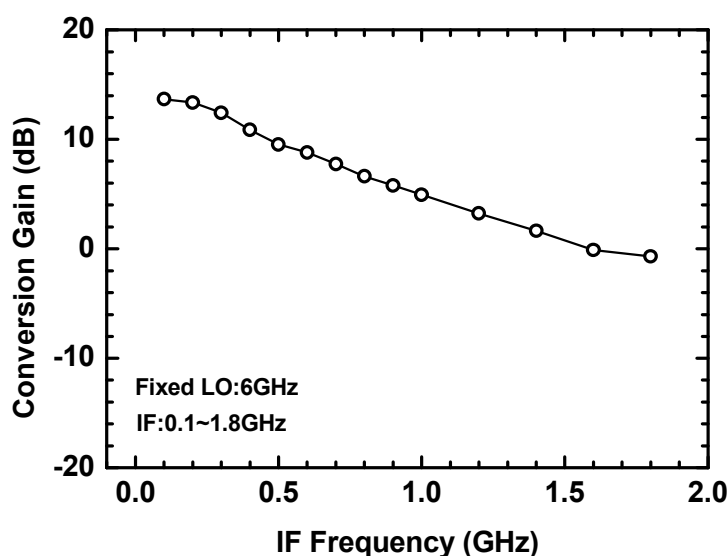
Fig. 2-6   Conversion gain of the micromixer with respect to IF frequencies.

Fig. 2-7 illustrates that the effect of the LO power on the conversion gain is measured with the fixed IF frequency of 100 MHz, but different LO frequencies by Agilent's E4448A power spectrum analyzer (PSA). The current commutation in the Gilbert cell is responsible for the frequency translation. The differential pair of the bipolar Gilbert cell only needs a small twist voltage (approximately 0.1 V) to perform the near-perfect current commutation. Once the LO power is large enough to drive the switch quad of the Gilbert mixer, the conversion gain keeps constant and is insensitive to the LO power. If the LO power is too large, the quad switch SiGe HBT transistors enter the saturation region and then the mixer gain degrades. However, there is more power to drive the switch quad at higher frequencies. With the LO frequency increase, the LO power range for the flat constant conversion gain region decreases.

17
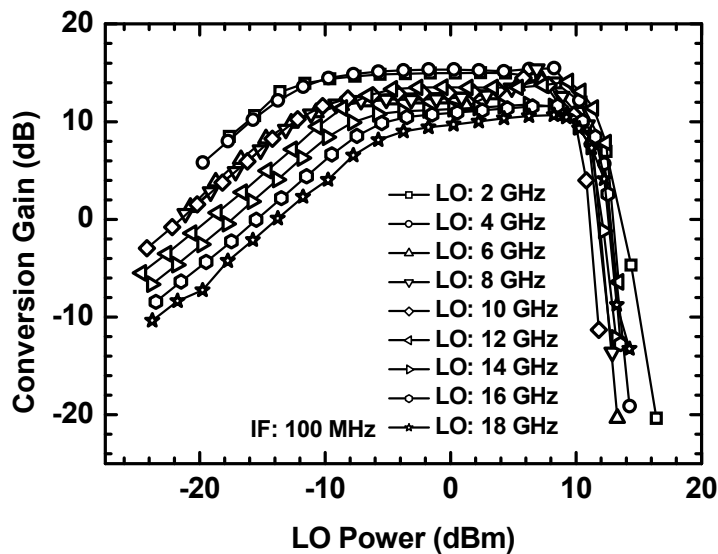
Fig. 2-7   Conversion gain of the micromixer with respect to LO power.

The RF and IF bandwidth experiments in Fig. 2-5 and Fig. 2-6 give the direct measurement of the IF and RF stage frequency response of the mixer, while the frequency response of the LO Gilbert cell is examined in Fig. 2-7. The higher the LO frequency, the narrow the flat gain region becomes. The flat gain region still exists for LO frequencies up to 18 GHz. According to the measured results, the maximum operating frequency of the mixer is approximately 15 GHz and is limited by the RF input stage.

TABLE 2.1 Measurement Results of the Wideband Micromixer

TSMC 0.35μm 3P3M SiGe BiCMOS	
Item	Down-Converter
RF Frequency	Up to 15 GHz
Conversion Gain	15 dB
IF Bandwidth	400 MHz
LO Speed	> 18 GHz
LO Power	-8 dBm ~ 8 dBm
RF Return Loss	<-14 dB
IF Return Loss	< -12 dB
Supply Voltage	5 V
Power Dissipation	60 mW (Core) / 65 mW (Buffer)
Chip Size	0.75 mm × 0.75 mm

2.4 SUMMARY

A single-ended wideband Gilbert mixer has been demonstrated using 0.35-μm SiGe BiCMOS technology. This wideband mixer has the conversion gain of 15 dB and works up to 15 GHz with 400-MHz IF bandwidth. A systematic approach to measure the frequency response of the RF, IF, and LO stages of a Gilbert mixer has been developed. The developed frequency response measurement technique can be employed to identify the frequency-limiting mechanism.

Chapter 3 Adjustable and Reactive I/Q Generator With Constant Resistance for Down- and Up-Converters

3.1 INTRODUCTION

There is a tendency towards multimode and multiband communication systems, such as the IEEE 802.11a/b/g wireless local area network (WLAN) combo system [1]. The communication ability and diversity enhance for users but the challenges also augment for designers. For the RF integrated circuits (RFICs), it is very difficult that the optimal performance of the matching, noise figure, or quadrature accuracy is carried out for multiple frequency bands. Much research has focused on dual-band low noise amplifiers [22]. The dual-band input matching is achieved by using a high-order reactive matching network. However, generating dual-band quadrature signals from reactive elements is still a challenge.

The quadrature mechanism is widely used in the system architecture, for instance, sub-harmonic mixers [23], in-phase/quadrature (I/Q) down-converters, single-sideband (SSB) up-converters [24], and Weaver and Hartley transceivers [25]. There had been five types of quadrature generators. The first one is a polyphase filter, which is employed throughout the RFICs [26], [27]. Its phase accuracy improves with more *RC-CR* sections. More than three sections are needed to resist the fabrication variation and to maintain precise quadrature signals. However, the resistive loss of the polyphase filter also increases. Besides, the polyphase filter is not suitable at high-frequency regimes because of its parasitics and the resistor self-cutoff frequency [26]. Using ring oscillators to generator quadrature signals is the second means [28], [29]. Although the ring oscillators have wide oscillation frequency in comparison with *L-C*

oscillators, their poor phase accuracy and phase noise deteriorate the performance of the entire transceiver [30]. Third, differential signals can be converted to quadrature signals by a divide-by-2 divider [31]. The input differential signals should operate with twice the desired frequency, and the oscillator with two times the desired frequency is not easily designed at high frequencies. The fourth way is to apply a quadrature coupler. The quadrature couplers, like a transmission line coupler and a Lange coupler, are often used in millimeter-wave applications [32]. However, the coupler size limits its usage in the RFICs. In spite of the size reduction of the spiral transmission line coupler, the phase accuracy and magnitude balance are not easily controlled, and hence, the performance is not good enough [33], [34].

The final solution is to directly construct a quadrature oscillator with a cross-coupling scheme between two differential oscillators. There are two types of the coupling schemes—the fundamental coupling scheme and harmonic coupling scheme. The fundamental coupling scheme includes the top-series coupling scheme, bottom-series coupling scheme, and paralleled coupling scheme [35]. There is a trade-off between phase noise and quadrature accuracy in this fundamental coupling scheme [36]. The good quadrature accuracy can be fulfilled at the cost of the phase-noise performance of the oscillators. In the harmonic coupling scheme, perfect quadrature signals can be obtained without phase noise degradation, but a differential amplifier or a transformer performing the coupling between oscillators should function at twice the oscillation frequency [37]. The quadrature ring oscillators, coupled oscillators, and dividers as quadrature generators are only employed at the LO stage.

The mentioned approaches are all utilized in a single frequency band. In this chapter, a dual band adjustable and constant-resistance I/Q generator is proposed.

Since the generator is composed of pure reactive components, inductors and capacitors, there is no loss introduced. Besides, the multiband I/Q generator is easily implemented by increasing the order of the *L-C* networks. Capacitors along with varactors will add the ability to control the phase and magnitude of the quadrature outputs. The configuration and optimization for the quadrature accuracy are also described here. A 2.4/5.2 GHz I/Q down-conversion mixer and a 2.4/5.7 GHz SSB upconversion mixer using 0.35-µm SiGe BiCMOS are demonstrated with the dual-band adjustable and reactive I/Q generator. Thanks to the excellent quadrature accuracy, the magnitude mismatch and phase error of the down-converter outputs are <1% and <1°, respectively, and the maximum sideband rejection ratio of the up-converter is up to 50 dB. According to the measurements, the down-converter outputs are always in quadrature and the I/Q generator input matching is achieved over all frequencies. In addition, the operation bandwidth (sideband rejection ratio > 30 dB) is 200 MHz at 2.4 GHz and 720 MHz at 5.7 GHz.

3.2 REACTIVE I/Q GENERATOR

A polyphase filter consisting of *R-C* and *C-R* sections is an I/Q generator. Nevertheless, the polyphase filter is not appropriate for high frequency applications because the parasitics and the resistor self-cutoff frequency deteriorate phase and magnitude accuracy [26]. In this dissertation, the quadrature generator formed by *C-R* and *L-R* sections is proposed here. This reactive I/Q generator is derived from the conventional *C-R* and *R-C* sections as shown in Fig. 3-1. For the *R-C* section, the transfer function is derived as

$$\frac{\dfrac{1}{SC}}{R+\dfrac{1}{SC}} = \frac{\dfrac{1}{R}}{\dfrac{1}{R}+SC} = \frac{R}{R+SCR^2} = \frac{R}{R+SL} \tag{3.1}$$

where

$L = CR^2$.

Based on (3.1), the *R-C* section can be replaced by the *L-R* section as shown in Fig. 3-1. Here, a reactive I/Q generator is made of *C-R* and *L-R* sections and *R* is given by the input impedance of the following stage. Thanks to no extra resistive components in this reactive quadrature generator, no resistive loss would be introduced.
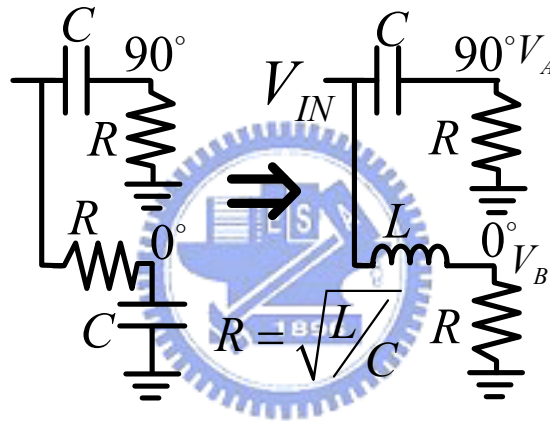
Fig. 3-1   Quadrature generators with the *C-R* and *R-C* sections or with the *C-R* and *L-R* sections.

3.2.1 *Wideband Reactive I/Q Generator With Constant Resistance*

The reactive I/Q generator is offered here to replace the polyphase filter. The key point of design principle is that an inductor advances in phase, while a capacitor delays to result in 90° phase difference. The reactive I/Q generator is shown in Fig. 3-1. *C-R* and *L-R* are in parallel. The voltage at node *A* and *B* in Fig. 3-1 can be expressed as

$$V_A = \frac{R}{\dfrac{1}{j\omega C} + R} V_{IN}$$

$$V_B = \frac{R}{j\omega L + R} V_{IN}$$

(3.2)

From (3.2), the reactive I/Q circuit with $R = \omega_0 L = (\omega_0 C)^{-1}$ can generate truly balanced

quadrature signals because V_A advances for 45° and V_B delays 45° with respect to V_{IN}.

$R = \omega_0 L = (\omega_0 C)^{-1}$ can also be viewed as $R = (L/C)^{1/2}$ and $\omega_0 = (LC)^{-1/2}$.

The input impedance of this generator can be written as

$$
\begin{aligned}
Z_{in} &= (R + j\omega L) // \left(R + \frac{1}{j\omega C} \right) \\
&= \frac{R^2 + \dfrac{L}{C} + R\left(j\omega L - \dfrac{j}{\omega C} \right)}{2R + j\omega L - \dfrac{j}{\omega C}} \\
&= R \qquad \text{when} \quad R = \sqrt{\dfrac{L}{C}}
\end{aligned}
$$

(3.3)

Under the condition of $R = (L/C)^{1/2}$, the input impedance is equal to R regardless of

frequencies. If the value of R is equal to 50 Ω, the input port of the I/Q generator is

wideband matched.

The voltage ratio between node A and B as a function of frequency can be

expressed as

$$\frac{V_A}{V_B} = \frac{j\omega L + R}{\dfrac{1}{j\omega C} + R} = \frac{\left(R^2 - \dfrac{L}{C} \right) + jR\left(\omega L + \dfrac{1}{\omega C} \right)}{R^2 + \left(\dfrac{1}{\omega C} \right)^2}.$$

(3.4)

The voltage of node A is always quadrature to that of node B and unrelated to

frequencies under the condition of $R = (L/C)^{1/2}$. Also from (3.3), the input impedance

is independent of frequency when $R = (L/C)^{1/2}$. However, the magnitude values of both

nodes are identical only at frequency of ω_0. Fig. 3-2 represents the magnitude ratio

($|V_A/V_B|$) and phase error of the I/Q generator with respect to normalized frequency,

ω_0, when $R = \omega_0 L = 1/(\omega_0 C)$. Thanks to the wideband quadrature outputs of the reactive generator and the constant conversion gain of Gilbert mixers within a wide LO power range, mentioned in Section 2.3, the Gilbert mixers with an integrated reactive I/Q generator can work for broadband applications.
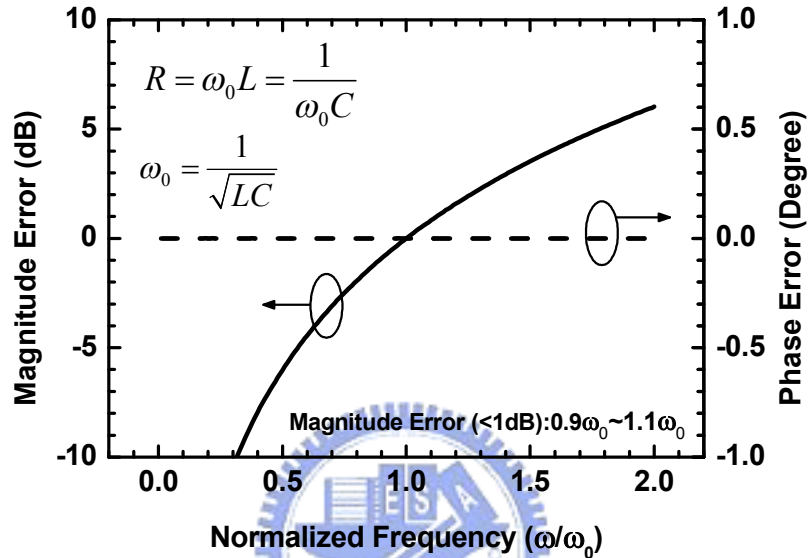
Fig. 3-2   Magnitude ratio ($|V_A/V_B|$) and phase error of the reactive I/Q generator with respect to normalized frequency ω_0.

3.2.2 Dual-Band and Adjustable I/Q Generator With Constant Resistance

When compared with the polyphase filter, this reactive I/Q generator is easily designed for dual-band applications. A parallel *L-C* and a series *L-C* take place of *L* and *C* paths in the single-band I/Q generator, as shown in Fig. 3-3. The parallel *L-C* section is inductive at low frequencies and capacitive at high frequencies. On the other hand, the series *L-C* section has the opposite properties. Hence, this topology satisfies the quadrature condition at a low frequency (ω_l) and a high frequency (ω_h).
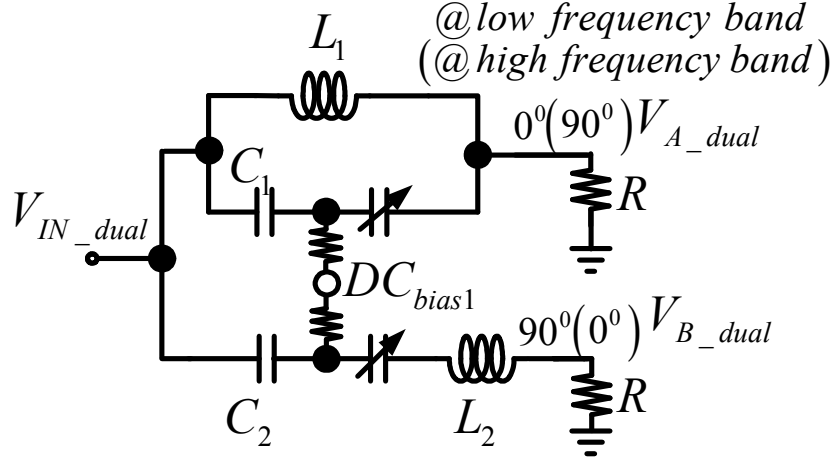
Fig. 3-3   Topology of the dual-band I/Q generator.

The capacitor in Fig. 3-3 is in series with a varactor to add the tuning ability in the I/Q generator to conquer the fabrication variation. For simplification in the analysis, the varactors are neglected. Based on the quadrature conditions,

$$\begin{cases} j\omega_l L_1 \mathbin{/\mkern-5mu/} \dfrac{1}{j\omega_l C_1} = jR \\[2mm] j\omega_l L_2 + \dfrac{1}{j\omega_l C_2} = -jR \\[2mm] j\omega_h L_1 \mathbin{/\mkern-5mu/} \dfrac{1}{j\omega_h C_1} = -jR \\[2mm] j\omega_h L_2 + \dfrac{1}{j\omega_h C_2} = jR \end{cases} \tag{3.5}$$

the inductance (L_1 and L_2) and capacitance (C_1 and C_2) are expressed in terms of ω_l, ω_h and R as follows:

$$L_1 = \frac{\omega_h - \omega_l}{\omega_l \omega_h} R \tag{3.6}$$

$$C_1 = \frac{1}{(\omega_h - \omega_l) R} \tag{3.7}$$

$$L_2 = \frac{1}{\omega_h - \omega_l} R \tag{3.8}$$

$$C_2 = \frac{\omega_h - \omega_l}{\omega_l \omega_h R}. \tag{3.9}$$

The input impedance of the dual-band I/Q generator is derived as

$$Z_{in\_dual} = \left(R + j\omega L_1 \text{ // } \frac{1}{j\omega C_1}\right) \text{ // } \left(R + j\omega L_2 + \frac{1}{j\omega C_2}\right)$$

$$= \frac{R^2 + \left(\dfrac{L_1}{C_2}\dfrac{1-\omega^2 L_2 C_2}{1-\omega^2 L_1 C_1}\right) + jR\left(\dfrac{\omega L_1}{1-\omega^2 L_1 C_1} - \dfrac{1-\omega^2 L_2 C_2}{\omega C_2}\right)}{2R + j\left(\dfrac{\omega L_1}{1-\omega^2 L_1 C_1} - \dfrac{1-\omega^2 L_2 C_2}{\omega C_2}\right)} \tag{3.10}$$

$$= R \qquad \text{when} \quad R = \sqrt{\frac{L_1}{C_2}} = \sqrt{\frac{L_2}{C_1}}$$

Under the condition of $R = (L_1/C_2)^{1/2} = (L_2/C_1)^{1/2}$, the input impedance is also equal to R regardless of frequencies and the wideband matching can be achieved [38]. The voltage ratio at node A_dual and B_dual in Fig. 3-3 can be expressed as

$$\frac{V_{A\_dual}}{V_{B\_dual}} = \frac{R - j\dfrac{1-\omega^2 L_2 C_2}{\omega C_2}}{R + j\dfrac{\omega L_1}{1-\omega^2 L_1 C_1}}$$

$$= \frac{\left(R^2 - \dfrac{L_1}{C_2}\dfrac{1-\omega^2 L_2 C_2}{1-\omega^2 L_1 C_1}\right) - jR\left(\dfrac{\omega L_1}{1-\omega^2 L_1 C_1} + \dfrac{1-\omega^2 L_2 C_2}{\omega C_2}\right)}{R^2 + \left(\dfrac{\omega L_1}{1-\omega^2 L_1 C_1}\right)^2} \tag{3.11}$$

and two nodes are always in quadrature regardless of frequencies when $R = (L_1/C_2)^{1/2} = (L_2/C_1)^{1/2}$.

In TABLE 3.1, the ideal inductance and capacitance of the dual-band I/Q generator are calculated for WLAN applications. Here, the quadrature condition is designed based on the matching condition ($R=50$ Ω). The inductance and capacitance are reasonable and the dual-band I/Q generator can be realized in WLAN systems. Fig. 3-4 represents the magnitude ratio ($|V_{A\_dual}/V_{B\_dual}|$) and phase error of the dual-band I/Q generator with respect to normalized frequency, $\omega_0 = \omega_l$, when $R = (L_1/C_2)^{1/2} = (L_1/C_2)^{1/2}$. For the 2.4/5.2 GHz application, $\omega_h = 2.167\omega_l$ and the magnitude error is smaller than 1 dB within the 0.96–1.04 and 2.08–2.27 normalized frequency. For the

2.4/5.7 GHz application, $\omega_h = 2.375\omega_l$ and the magnitude error is smaller than 1 dB within the 0.96–1.04 and 2.27–2.5 normalized frequency. At the transition frequency,

$$\omega_{transition} = \sqrt{\omega_l\omega_h} = \frac{1}{\sqrt{L_1C_1}} = \frac{1}{\sqrt{L_2C_2}}, \tag{3.12}$$

the parallel L-C network (L_1 and C_1) is open, while the series L-C network (L_2 and C_2) is short. All of the power flows to node B_dual. Therefore, the output magnitude ratio becomes zero and the phase reversal occurs.

TABLE 3.1 Calculated Inductance and Capacitance for Dual-Band Wi-Fi I/Q Generators.

ω_l(GHz)/ω_h(GHz)/$R(\Omega)$	L_1(nH)	L_2(nH)	C_1(pF)	C_2(pF)
2.4/ 5.2/ 50	1.785	2.842	1.137	0.714
2.4/ 5.7/ 50	1.92	2.411	0.965	0.768
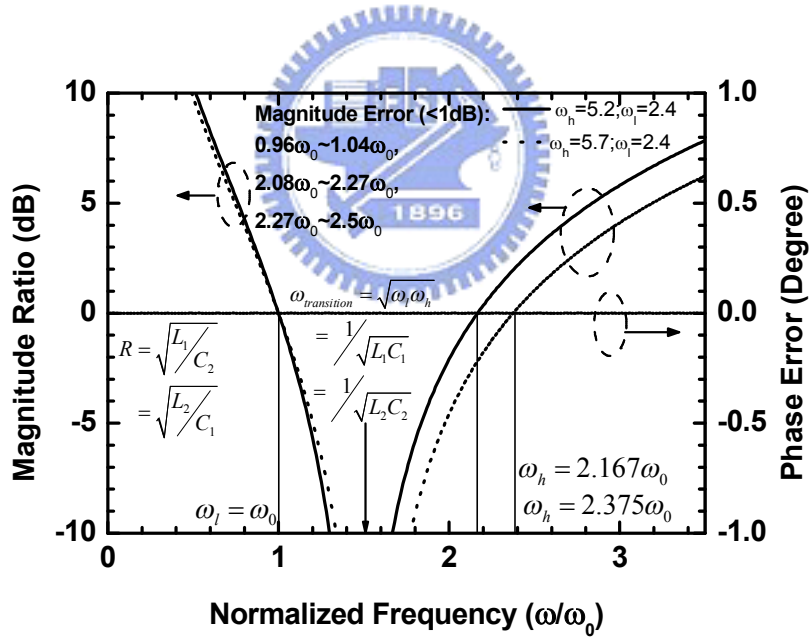
Fig. 3-4   Magnitude ratio ($|\,V_{A\_dual}/V_{B\_dual}\,|$) and phase error of the dual-band reactive I/Q generator with respect to normalized frequency $\omega_0 = \omega_l$.

In comparison with a polyphase filter, there are several advantages in this reactive I/Q generator, which are listed below.

1) The generator has low loss because of the absence of resistors and is suitable for

high-frequency applications.

2) *Zin=R*, and the input matching condition is determined by the input impedance of the following circuits. Hence, it is possible to achieve the wideband matching.

3) By increasing the order of the *L-C* networks, it is easy to construct a multiband quadrature generator.

3.3 CIRCUIT DESIGN

The proposed dual-band adjustable I/Q generator is employed at the LO stage in an I/Q down-converter and an SSB up-converter. The entire schematics of the I/Q down-converter and the SSB up-converter are depicted in Fig. 3-5 and Fig. 3-6, respectively. The mixer topology is a micromixer, which has the wideband input matching property [15], [21], [39]. Thus, the micromixer is suitable for multiband or wideband applications. The quadrature differential LO signals are generated by the dual-band reactive I/Q generator and two single-to-differential amplifiers. Here, the single-to-differential input stage of the micromixer is adopted in the single-to-differential amplifier. Thus, the input impedance of the single-to-differential amplifier also serves as the loading impedance of the I/Q generator *R*. The emitter followers are employed as output buffers to drive 50 Ω measurement equipments. The circuit topologies of the down- and up-converters are very similar, except the connection in the mixer outputs.

The phase property of LO signals is changed between dual bands, which alternates the quadrature property of the down-converter and the sideband property of the up-converter, as shown in Fig. 3-5 and Fig. 3-6. In the up-converter, the RF output signal of the low-frequency band is located at the upper sideband while that of the high-frequency band is located at the lower sideband.
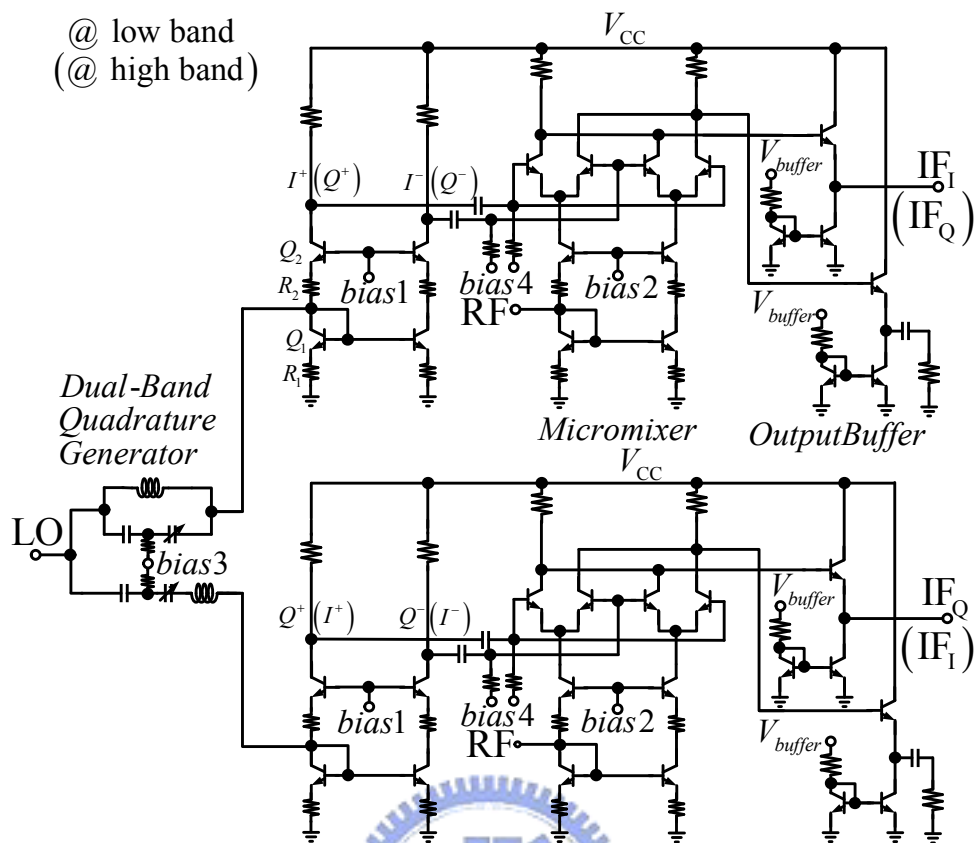
Fig. 3-5   Schematic of the dual-band I/Q down-converter.
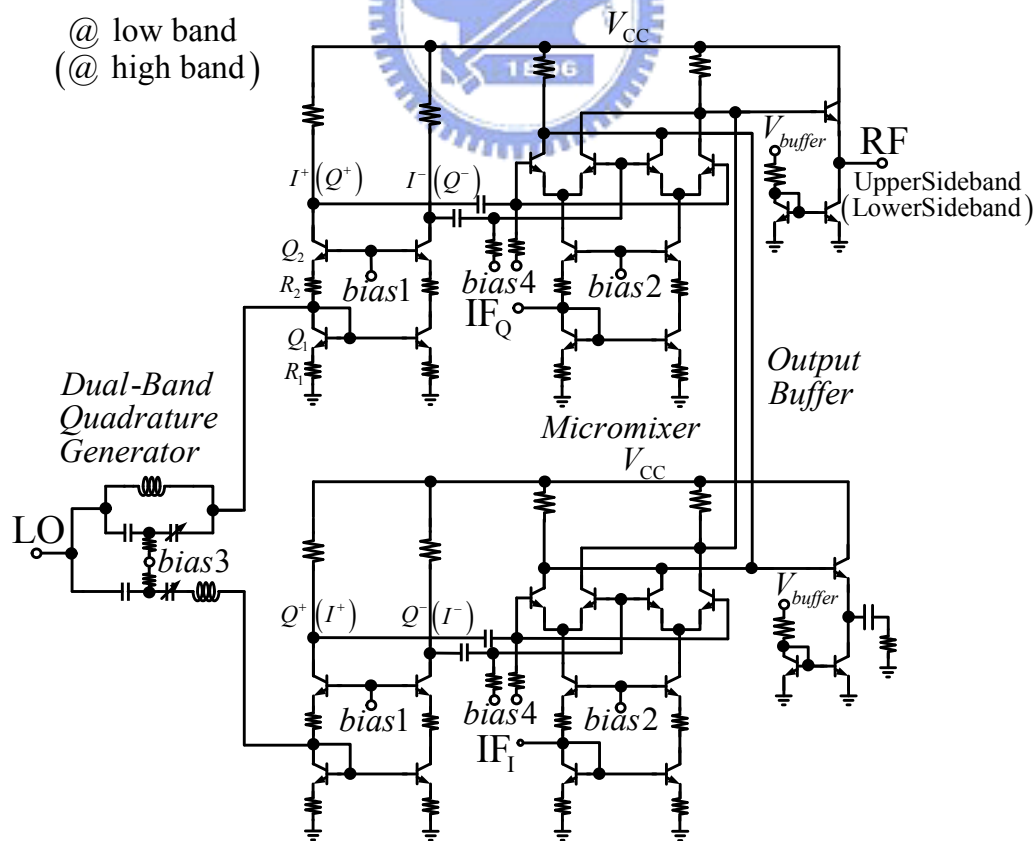
Fig. 3-6   Schematic of the dual-band SSB up-converter.

The adjustable mechanism is added to overcome the inductance and capacitance variations in IC fabrication. Fig. 3-7 illustrates four I/Q mismatch conditions. A and B denote the impedance of inductive ($R+j\omega L$) and capacitive ($R+1/j\omega C$) sections, respectively. Obviously, the magnitude difference can be controlled by varactors as the quadrature phase is determined by the input impedance of the amplifier R, where the input impedance of the single-to-differential converter is approximately $(1/gm_1+R_1)//(1/gm_2+R_2)$. Thus, the bias of the amplifier can control current and then the input impedance. TABLE 3.2 summarizes the configurations for four I/Q mismatch conditions, where Z_{CAP} is the impedance of the varactor.

(a) $|A|<|B|$ & $\angle AB < 90^0$ (b) $|A|>|B|$ & $\angle AB < 90^0$

(c) $|A|<|B|$ & $\angle AB > 90^0$ (d) $|A|>|B|$ & $\angle AB > 90^0$
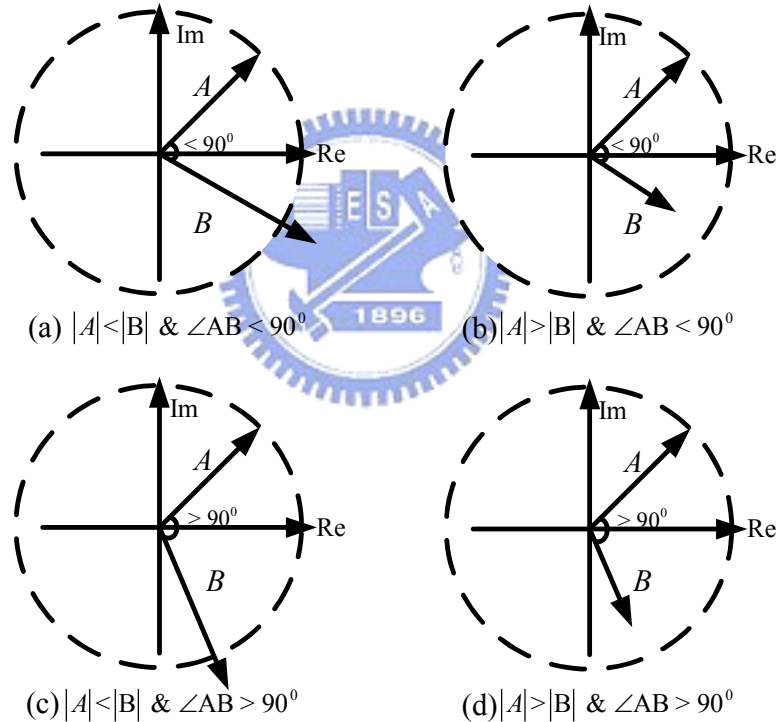
Fig. 3-7   Four types of I/Q mismatch conditions.

TABLE 3.2 Adjustable Mechanism for Four I/Q Mismatch Conditions.

I/Q mismatch conditions	R	Z_{CAP}
$|A|<|B|$ & $\angle AB < 90^0$	↘	↘
$|A|>|B|$ & $\angle AB < 90^0$	↘	↗
$|A|<|B|$ & $\angle AB > 90^0$	↗	↘
$|A|>|B|$ & $\angle AB > 90^0$	↗	↗

3.4 MEASUREMENT RESULTS

A dual-band I/Q down-converter and a dual-band SSB up-converter are fabricated using the 0.35-μm SiGe BiCMOS process [40]. Both mixers utilize the dual-band adjustable and reactive I/Q generators to provide accurate quadrature LO signals. The die photographs are displayed in Fig. 3-8 (a) and (b), respectively. The dual-band LO I/Q generator occupies the estate of 600 μm × 300 μm. By the simulation, the loss of the reactive I/Q generator is less than 2 dB from the metal loss and substrate loss.
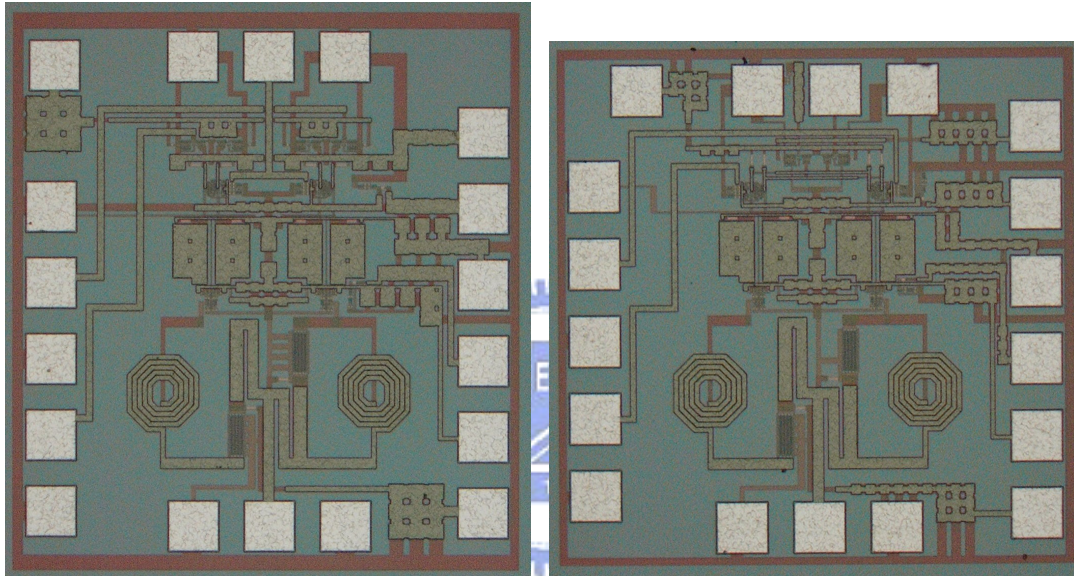
(a) Dual-band I/Q down-conversion mixer   (b) Dual-band SSB up-conversion mixer

Fig. 3-8   Die photographs of (a) the 2.4/5.2-GHz I/Q down-conversion mixer and (b) the 2.4/5.7-GHz SSB up-conversion mixer.

3.4.1 *2.4 GHz and 5.2 GHz I/Q Down-Converter*

This down-conversion mixer operates at 2.4/5.2 GHz with the voltage supply of 3.3 V. The capacitances of the I/Q generator is varied by tuning the varactor capacitance, and hence, the optimal performance is achieved. The power consumption of the down-converter at 2.4 GHz and 5.2 GHz is 37.9 and 33.3 mW, respectively.

The conversion gain of I and Q channels is dependent on the LO frequency, as shown in Fig. 3-9. The matched point between I and Q channels occurs at 2.4 and 5.2

GHz. The conversion gain at 2.4/5.2 GHz is approximately 5.2/1.2 dB. At frequency below the matched point frequency, the inductive path of the I/Q generator obtains more power than capacitive path does. Therefore, the I-channel conversion gain is higher. On the contrary, at frequency above the matched point frequency, the Q-channel down-converter has a higher conversion gain.
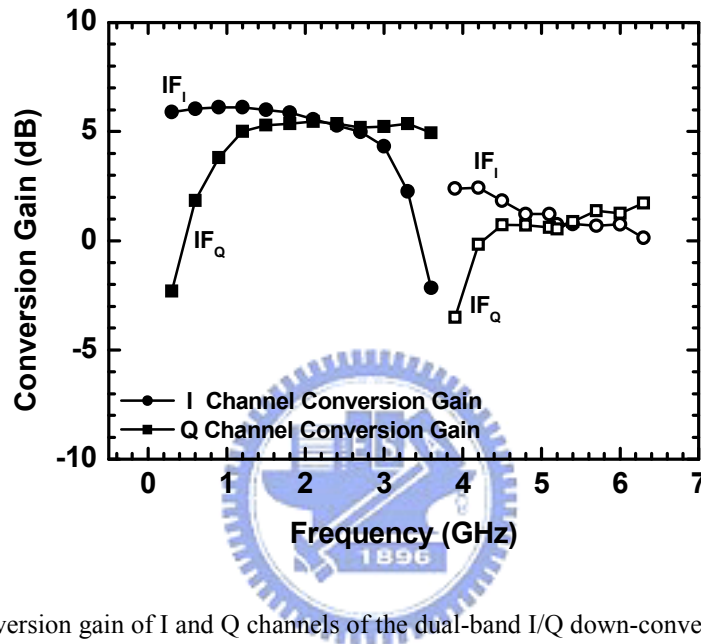
Fig. 3-9   Conversion gain of I and Q channels of the dual-band I/Q down-conversion mixer.

At 2.4 GHz, the mixer is driven with LO power of -3 dBm and has -10.5-dBm IP_{1dB}, -2-dBm IIP_3, 900-MHz 3-dB IF bandwidth, -21.65-dB RF input return loss, -12.45-dB LO input return loss, -9.71-dB IF input return loss and 19-dB noise figure. The LO input port is single-ended. The reactive I/Q generators is lossless and does not increase the LO driven power. The rms magnitude error is approximately 0.204% and phase error is approximately 0.2°, which shows excellent orthogonal property of two outputs. Since the quadrature mechanism is decided by the LO quadrature generator, the IF outputs are in quadrature within all of IF frequencies.

At 5.2 GHz, the RF, LO, and IF return loss of the mixer are -17.3, -11.78, and

-10.28 dB, respectively. The IP_{1dB} and IIP_3 are -9.5 and -0.5 dBm, respectively. The LO power is 0.1 dBm. The 3-dB IF bandwidth is the same as that at 2.4 GHz. The noise figure is approximately 21 dB. This I/Q mixer has 0.944% gain mismatch and 0.68° phase error at 5.2-GHz RF frequency. Fig. 3-10 describes the output phase and amplitude balance with respect to RF frequency. The phase error is small than 1° over entire frequency range and is limited by the measurement accuracy of ±0.5° phase and ±0.1-dB amplitude error. The measurement results agree with the discussion in Section 3.2.2. The phase difference is always in quadrature and the phase reversal occurs at the transition frequency of around 3.6 GHz. Within ±0.5 dB output magnitude imbalance and 1° phase error, this down-converter works from 1.8 to 2.8 GHz and from 4.8 to 5.6 GHz for each band. The operation bandwidth of the mixer is larger than that of the reactive I/Q generator because the conversion gain keeps constant and is insensitive to the LO power as long as the LO power is large enough to switch the Gilbert cell [21]. As shown in Fig. 3-11, the LO-to-IF, RF-to-IF, and LO-to-RF isolations are below -35, -15, and -45 dB, respectively.
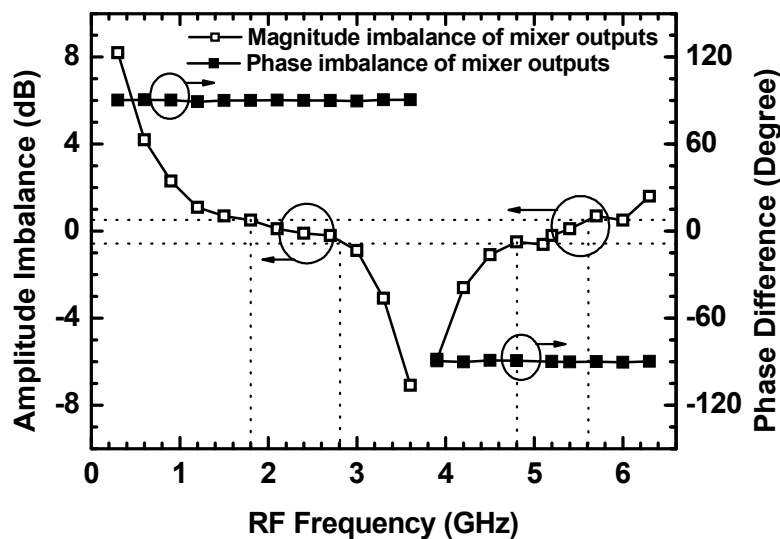
Fig. 3-10   Output phase and amplitude balance for the dual-band I/Q downconverter.
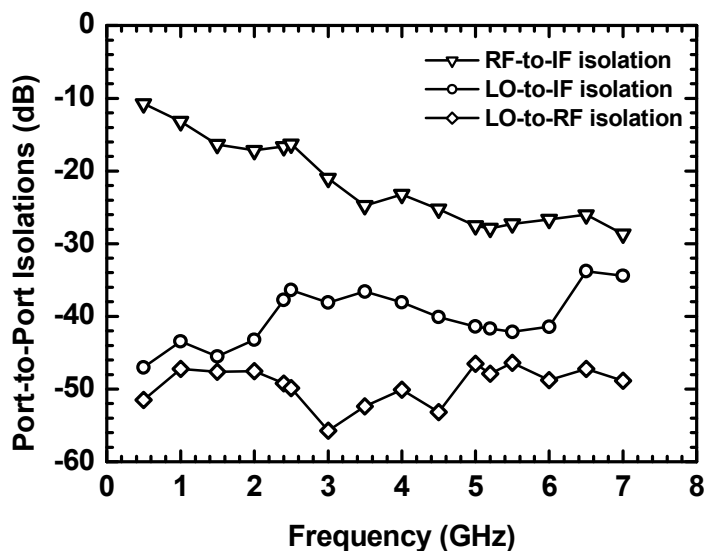
Fig. 3-11   Port-to-port isolations of the dual-band I/Q downconverter.

3.4.2 *2.4 GHz and 5.7 GHz SSB Up-Converter*

The dual-band adjustable and reactive I/Q generator is also employed in the 2.4/5.7 GHz SSB up-converter. As shown in Fig. 3-12, the conversion gain at 2.4 and 5.7 GHz are 0.5 and -2.2 dB, respectively. The peaks of the SSB rejection ratio occur at 2.4 and 5.7 GHz. The peak values at 2.4 GHz and 5.7 GHz are 52.59 and 62.85 dB, respectively. The sideband rejection bandwidth (>30dB rejection ratio) is approximately 200 MHz at 2.4 GHz and 700 MHz at 5.7 GHz. The 30-dB sideband rejection ratio represents approximately 0.6-dB magnitude error with perfect quadrature phase [41]. The output signal is located at the upper sideband at the 2.4 GHz and located at the lower sideband at 5.7 GHz as shown in Fig. 3-13 and Fig. 3-14 because the phase property of the I/Q generator between 2.4 and 5.7 GHz is exchanged. The transition frequency is approximately 3.7 GHz. The performance of the sideband rejection is very sensitive to the phase and amplitude balance of the I/Q generator. The high sideband rejection ratio performance reveals that this adjustable

and reactive I/Q generator can provide excellent quadrature outputs with equal power

for dual-band applications.
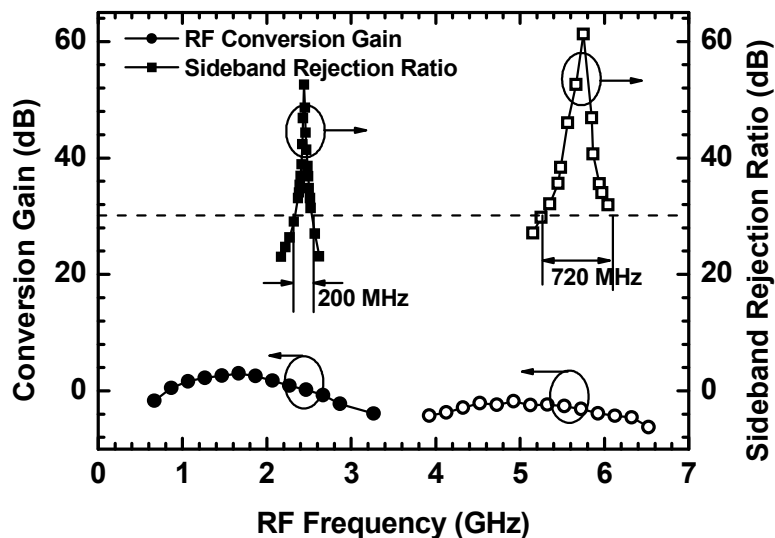
Fig. 3-12   Conversion gain and sideband rejection ratio of the up-converter.
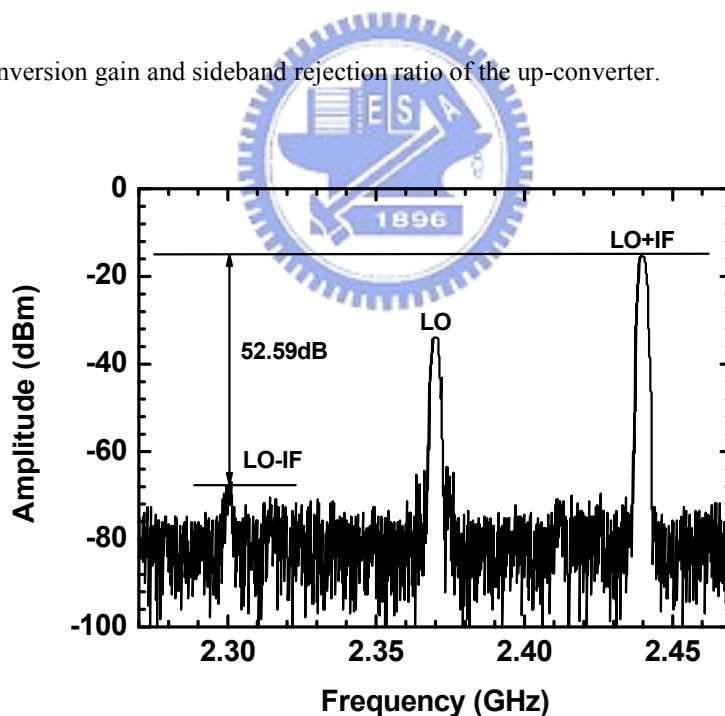
Fig. 3-13   Output spectrum of the dual-band SSB up-converter at 2.4 GHz. The side-band rejection ratio is 52.59 dB.
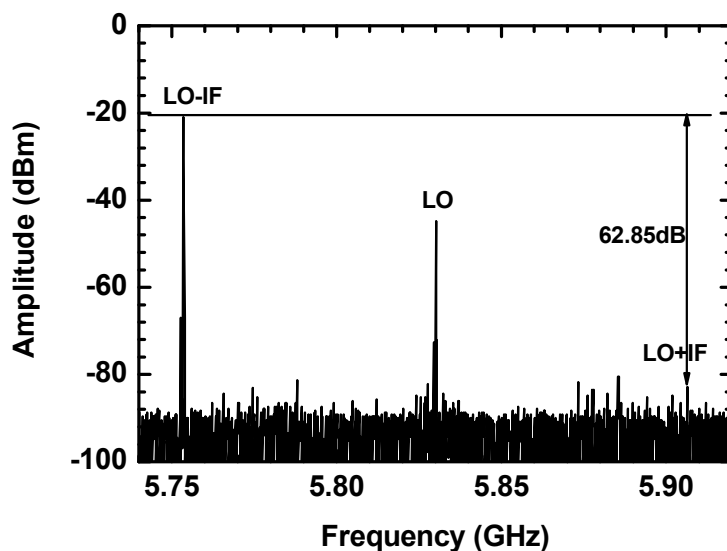
Fig. 3-14   Output spectrum of the dual-band SSB up-converter at 5.7 GHz. The side-band rejection ratio is 62.85 dB.
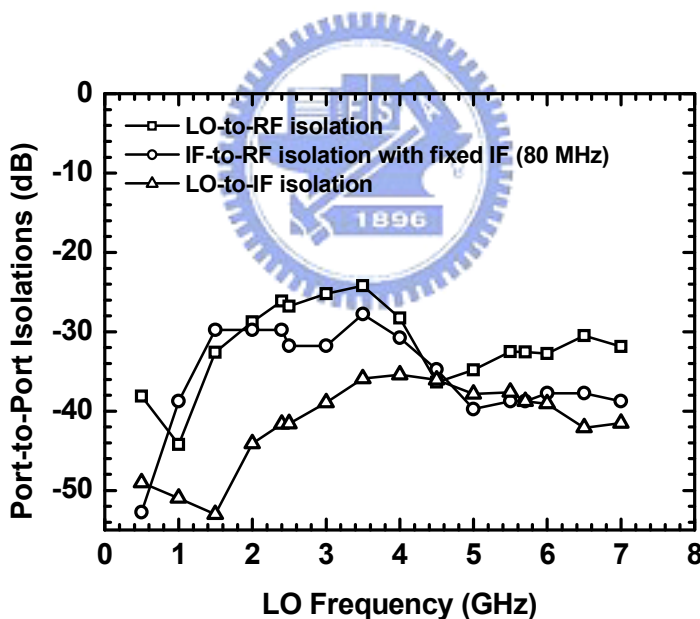
Fig. 3-15   Port-to-port isolations of the dual-band SSB up-converter.

At 2.4-GHz RF frequency, with the LO power of -2.5 dBm, the mixer has OP_{1dB} of -7 dBm, OIP_3 of 4 dBm, and the total power consumption of 38 mW. At 5.7 GHz, with the LO power of 7.5 dBm, the mixer has OP_{1dB} of -6.5 dBm and OIP_3 of 4 dBm. Fig. 3-15 illustrates the LO-to-RF and IF-to-RF isolations. The LO-to-RF isolation is

below -24 dB and the IF-to-RF isolation measured with the fixed IF of 80 MHz is below -28 dB. In addition, the LO-to-IF isolation is approximately -41 and -38 dB for 2.4- and 5.7-GHz bands, respectively.

The LO return loss of the dual-band I/Q down-converter and SSB up-converter is displayed in Fig. 3-16. Obviously, the wideband matching is achieved as expected because of the constant resistance property of the dual-band I/Q generator. TABLE 3.3 summarizes the measured performance of both mixers. According to the measured results, this dual-band adjustable and reactive I/Q generator has optimal quadrature performance to achieve excellent quadrature outputs for a down- conversion mixer and high sideband rejection ratio for an up-converter. Compared with a polyphase filter, this reactive I/Q generator has no resistive loss and achieves dual-band operations easily.
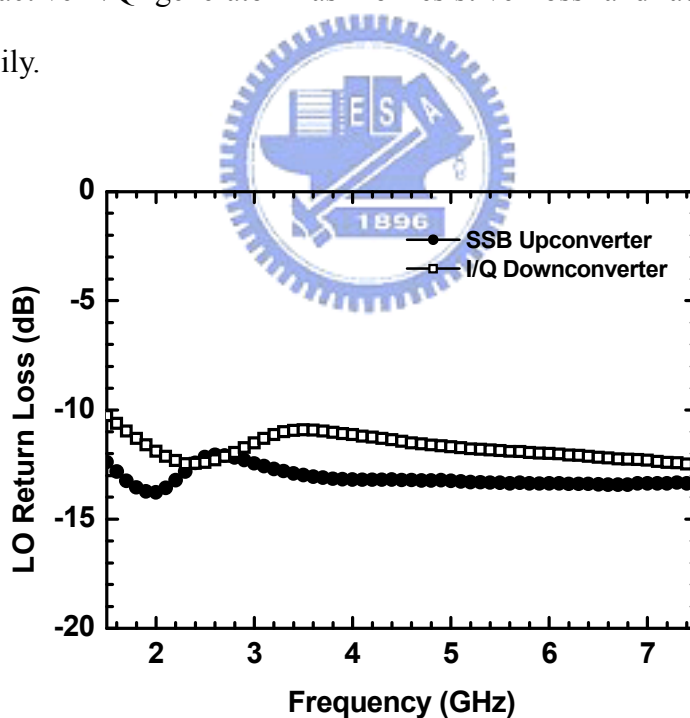
Fig. 3-16 LO return loss of the dual-band I/Q down-converter and SSB up-converter.

TABLE 3.3 Measurement Results of the Tunable Dual-Band I/Q Down-Converter and SSB Up-Converter

TSMC 0.35µm 3P3M SiGe BiCMOS				
Item	UP		DOWN	
Frequency	2.4 GHz	5.7 GHz	2.4 GHz	5.2 GHz
Conversion Gain	0.5 dB	-2.2dB	5.2dB	1.2 dB
LO Power	-2.5 dBm	7.5 dBm	-3 dBm	0.1 dBm
I/O P_{1dB}	-7 dBm	-6.5 dBm	-10.5 dBm	-9.5 dBm
I/O IP_3	4 dBm	4 dBm	-2 dBm	-0.5 dBm
Sideband Rejection Ratio Bandwidth (>30dB)	200 MHz	720 MHz		
Max. Sideband Rejection Ratio	52.59 dB	62.85 dB		
RF Operation Frequency (errors<0.5dB, <1°)			1.8~2.8 GHz	4.8~5.6 GHz
Magnitude Imbalance			0.204%	0.944%
Phase Error			0.2°	0.68°
RF Return Loss	-4.62 dB	-4.7 dB	-21.65 dB	-17.31 dB
LO Return Loss	-12.4 dB	-13.4 dB	-12.45 dB	-11.78 dB
IF Return Loss	-10.8 dB	-13.3 dB	-9.71 dB	-10.28 dB
Noise Figure			19 dB	21 dB
Supply Voltage	3.3 V			
Total Power Dissipation	38 mW	36 mW	37.9 mW	33.3 mW
Chip Size	1 mm × 1 mm		1 mm × 1.1 mm	

3.5 SUMMARY

This dissertation proposes a dual-band adjustable I/Q generator with quadrature phase property and constant input resistance at all frequencies. Dual band is achieved because the magnitude balance of the I/Q generator occurs at two designed frequencies. The 2.4/5.2 GHz I/Q down-converter and 2.4/5.7 GHz SSB up-converter implemented using 0.35-µm SiGe BiCMOS present the excellent quadrature performance of the dual-band adjustable I/Q generator. In comparison with the polyphase filter, there is no resistive loss in this generator and multiband quadrature mechanism is feasible by increasing the order of the *L-C* networks.

Chapter 4 Silicon Monolithic Phase-Inverter Rat-Race Coupler Using Spiral CPSs

4.1 INTRODUCTION

Fig. 4-1 displays the evolution of the rat-race coupler. A rat-race coupler is a commonly used four-port passive component, with three one-quarter-wavelength and one three-quarter-wavelength transmission lines. The three-quarter-wavelength segment offers a 180° phase delay to generate differential signals at the neighboring ports and to cancel signal at the opposite isolation port. These properties are achieved at a specified frequency, and thus, the bandwidth is limited. In the case of the uniplanar transmission line, there exists an effective way to minimize the size and to extend the bandwidth simultaneously for the rat-race coupler. A phase inverter is employed in the middle of the quarter-wavelength transmission line to replace the three-quarter-wavelength section, as shown in Fig. 4-1 [42]–[46]. On account of the wideband and low loss properties of the phase inverter, the operation bandwidth of a phase-inverter rat-race coupler is very large. This rat-race coupler maintains balanced output signals regardless of the substrate loss, thanks to the equal path loss. Couplers had been realized on the silicon substrate, but most of them are created with substrate shielding [47], [48], which results in a low effective dielectric constant, and thus, a large coupler size. It is advantageous to implement the coupler directly on the silicon substrate for size reduction by the higher effective dielectric constant. The finite-ground coplanar waveguide (FGCPW) phase-inverter rat-race couplers directly on the silicon substrate had been implemented at 60 and 77 GHz [49], and size-reduction techniques were applied at the cost of the bandwidth even at such high frequencies [42].
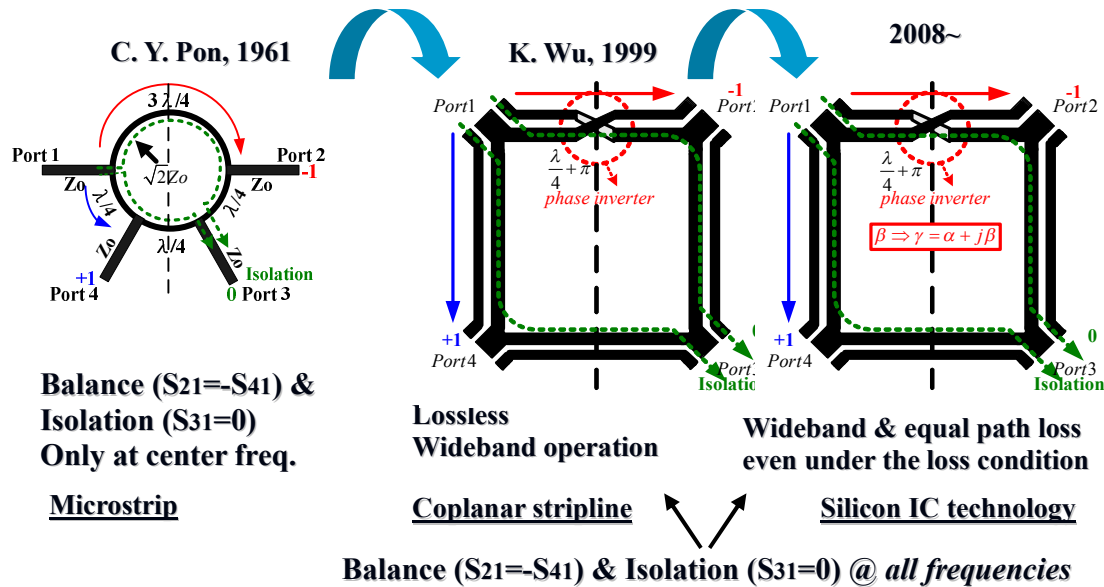
Fig. 4-1   Rat-race coupler evolution.

In this study, the balanced structure of passive components is analyzed and designed to mitigate the influence of the substrate loss by means of using two signal paths with equal loss. This research focuses on a uniplanar transmission line rat-race coupler implemented directly on lossy silicon substrate. Here, the uniplanar transmission lines—coplanar waveguides (CPWs) and coplanar striplines (CPSs)—demand few metal layers and have the higher effective dielectric constant for size reduction when compared with microstrip lines formed by the inter-metal dielectric, sandwiched by the top metal and the bottom shielding ground metal [47], [48], [50]. In addition, spiral-shaped CPSs are also employed to shrink the size. A phase-inverter rat-race coupler using symmetrical spiral CPSs is implemented directly on a low-resistivity (~10 Ω·cm) standard silicon substrate in this work. The phase inverter in the rat-race coupler is the key element to keep outputs balanced by providing the equal-length lossy paths, and thus, the phase-inverter rat-race coupler preserves the broadband properties even in the presence of lossy silicon substrate. In addition, the lossy CPS is designed as a distortionless transmission line to have a

nondispersive and real characteristic impedance for broad bandwidth and perfect port-matching of the coupler. This chapter also demonstrated a wideband Gilbert mixer with this integrated coupler using a 0.35-μm SiGe BiCMOS process. The integrated wideband phase-inverter rat-race coupler can eliminate the problem of poor differential signals caused by the mismatch of the external balun and cables.

4.2 ANALYSIS AND DESIGN OF RAT-RACE COUPLERS WITH A PHASE INVERTER

A spiral-shaped CPS is applied for size reduction to the phase-inverter rat-race coupler directly on the standard silicon substrate at a low frequency regime without any compromise in the bandwidth. Moreover, the phase-inverter rat-race coupler is analyzed under the lossy condition and a distortionless transmission-line design methodology is developed for the simple port-matching condition. Many previous analyses have focused on a lossless rat-race coupler [42]. Here, the even- and odd-mode analyses are applied to analyze a lossy rat-race coupler with a phase inverter, as shown in Fig. 4-2 [51]. Ports 1 and 3 are the delta and sum ports, respectively. The length and the complex propagation constant of the transmission lines, A and B, in Fig. 4-2(a) are denoted as ℓ_a, γ_a, ℓ_b, and γ_b, respectively. The normalized characteristic impedances $\hat{z}_a$ and $\hat{z}_b$ of the transmission lines, with respect to the terminal impedance Z_0 are, in general, complex as described in reference [21]. The even-mode network consists of a transmission line with one short shunt stub and one open shunt stub on two sides and this network becomes the odd-mode network by exchanging two shunt stubs, as shown in Fig. 4-2(b) and (c).
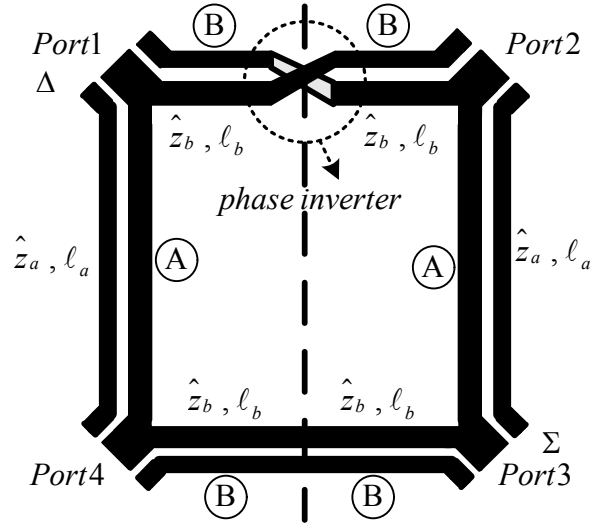
(a) Phase-inverter rat-race coupler
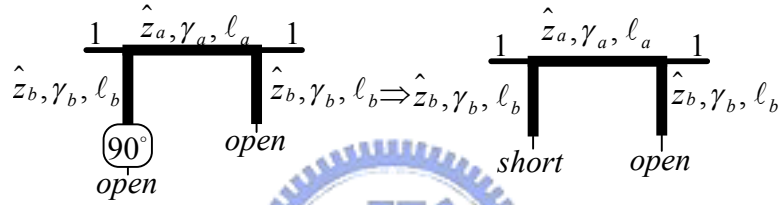
(b) Even mode of the phase-inverter rat-race coupler
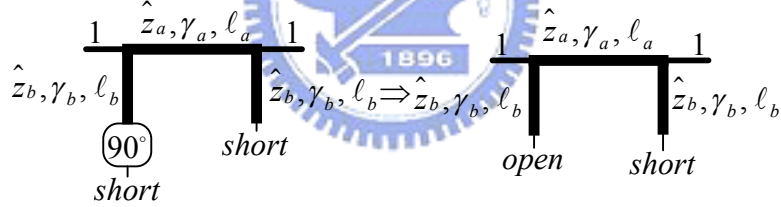
(c) Odd mode of the phase-inverter rat-race coupler

Fig. 4-2   Even- and odd-mode analyses of a phase-inverter rat-race coupler.

The even- and odd-mode *ABCD* matrices are then derived as

$$\begin{bmatrix} A & B \\ C & D \end{bmatrix}_e = \begin{bmatrix} 1 & 0 \\ \dfrac{1}{\hat{z}_b}\coth(\gamma_b\ell_b) & 1 \end{bmatrix}\begin{bmatrix} \cosh(\gamma_a\ell_a) & \hat{z}_a\sinh(\gamma_a\ell_a) \\ \dfrac{1}{\hat{z}_a}\sinh(\gamma_a\ell_a) & \cosh(\gamma_a\ell_a) \end{bmatrix}\begin{bmatrix} 1 & 0 \\ \dfrac{1}{\hat{z}_b}\tanh(\gamma_b\ell_b) & 1 \end{bmatrix} \quad (4.1)$$

$$= \begin{bmatrix} a & b \\ c & d \end{bmatrix}$$

and

$$\begin{bmatrix} A & B \\ C & D \end{bmatrix}_o = \begin{bmatrix} 1 & 0 \\ \dfrac{1}{\hat{z}_b}\tanh(\gamma_b\ell_b) & 1 \end{bmatrix} \begin{bmatrix} \cosh(\gamma_a\ell_a) & \hat{z}_a\sinh(\gamma_a\ell_a) \\ \dfrac{1}{\hat{z}_a}\sinh(\gamma_a\ell_a) & \cosh(\gamma_a\ell_a) \end{bmatrix} \begin{bmatrix} 1 & 0 \\ \dfrac{1}{\hat{z}_b}\coth(\gamma_b\ell_b) & 1 \end{bmatrix} \quad (4.2)$$

$$= \begin{bmatrix} d & b \\ c & a \end{bmatrix}$$

respectively, where

$$a = \cosh(\gamma_a\ell_a) + \frac{\hat{z}_a}{\hat{z}_b}\tanh(\gamma_b\ell_b)\sinh(\gamma_a\ell_a)$$

$$b = \hat{z}_a\sinh(\gamma_a\ell_a)$$

$$c = \frac{1}{\hat{z}_b}\cosh(\gamma_a\ell_a)[\tanh(\gamma_b\ell_b)+\coth(\gamma_b\ell_b)]+\sinh(\gamma_a\ell_a)[\frac{1}{\hat{z}_a}+\frac{\hat{z}_a}{\hat{z}_b^2}] \qquad (4.3)$$

$$d = \cosh(\gamma_a\ell_a) + \frac{\hat{z}_a}{\hat{z}_b}\coth(\gamma_b\ell_b)\sinh(\gamma_a\ell_a)$$

Deriving from the even- and odd-mode *ABCD* matrices, the *S*-parameter matrix of the

phase-inverter rat-race coupler can be written as

$$[S] = \frac{1}{a+b+c+d}\begin{bmatrix} b-c & a-d & 0 & 2 \\ a-d & b-c & 2 & 0 \\ 0 & 2 & b-c & d-a \\ 2 & 0 & d-a & b-c \end{bmatrix} = \begin{bmatrix} S_{11} & S_{21} & S_{31} & S_{41} \\ S_{21} & S_{11} & S_{41} & S_{31} \\ S_{31} & S_{41} & S_{11} & -S_{21} \\ S_{41} & S_{31} & -S_{21} & S_{11} \end{bmatrix}. \qquad (4.4)$$

where S_{11}, S_{21}, S_{31}, and S_{41} are expressed as

$$S_{11} = \frac{\sinh(\gamma_a\ell_a)(\hat{z}_a - 1/\hat{z}_a - \hat{z}_a/\hat{z}_b^2) - 1/\hat{z}_b\cosh(\gamma_a\ell_a)[\tanh(\gamma_b\ell_b)+\coth(\gamma_b\ell_b)]}{2\cosh(\gamma_a\ell_a)+1/\hat{z}_b[\hat{z}_a\sinh(\gamma_a\ell_a)+\cosh(\gamma_a\ell_a)][\tanh(\gamma_b\ell_b)+\coth(\gamma_b\ell_b)]+\sinh(\gamma_a\ell_a)[\hat{z}_a+1/\hat{z}_a+\hat{z}_a/\hat{z}_b^2]}$$

$$S_{21} = \frac{\dfrac{\hat{z}_a}{\hat{z}_b}\sinh(\gamma_a\ell_a)[\tanh(\gamma_b\ell_b)-\coth(\gamma_b\ell_b)]}{2\cosh(\gamma_a\ell_a)+1/\hat{z}_b[\hat{z}_a\sinh(\gamma_a\ell_a)+\cosh(\gamma_a\ell_a)][\tanh(\gamma_b\ell_b)+\coth(\gamma_b\ell_b)]+\sinh(\gamma_a\ell_a)[\hat{z}_a+1/\hat{z}_a+\hat{z}_a/\hat{z}_b^2]}$$

$$S_{31} = 0$$

$$S_{41} = \frac{2}{2\cosh(\gamma_a\ell_a)+1/\hat{z}_b[\hat{z}_a\sinh(\gamma_a\ell_a)+\cosh(\gamma_a\ell_a)][\tanh(\gamma_b\ell_b)+\coth(\gamma_b\ell_b)]+\sinh(\gamma_a\ell_a)[\hat{z}_a+1/\hat{z}_a+\hat{z}_a/\hat{z}_b^2]}$$

$$(4.5)$$

Under the design conditions that $\ell_a = 2\ell_b = \ell$, $\hat{z}_a = \hat{z}_b = \hat{z}$, and

$\gamma_a = \gamma_b = \alpha + j\beta$, S_{21} is equal to -S_{41} no matter what the operation frequency is, as is

derived from Appendix A. Obviously, the phase inverter is properly employed to keep

the signal lossy paths equal so that the differential outputs of the coupler maintain balance in magnitude and phase. In the case of no loss, the *S*-parameters are the same as the *S*-parameters derived in [42].

According to the derivation shown in Appendix B, the perfect port-matching is achieved at the center frequency with the wavelength $\ell = \lambda/4$ when the normalized characteristic impedance of the rat-race coupler is equal to

$$\hat{z} = \frac{\sqrt{2\cosh\left(\lambda\alpha/2\right)}}{\cosh\left(\lambda\alpha/4\right)} . \tag{4.6}$$

The normalized characteristic impedance $\hat{z}$ is a function of $\lambda\alpha$, and the minimum and maximum values are $\sqrt{2}$ and 2, respectively. Fig. 4-3 reveals that the characteristic impedance for perfect matching is always a real number, which occurs only under the lossless or distortionless conditions [52]. Therefore, the transmission line is designed as a near distortionless line in our study to achieve perfect matching. Theoretically, S_{21} is equal to $-S_{41}$. The bandwidth of the coupler is limited by the matching condition. In order to extend the bandwidth, the perfect port matching could be designed at more frequencies around the center frequency, as mentioned in [46]. Nevertheless, the lossy coupler has broader input matching than the lossless counterpart, because of the degradation of the quality factor of the transmission line. The rat-race coupler is directly implemented on a lossy substrate for a compact size, and the dielectric loss is dominant. The loss is proportional to the length of the transmission line. For high-frequency applications, a shorter transmission line length reduces loss. As is derived from Appendix B, the transmission coefficient S_{21}, at the center frequency, can be expressed in terms of $\lambda\alpha$

$$|S_{21}| = -20\log_{10}\left[2\sinh\left(\frac{\lambda\alpha}{4}\right) + \sqrt{2\cosh\left(\frac{\lambda\alpha}{2}\right)}\right] \ (dB).$$

(4.7)

As shown in Fig. 4-3, with the same attenuation constant, α=2.1cm^{-1}, the transmission coefficient S_{21} becomes -7.55, -5.32 and -4.17 dB, at the operation frequency of 15, 30, and 60 GHz, respectively. This loss at 60 GHz is consistent with [49]. Our proposed rat-race coupler directly on a low-resistivity substrate is more suitable at higher frequencies. A lumped-element technique is also useful to shorten the length and then to lessen the loss at the cost of the operation bandwidth. Though a high coupler loss occurs for low-frequency applications, the coupler is useful to provide wideband differential signals to the LO port of a Gilbert mixer. This is because the differential pair of the bipolar/MOS Gilbert cell needs a small twist voltage to commutate an RF current. However, the lossy coupler is not appropriate for diode mixers, which demand large LO pumping power. Besides, the coupler is not useful to be employed in the RF port of a down-converter because the high coupler loss results in a high noise figure.
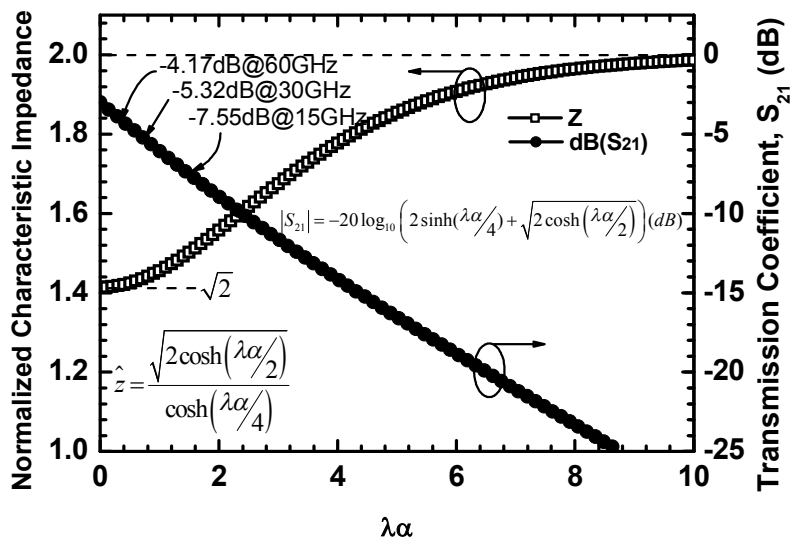
Fig. 4-3   Normalized characteristic impedance and transmission coefficient with respect to $\lambda\alpha$ for perfect matching.

Fig. 4-4 shows the layout of the phase-inverter CPS rat-race coupler. Quarter-wavelength CPSs are winding into a symmetrical spiral shape to condense the estate of the coupler. In addition, the phase inverter is easily established in the middle of the symmetrical spiral-shaped CPSs to provide a 180° phase shift, as shown in Fig. 4-4. The physical size of the phase inverter should be negligible when compared with the operating wavelength. The transmission line can be modeled in terms of the per-unit-length resistance R_0, inductance L_0, conductance G_0, and capacitance C_0 [52]. The transmission-line parameters are extracted from the electromagnetic (EM)-simulated S-parameters [53],

$$\gamma = \frac{1}{\ell} \ln\left(\frac{1 - S_{11}^2 + S_{21}^2}{2S_{21}} \pm K \right) = \sqrt{(R_0 + j\omega L_0)(G_0 + j\omega C_0)} \tag{4.8}$$

and

$$Z = Z_0 \sqrt{\frac{(1 + S_{11})^2 - S_{21}^2}{(1 - S_{11})^2 - S_{21}^2}} = \sqrt{\frac{R_0 + j\omega L_0}{G_0 + j\omega C_0}} \tag{4.9}$$

where

$$K = \sqrt{\frac{(S_{11}^2 - S_{21}^2 + 1)^2 - 4S_{11}^2}{4S_{21}^2}} . \tag{4.10}$$

Then,

$$\begin{cases} R_0 = \mathrm{Re}\{\gamma Z\} \\ L_0 = \dfrac{\mathrm{Im}\{\gamma Z\}}{\omega} \\ G_0 = \mathrm{Re}\left\{\dfrac{\gamma}{Z}\right\} \\ C_0 = \dfrac{\mathrm{Im}\left\{\dfrac{\gamma}{Z}\right\}}{\omega} \end{cases} . \tag{4.11}$$

For a fixed CPS gap, R_0 decreases with the CPS width increase, so that the

distortionless condition is achieved by controlling the metal width. The characteristic impedance for the matching condition varies smoothly from $\sqrt{2}Z_0$ to $2Z_0$. Thus, the transmission-line impedance approaches the characteristic impedance for the matching condition of a proper CPS gap. With this systematic design, the input matching and distortionless property are achieved approximately at the same time. Wave propagates well in straight CPSs. However, coupling occurs at the bends of the spiral-shaped lines. The spacing between adjacent CPSs is a trade-off between layout size and coupling. The optimal spacing between adjacent CPSs from the simulations is close to the CPS line-to-line spacing. Moreover, the bends in the spiral-shaped CPSs are a small proportion of entire quarter-wavelength transmission lines, and hence the change of impedance or transmission-line parameters of this section can be neglected from the EM simulations.
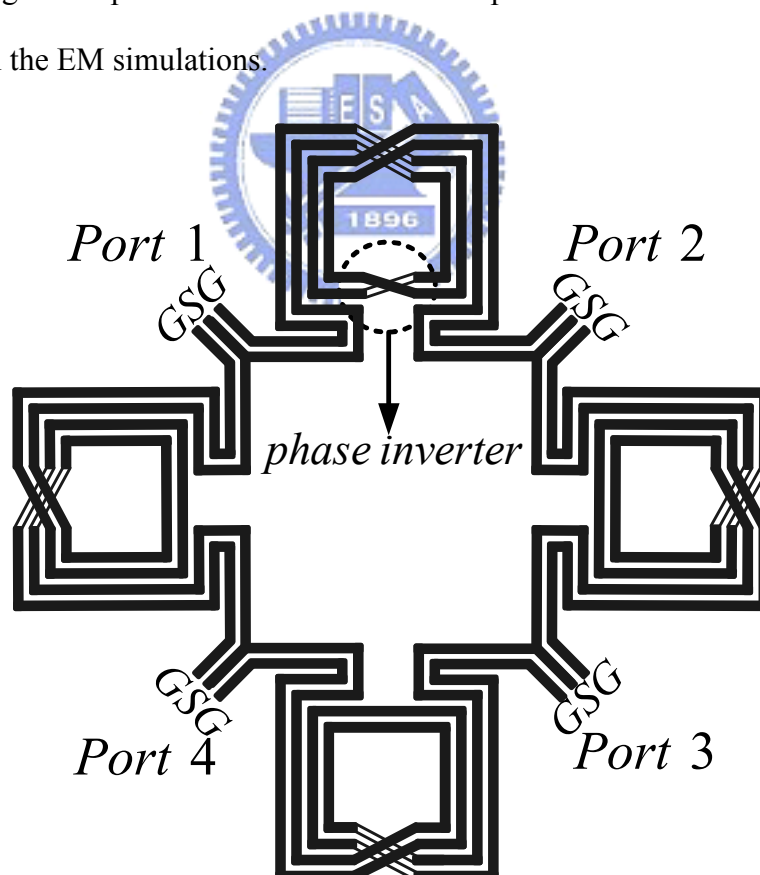
Fig. 4-4   Symmetrical spiral-shaped CPS rat-race coupler with a phase inverter.

In our complete analysis, the lossy rat-race coupler with a phase inverter has wideband operation and still keeps outputs balanced because of equal path loss. It is interesting that a distortionless line is employed to achieve a simple port-matching condition. The matching condition and bandwidth performance are different from those under the lossless condition analysis [42]. The shorter a transmission line is, the smaller the loss is. Therefore, the lossy phase-inverter rat-race coupler is suitable for high frequencies because of the compact size as well as the small loss.

The schematic of the entire mixer with an LO phase-inverter rat-race coupler is shown in Fig. 4-5. A micromixer employed in this chapter is the same as the micromixer presented in Section 2.3, and more details about the micromixer design are described in our previous publication [21].
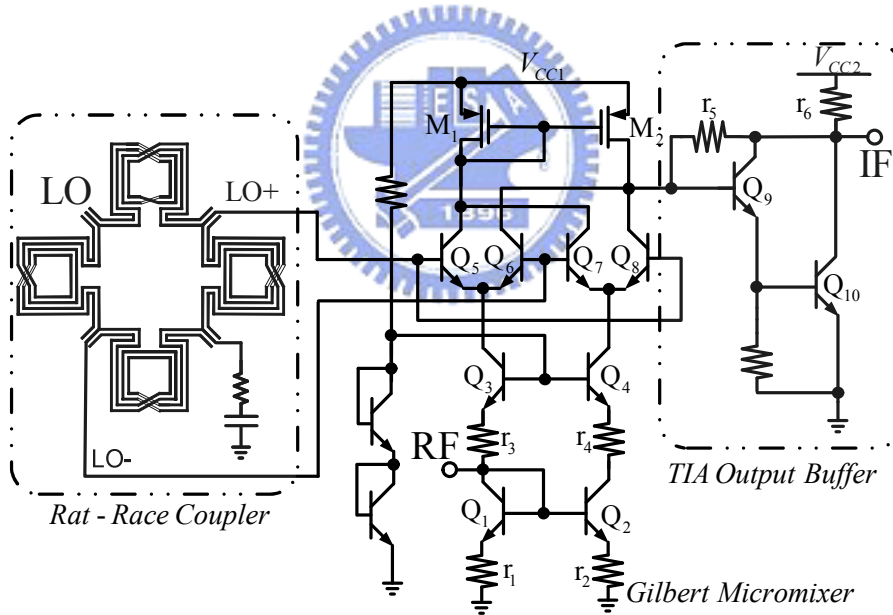
Fig. 4-5   Schematic of the micromixer with a phase-inverter rat-race coupler.

4.3 MEASUREMENT RESULTS

4.3.1 Micromixer With an Integrated Phase-Inverter Rat-Race Coupler

The micromixer with an integrated phase-inverter rat-race coupler is fabricated using 0.35-μm SiGe BiCMOS technology with three metal layers [54]. The die

photograph is displayed in Fig. 4-6 and the active circuitry is inside the rat-race coupler for a compact layout. The chip size is approximately 1.4 mm × 1.4 mm. The transistors of the mixer core are SiGe HBT devices with a peak cut-off frequency of 67 GHz, while the rat-race coupler is mainly formed by the top metal. The total current consumption is approximately 32 mA at the supply voltage of 5 V.
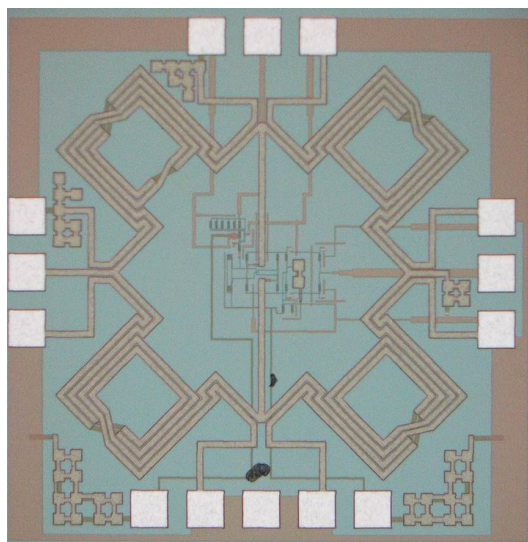
Fig. 4-6   Die photograph of the micromixer with an integrated phase-inverter rat-race coupler.

Fig. 4-7 presents the wideband performance of this micromixer. Thanks to the RF wideband matching and LO broadband phase-inverter rat-race coupler, this mixer works with a 3-dB bandwidth of 10.5 GHz from 2.5 to 13 GHz. The conversion gain is approximately 12 dB. The mixer needs only 0-dBm LO power to function after taking the dissipated loss of the coupler into consideration because the SiGe HBT transistors in the Gilbert cell switching quad only need small power to perform the current commutation. Fig. 4-7 also exhibits that the input 1-dB gain compression point IP_{1dB} and the input third-order intercept point IIP_3 are approximately -16 and -4 dBm, respectively. The power performance is measured at 2.6, 5.1, 7.6, 10.1, and 12.6 GHz.
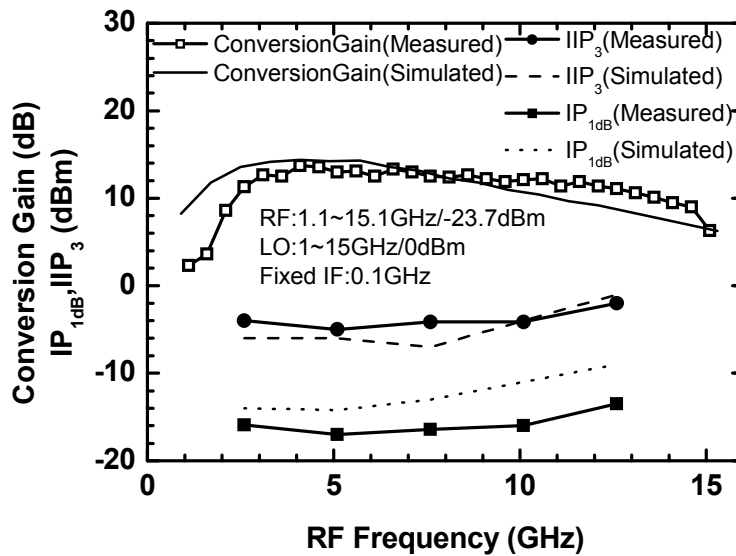
Fig. 4-7   Conversion gain, IP$_{1dB}$, and IIP$_3$ of the phase-inverter rat-race coupler micromixer.

The noise figure of the micromixer with an integrated phase-inverter rat-race coupler is measured at fixed LO frequencies of 5, 7, and 9 GHz. The minimum noise figure is approximately 14 dB, as shown in Fig. 4-8. The noise figure does not vary very much with LO frequency. As shown in Fig. 4-9, the 3-dB bandwidth is approximately 400 MHz. The simulations are performed by the post-layout extraction of active circuits, as well as by the EM simulation of the rat-race coupler. The measurements are close to the simulations.

The LO-to-IF and LO-to-RF isolations are below -30dB, while the RF-to-IF isolation is below -25 dB, as shown in Fig. 4-10. The input return loss at the RF and LO ports and the output return loss at the IF port are measured, as shown in Fig. 4-11. Because the RF-input stage is a micromixer with a wideband matching property, and the IF-output stage utilizes a Darlington pair of transistors along with a resistive feedback technique, the return loss at the RF and IF ports is below -10 dB. The perfect LO-input matching occurs at 7 GHz.
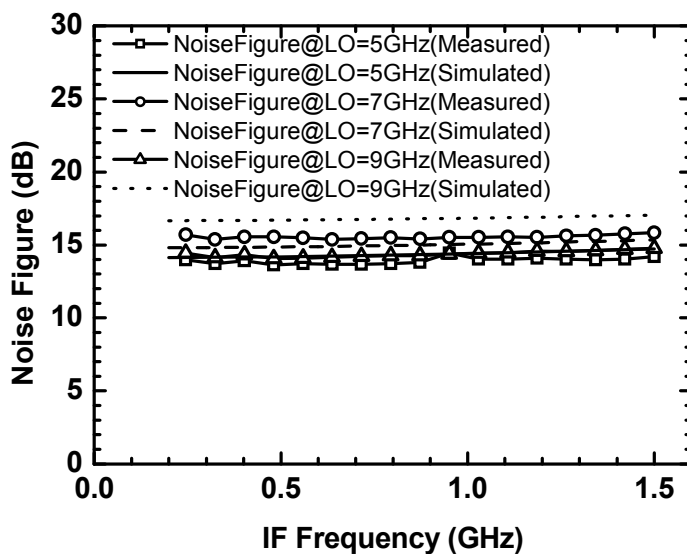
Fig. 4-8   Noise figure of the micromixer with an integrated phase-inverter rat-race coupler.
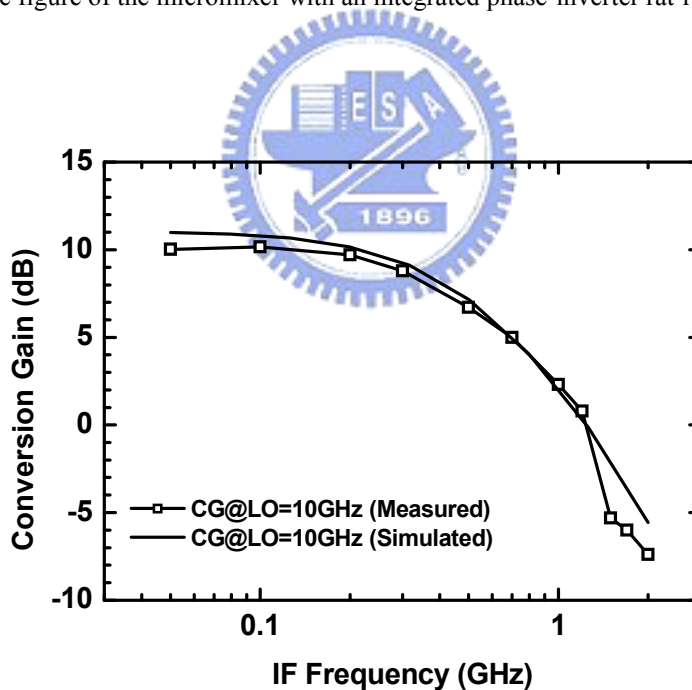
Fig. 4-9   Conversion gain of the micromixer with an integrated phase-inverter rat-race coupler with respect to IF frequencies.
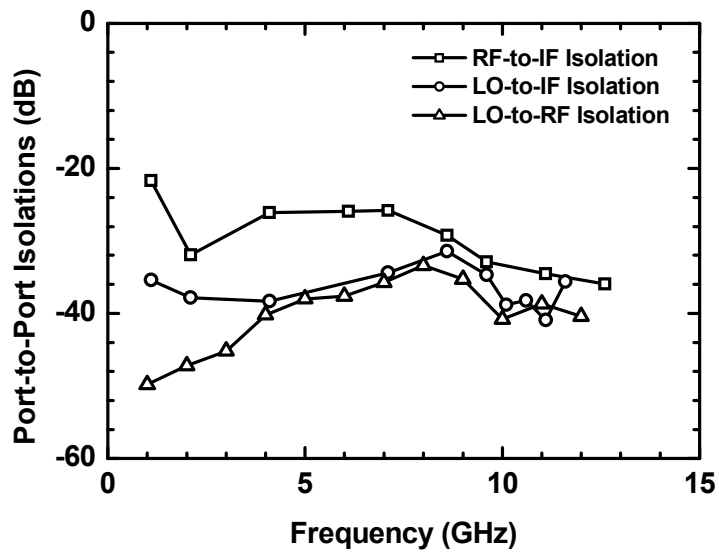
Fig. 4-10   Port-to-port isolations of the micromixer with an integrated phase-inverter rat-race coupler.
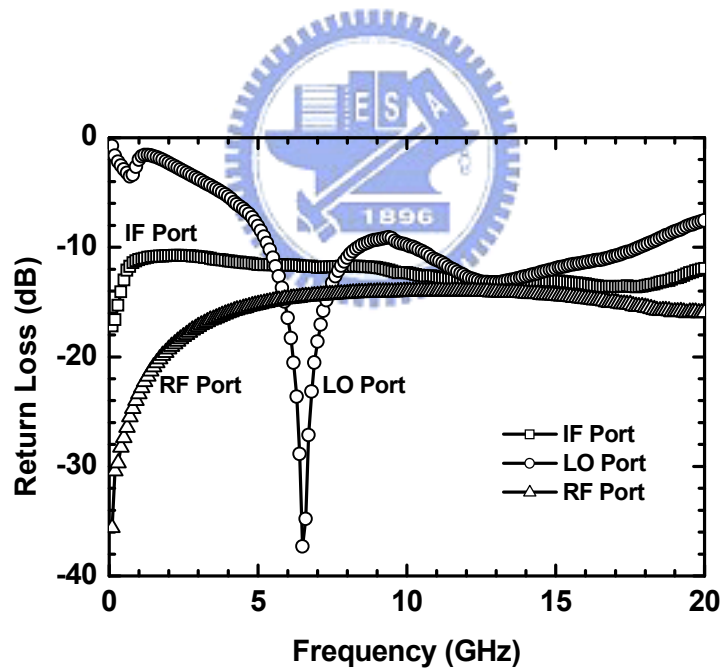
Fig. 4-11   Return loss of the micromixer with an integrated phase inverter rat-race coupler.

TABLE 4.1 Measurement Results of the Phase-Inverter Rat-Race Coupler Mixer

	TSMC 0.35-μm 3P3M SiGe BiCMOS
Item	Down-Converter
Frequency (GHz)	2.5 to 13
Conversion Gain (dB)	12
LO Power (dBm)	0
IF Bandwidth (MHz)	400
IP_{1dB} (dBm)	-16
IIP_3 (dBm)	-4
Noise Figure (dB)	14
RF Return Loss (dB)	< -14
IF Return Loss (dB)	< -10
Supply Voltage (V)	5
Total Power Dissipation (mW)	160
Chip Size (mm × mm)	1.4 × 1.4

4.3.2 Symmetrical Spiral-Shaped Phase-Inverter Rat-Race Coupler

A symmetrical spiral-shaped rat-race coupler with a phase inverter was implemented on a low-resistivity (~10 Ω·cm) silicon substrate [54]. The die photograph is shown in Fig. 4-12, and the chip estate, including pads, is 1×1 mm^2. However, the coupler size is only 0.5 mm^2, while each spiral-shaped CPS takes on an area of 250 μm × 250 μm. In addition, circuitry, like a mixer, can be arranged in the center of the rat-race coupler to save the area without performance degradation, as shown in Fig. 4-6. The rat-race coupler here is designed at the center frequency of 14.5 GHz, while the rat-race coupler employed in the mixer is designed at the center frequency of 7.7 GHz. The phase-inverter rat-race coupler is formed by the top two metals with a thickness of 0.925 and 0.64 μm. The width, spacing, and length of the quarter-wavelength CPS are 15, 5, and approximately 1800 μm, respectively. The measurement is performed by a four-port network analyzer with on-wafer probes on four sides of the die.
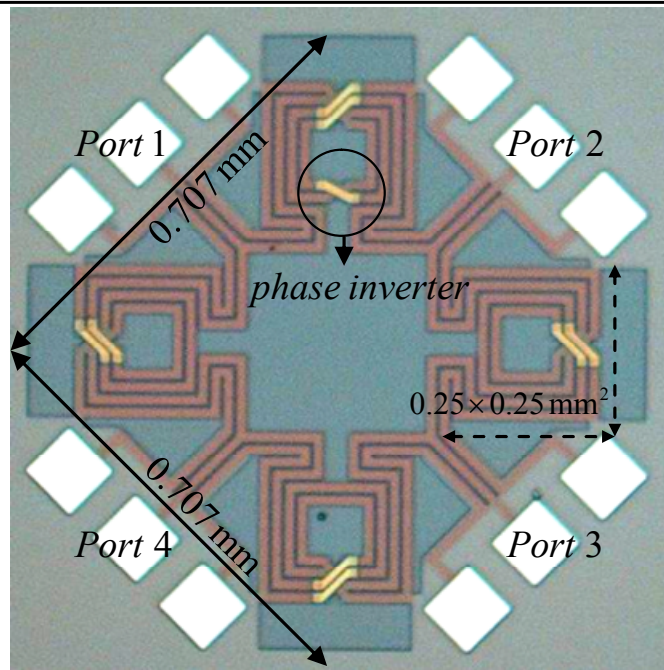
Fig. 4-12   Die photograph of the symmetrical spiral-shaped rat-race coupler with a phase inverter.

Ports 1 and 3 are the delta and sum ports, respectively. Fig. 4-13 shows the magnitude of S_{11}, S_{21}, S_{31}, and S_{41} from the measurement and the IE3D EM simulation. This phase-inverter rat-race coupler functions from 5 to 23 GHz with a 4.6-to-1 bandwidth ratio. The bends in the spiral-shaped CPSs, in the IC process, are a small proportion of the entire transmission lines. Thus, the bandwidth of the phase-inverter rat-race coupler implemented by IC technology is comparable with that implemented on the printed circuit board [42], [45]. There is perfect port-matching at 14.5 GHz, and the isolation between the delta and sum ports (S_{31}) is below -25 dB. The magnitude imbalance between S_{21} and S_{41} is small and approximately 1 dB, as shown in Fig. 4-14, resulting from the phase inverter. However, the phase difference is always close to 180°. The maximum phase and magnitude errors are 8.5° and 1.6 dB within the operation frequencies of 5~23 GHz, respectively.
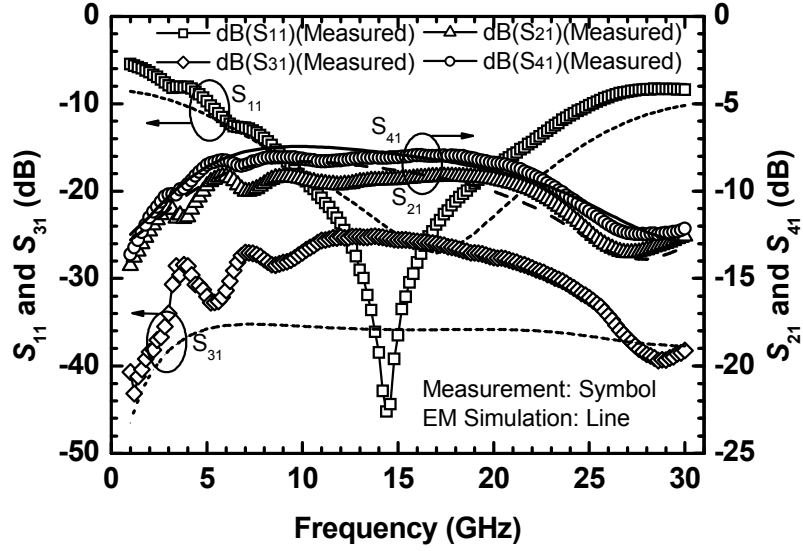
Fig. 4-13   *S*-parameters of the symmetrical spiral-shaped rat-race coupler with a phase inverter.
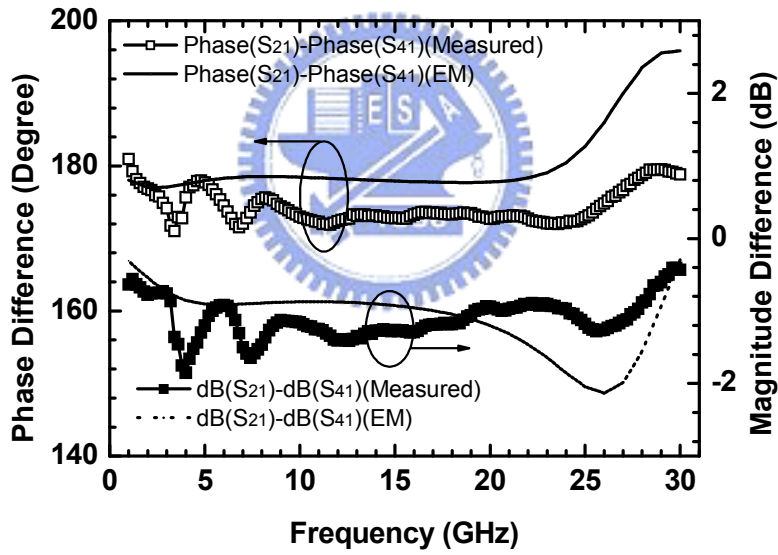
Fig. 4-14   Phase difference between S_{21} and S_{41} of the rat-race coupler with a phase inverter.

The performance of the signals, when fed from the sum port, is displayed in Fig. 4-15. The phase difference stays at around 0° and the difference in magnitude is close to 0 dB. The dissipated loss of the phase-inverter rat-race coupler is defined as

$$Loss = -10\log\left(\left|S_{11}\right|^2 + \left|S_{21}\right|^2 + \left|S_{31}\right|^2 + \left|S_{41}\right|^2\right) \qquad (4.12)$$

and is approximately 5.5 dB, as shown in Fig. 4-16.
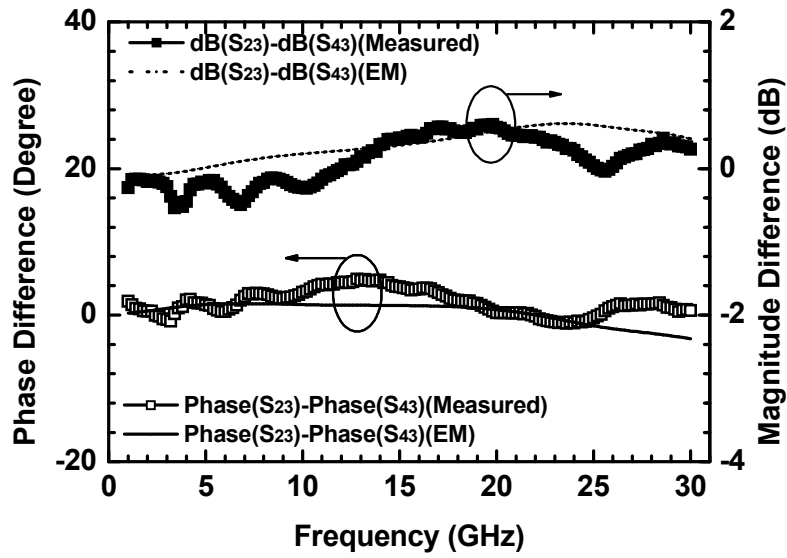
Fig. 4-15   Phase difference between S_{23} and S_{43} of the rat-race coupler with a phase inverter.
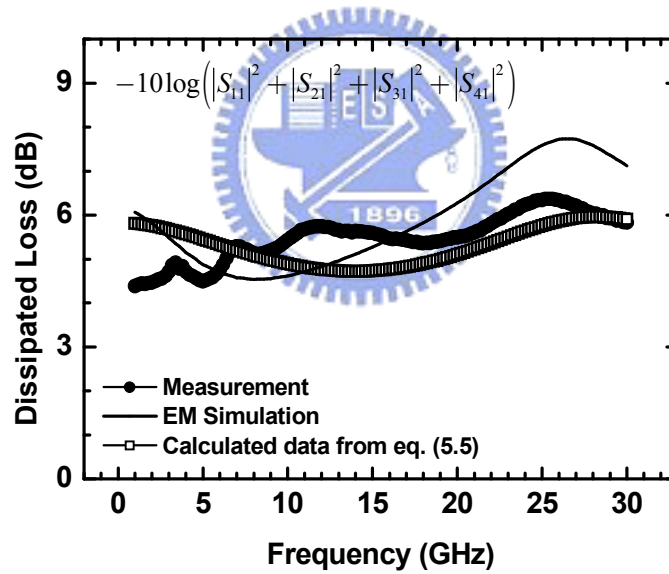
Fig. 4-16   Dissipated loss of the symmetrical spiral-shaped rat-race coupler with a phase inverter.

The measured input return loss of all ports is shown in Fig. 4-17. All port matching is achieved in this 4-port rat-race coupler while the 3-port lossless passive components in Chapter 5 and Chapter 6 do not have all port matching.
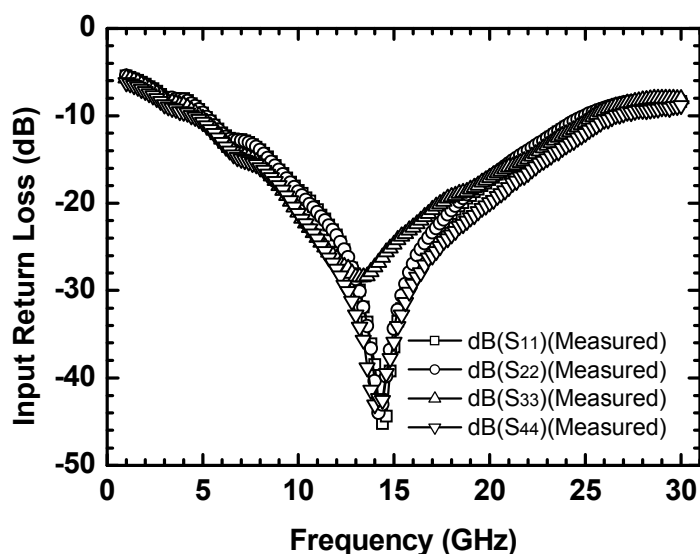
Fig. 4-17   Input return loss of the symmetrical spiral-shaped rat-race coupler with a phase inverter.

A two-port transformer has a broad frequency operation and a low loss. Generally speaking, the upper operation frequency of a two-port transformer is limited by the parasitic capacitances. However, when the transformer is employed as a three-port balun, output signal balance at high frequencies is drastically deteriorated since the single-end input signal destroys the transformer's symmetry in EM characteristics [55]. Thus, a three-port transformer balun has much less bandwidth than a two-port transformer has. An active balun is plagued by the dc-power consumption, dynamic range, and noise, in spite of its small size. Therefore, this phase-inverter rat-race coupler is a good choice for a wideband balun.

The comparison results, based on the same return-loss performance (<-10 dB), are shown in TABLE 4.2. Silicon-based phase-inverter rat-race couplers are also implemented with lossless multilayer microstrips [47] and lossy finite-ground coplanar waveguides (FGCPWs) [49]. The lossy couplers in this study and [49] have broader input matching than the lossless counterpart in [47], because of the

degradation of the quality factor of the transmission line. The signal balance in our study is better than that of [47], because of the symmetrical design in our phase inverter. When compared with [49], our signal-balance performance is as good as that of the FGCPW coupler, but the fractional bandwidth of our coupler is better because of the lower quality factor of the transmission line when operated at lower frequencies.

TABLE 4.2 Comparisons of the Silicon-Based Rat-Race Couplers With a Phase Inverter.

Ref	Operation Frequency (GHz)	Size (μm²)	Method	Through (dB)	Coupled (dB)	Return Loss (dB)	Isolation (dB)	Phase Difference (degree)
[47]	25~35 (33%)	282×314	Multilayer design with ground plane	-3.1 ~ -3.18	-5.1~ -5.7	<-10	<-17	150~200*
[49]	48~80 (50%)	334×334	FGCPW	-4.1 ~ -5	-5.7 ~ -6.5	<-10	<-18.5	182~186
	62~90**	320×320		-4.2 ~ -5	-5.6 ~ -6.5	<-10	<-21	184~186.5
This Work	5~23 (128%)	707×707	Spiral-shaped CPSs	-7.96 ~ -9.65	-9.14 ~ -10.57	<-10	<-25	171.5~178

* From the plot of measured phase difference.

**The upper frequency is limited by the measurement.

4.3.3 Distortionless Transmission Line

By the extraction from the measured four-port S-parameters with curve fitting, the values of R_0, L_0, G_0, and C_0 are

$$\begin{cases} R_0 = 161\,\Omega/cm \\ L_0 = 7.47\,nH/cm \\ G_0 = 0.03\,S/cm \\ C_0 = 1.28\,pF/cm \end{cases} \tag{4.13}$$

and they are close to the values directly extracted from the simulated two-port S-parameters of a quarter-wavelength coplanar stripline [53]. S_{11} and S_{21}, calculated by (4.5), are plotted in Fig. 4-18 in comparison with the measurement results.
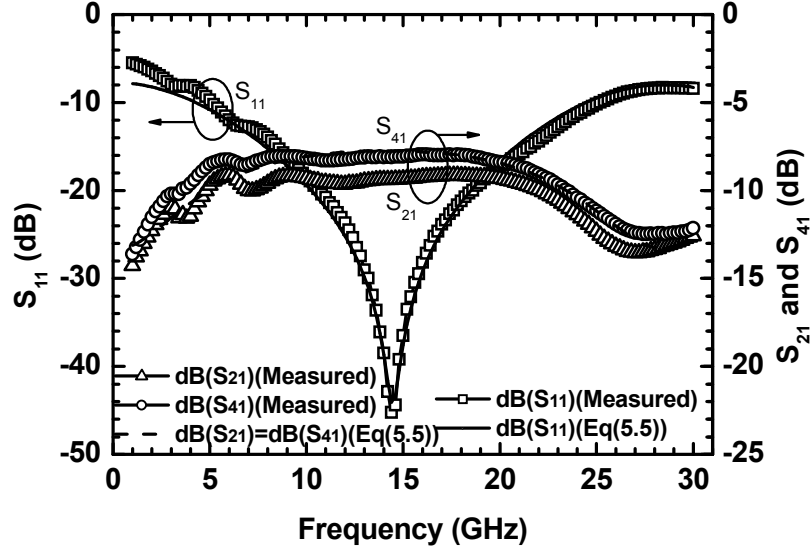
Fig. 4-18 Calculated *S*-parameters of the rat-race coupler with a phase inverter.

Notice that the ratio of R_0 to L_0 (R_0/L_0=21.6 GΩ/H) is close to the ratio of G_0 to C_0 (G_0/C_0=23.1 GS/F). Thus, the lossy transmission line is close to a distortionless transmission line [52]. Thus, the characteristic impedance is almost a real number. As mentioned in Section 4.2, perfect port matching can be achieved at the center frequency of approximately 14.5 GHz. Fig. 4-19 shows the characteristic impedance and the complex propagation constant, based on the formulas

$$Z_C = \sqrt{\frac{R_0 + j\omega L_0}{G_0 + j\omega C_0}} = \sqrt{\frac{L_0}{C_0}} \tag{4.14}$$

and

$$\gamma = \alpha + j\beta = \sqrt{(R_0 + j\omega L_0)(G_0 + j\omega C_0)} = \frac{R_0}{\sqrt{\frac{L_0}{C_0}}} + j\omega\sqrt{L_0 C_0} \tag{4.15}$$

where

$$\frac{R_0}{L_0} = \frac{G_0}{C_0} \tag{4.16}$$

for a distortionless transmission line. The characteristic impedance is approximately

76+0.6j Ω and it fits the matching equation (4.6). Moreover, the attenuation constant α is unchanged and the propagation constant β is almost a linear function of frequency. Therefore, the coupler is non-dispersive. The attenuation of the 1800-μm distortionless line is approximately 3.28 dB.
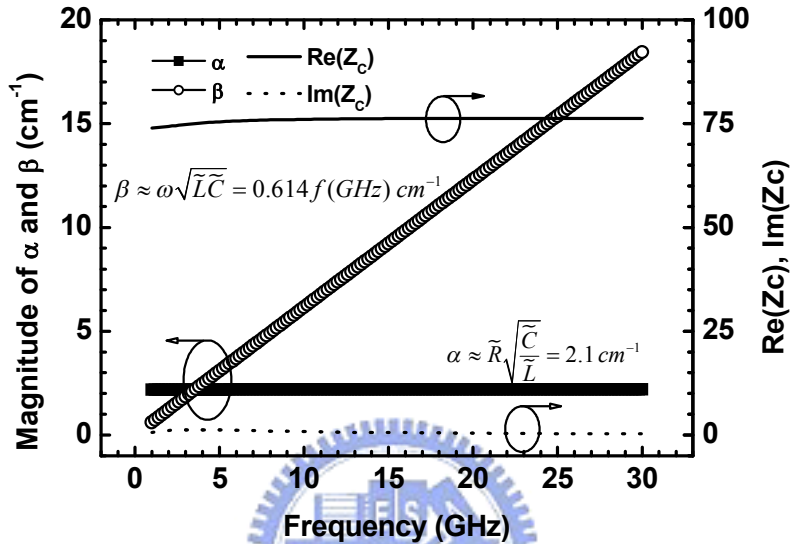
Fig. 4-19   Calculated characteristic impedance and complex propagation constant of the rat-race with a phase inverter.

4.4 SUMMARY

In this chapter, the lossy rat-race coupler implemented on the standard silicon substrate is analyzed and designed. A phase inverter is utilized in this coupler to extend the operation bandwidth and to provide balanced outputs even for the lossy silicon substrate. The transmission lines in the coupler are formed by symmetrical spiral-shaped CPSs to shrink the coupler size, and are designed as a distortionless line for the port matching of the coupler. It is easy to construct a phase inverter in the middle of the symmetrical spiral-shaped CPS. The demonstrated monolithic rat-race coupler, with the size of 0.5 mm^2, operates from 5 to 23 GHz, and keeps the output broadband balanced. In addition, a single-ended broadband Gilbert micromixer, along

with an LO phase-inverter rat-race coupler, is demonstrated. The mixer functions from 2.5 to 13 GHz and has the conversion gain of 12 dB, IP_{1dB} of -16 dBm, IIP_3 of -4 dBm, and noise figure of 14 dB.

Chapter 5 Monolithic Planar Marchand Balun Using a Standard Silicon IC Process

5.1 INTRODUCTION

For the balanced mixers, the Gilbert switch quad demands differential local oscillator (LO) signals. It is cumbersome to use an off-chip balun for the wideband balanced LO signal generation because the differential signals experience the different delay paths on the circuit board, especially at high frequencies. Hence, a single-to-differential LO balun is integrated in the IC process to form a single-ended mixer. Since it is difficult to achieve truly differential signals with equal magnitude and opposite phase by an active balun in addition to more power consumption at high frequencies, a passive balun is taken into consideration. The Marchand balun is a very wideband passive balun and is popularly used for broadband applications such as a double-balanced diode mixer [56] and a frequency doubler [57]. However, most Marchand baluns are realized on a semi-insulating or high-resistivity substrate. The proper Marchand balun topology suitable for a standard silicon IC process is identified in this chapter to maintain the truly balanced signals regardless of the substrate loss.

A single-ended wideband Gilbert down-converter is fabricated in the 0.35-μm SiGe BiCMOS technology and demonstrated in this chapter. It is composed of a micromixer, an integrated LO Marchand balun, and a TIA output amplifier. This mixer core is the same as that in Chapter 2. This mixer has 15-dB conversion gain, 13-dB noise figure, and 400-MHz IF bandwidth and works from 3.5 to 14.5 GHz.

5.2 ANALYSIS AND IMPLEMENTATION OF THE PLANAR MARCHAND

BALUN USING A SILICON IC PROCESS

5.2.1 Analysis

The Marchand balun, a very broadband passive balun, was proposed in 1944 and has one unbalanced input and two balanced outputs [58]. The compensated Marchand balun can perform impedance transformation from the balanced port to the unbalanced port. The load at the balanced port is shunted with a quarter-wavelength short stub and in series with a quarter-wavelength open stub [59], [60]. Nevertheless, this type is not easily realized in the IC process, especially in the silicon IC process, and thus is not commonly used in ICs.
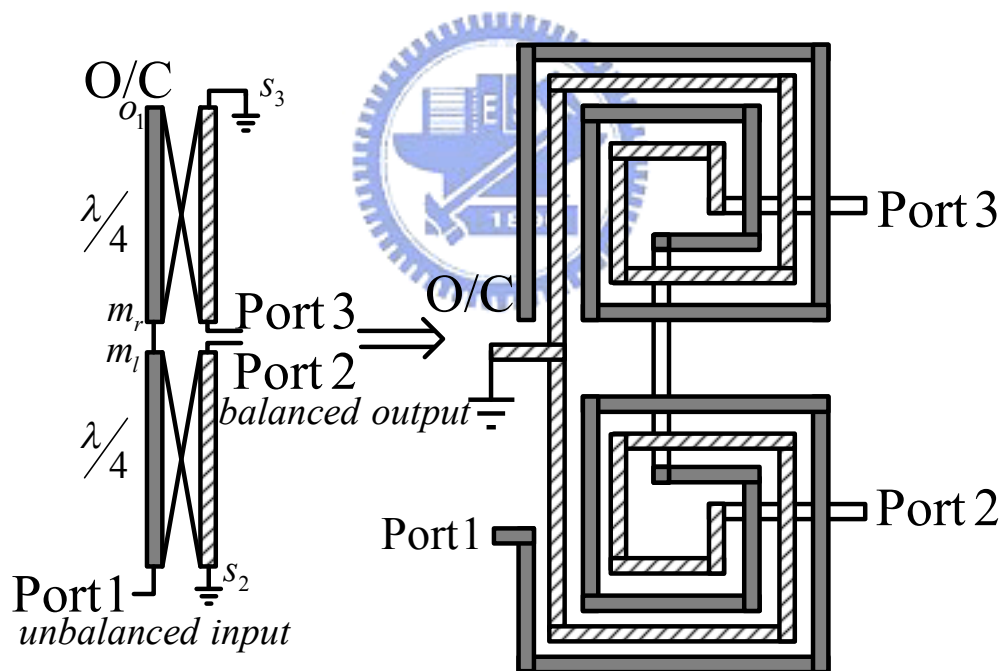
Fig. 5-1   Planar Marchand balun with λ/4 coupled lines.

The planar Marchand balun is composed of two back-to-back quarter-wavelength coupled lines, as shown in Fig. 5-1. Each coupled line has four ports—input, direct, coupled, and isolated ports. Two coupled ports of coupled lines are connected with

short ends; the direct ports are tied together. One of the input ports is connected with an open end and the other is the unbalanced input of the Marchand balun, while the balanced outputs of the Marchand balun are from the isolation ports. This configuration is the most popular one, and other topologies of the Marchand balun had been developed in [61].

The transmission and reflection properties of the Marchand balun can be analyzed easily by the properties of the coupler and open and short terminals [62]. The quarter-wavelength coupled line has the scattering parameters for the coupled and transmitted ports C and T, which are derived in Appendix C. The relation between C and T of the coupled line is written as

$$\begin{cases} |C|^2 + |T|^2 = 1, & \text{no loss} \\ |C|^2 + |T|^2 < 1, & \text{with loss}. \end{cases} \tag{5.1}$$

The short terminal results in an antiphase total reflection, whereas the open terminal causes an in-phase total reflection. When a signal inputs at Port 1, one part of the input signal, the solid line signal, shown in Fig. 5-2(a), couples to the short terminal, then reflects totally in an antiphase fashion, and finally transmits to Port 2. This causes the $C \times (-1) \times T$ voltage wave transmitting to Port 2. The other part, the dotted line signal, is analyzed more complicatedly, as shown in the following steps.

Step 1) The dotted line signal transmits to the open terminal, o_1, and reflects totally.

Step 2) Some reflected power directly transmits to the middle and then couples to Port 2; the rest power couples to the short terminal, s_3.

Step 3) A proportion of power reflected from the short terminal, s_3, couples to the open terminal, o_1, and then reflects totally. Finally, the reflected signal progresses repeatedly from Step 2).

$$S_{21} = -C \times T + \frac{T^3 \times C}{1+C^2}$$

(a) S21

$$S_{31} = T \times C - \frac{T^3 C}{1+C^2}$$

(b) S31
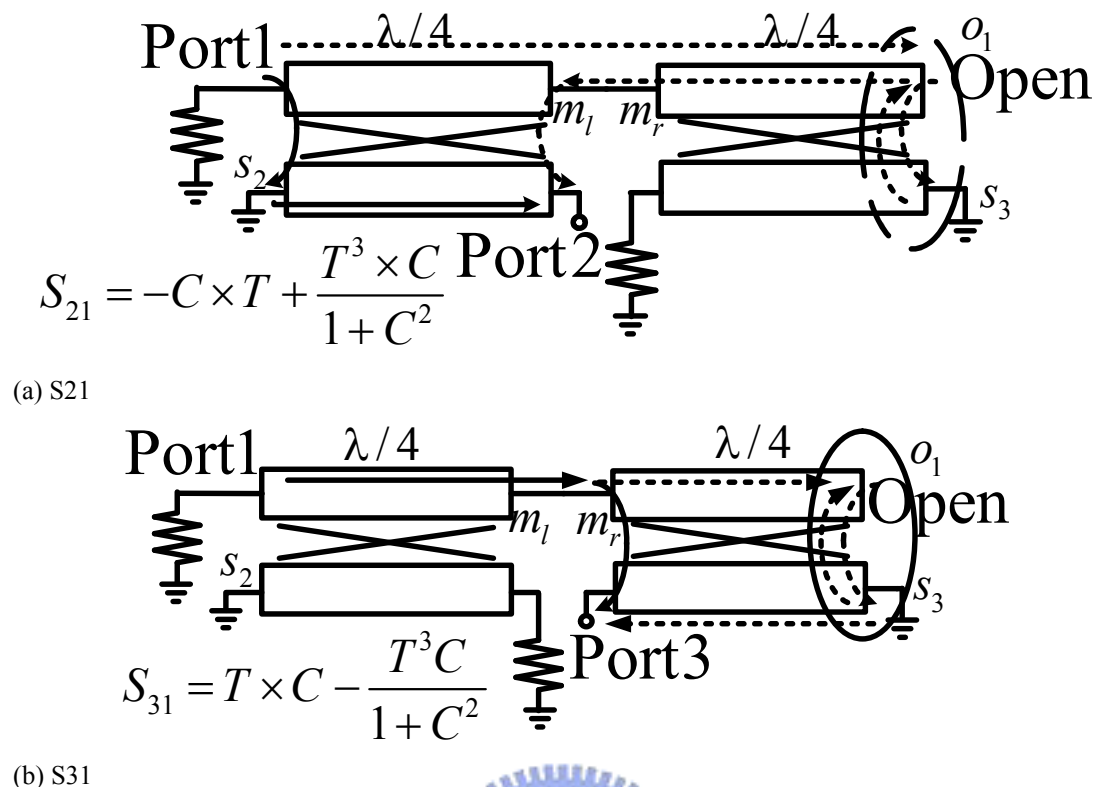
Fig. 5-2   *S*-parameter derivation of the planar Marchand balun with λ/4 coupled lines.

Consequently, the transmission coefficient form Ports 1 to 2 caused by the dotted line

signal is $T^3 \times C/(1+C^2)$. Therefore, the total transmission coefficient from Ports 1 to 2

is

$$S_{21} = -C \times T + \frac{T^3 \times C}{1+C^2}.$$ (5.2)

With the same analysis approach, the total transmission coefficient form Ports 1 to 3

is

$$S_{31} = C \times T - \frac{T^3 \times C}{1+C^2}$$ (5.3)

as shown in Fig. 5-2(b). Based on the calculations of S_{21} and S_{31}, this balun performs

single-to-differential conversion perfectly, regardless of the silicon substrate loss and

metal loss, thanks to the symmetric signal delivery, as shown in Fig. 5-2(a) and (b).

This procedure to figure out the scattering parameters can be portrayed in the tree

formation, as shown in Fig. 5-3. The tree nodes 1, 2, 3, o_1 and $s_{2\sim3}$, in Fig. 5-3,

symbolize Ports 1–3, open end, and short terminals, respectively, as shown in Fig. 5-1. As a result, the *S*-parameter matrix of the planar coupled-line Marchand balun can be expressed as

$$
[S] = \begin{bmatrix}
-C^2 + \dfrac{T^4}{1+C^2} & -CT + \dfrac{CT^3}{1+C^2} & CT - \dfrac{CT^3}{1+C^2} \\[3mm]
-CT + \dfrac{CT^3}{1+C^2} & -T^2 + \dfrac{C^2T^2}{1+C^2} & C^2 - \dfrac{C^2T^2}{1+C^2} \\[3mm]
CT - \dfrac{CT^3}{1+C^2} & C^2 - \dfrac{C^2T^2}{1+C^2} & -T^2 + \dfrac{C^2T^2}{1+C^2}
\end{bmatrix}.
\tag{5.4}
$$

$$S_{11} = -C^2 + \frac{T^4}{1+C^2}; S_{21} = -CT + \frac{CT^3}{1+C^2}; S_{31} = CT - \frac{CT^3}{1+C^2}$$

$$S_{12} = -TC + \frac{CT^3}{1+C^2}; S_{22} = -T^2 + \frac{C^2T^2}{1+C^2}; S_{32} = C^2 - \frac{C^2T^2}{1+C^2}$$

$$S_{13} = CT - \frac{CT^3}{1+C^2}; S_{23} = C^2 - \frac{C^2T^2}{1+C^2}; S_{33} = -T^2 + \frac{C^2T^2}{1+C^2}$$
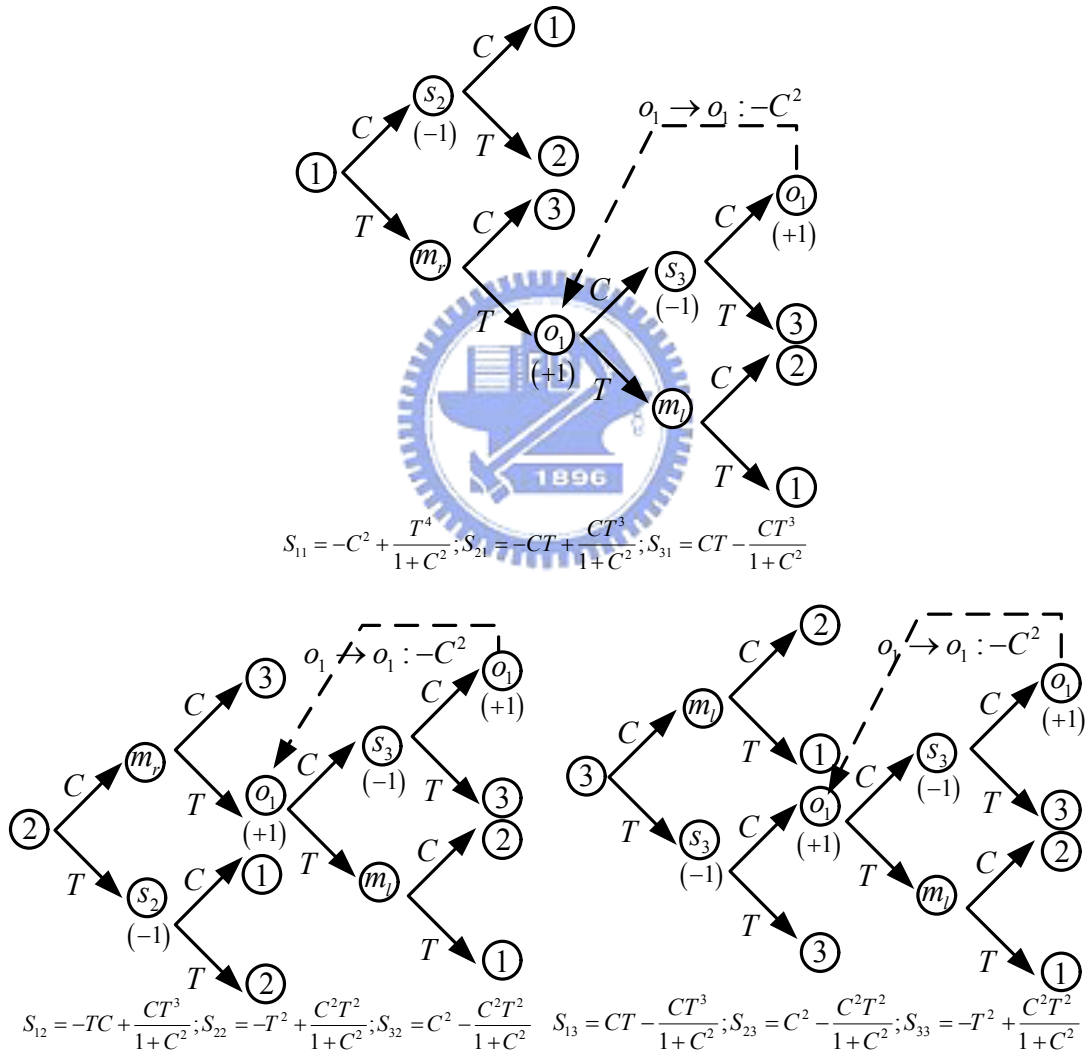
Fig. 5-3   *S*-parameter derivation of the planar Marchand balun. The nodes (1–3) of the tree stand for Port 1–3. The others nodes are denoted in Fig. 5-1.

Fig. 5-4 displays the magnitude of the transmission and reflection at the input

port of two configurations with respect to different coupling factors k, as defined in the Appendix C with the assumption of no loss. The coupling factor is designed as the value of $1/\sqrt{3}$ or 4.8 dB, for a good input matching, i.e., $S_{11}=0$, and the maximum transmission [63]. The optimal Marchand balun is practically implemented on account of the low optimal coupling factor.
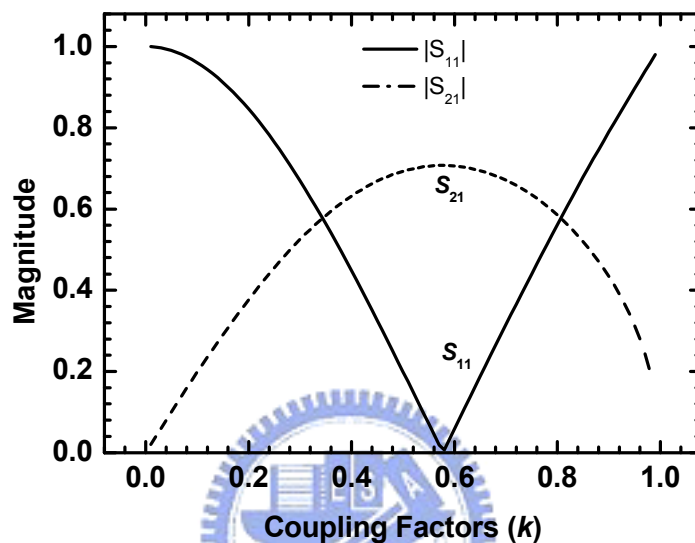
Fig. 5-4   Magnitude of the transmission and reflection at the input port of the planar Marchand balun with respect to coupling factor k for the cases of no loss.

5.2.2 Implementation

The coupled-line Marchand balun can be realized by Lange couplers [64], [65], broadside coupled lines [61], [66], [67], and spiral transmission lines [61], [66], [68]–[70]. In order to shrink the size of the balun, an interleave transformer is employed as a quarter-wavelength coupled line in our study, as shown in Fig. 5-1. The transformer-type coupled lines, namely, spiral transmission lines, can achieve the desired coupling factor. The coupled line Marchand balun with two short terminals and one open end is applied and the two ac ground terminals tied together can provide a dc bias for the mixer's switch quad.

For the balanced mixers, the LO switch quad is driven by the differential signals. A wideband single-to-differential Marchand balun is demanded in order to offer differential LO signals and to reserve the mixer wideband operation. Given that the input impedance Z_1 of the Gilbert cell is not matched to the source impedance Z_0, the *S*-parameters of Marchand balun are modified as

$$
[S] = \begin{bmatrix} \dfrac{1-k^2\left(\dfrac{2Z_1}{Z_0}+1\right)}{1+k^2\left(\dfrac{2Z_1}{Z_0}-1\right)} & j\dfrac{2k\sqrt{1-k^2}\sqrt{\dfrac{Z_1}{Z_0}}}{1+k^2\left(\dfrac{2Z_1}{Z_0}-1\right)} & -j\dfrac{2k\sqrt{1-k^2}\sqrt{\dfrac{Z_1}{Z_0}}}{1+k^2\left(\dfrac{2Z_1}{Z_0}-1\right)} \\[3em] j\dfrac{2k\sqrt{1-k^2}\sqrt{\dfrac{Z_1}{Z_0}}}{1+k^2\left(\dfrac{2Z_1}{Z_0}-1\right)} & \dfrac{1-k^2}{1+k^2\left(\dfrac{2Z_1}{Z_0}-1\right)} & j\dfrac{2k^2\sqrt{\dfrac{Z_1}{Z_0}}}{1+k^2\left(\dfrac{2Z_1}{Z_0}-1\right)} \\[3em] -j\dfrac{2k\sqrt{1-k^2}\sqrt{\dfrac{Z_1}{Z_0}}}{1+k^2\left(\dfrac{2Z_1}{Z_0}-1\right)} & j\dfrac{2k^2\sqrt{\dfrac{Z_1}{Z_0}}}{1+k^2\left(\dfrac{2Z_1}{Z_0}-1\right)} & \dfrac{1-k^2}{1+k^2\left(\dfrac{2Z_1}{Z_0}-1\right)} \end{bmatrix}. \tag{5.5}
$$

[63]. However, the balance of the two outputs is independent of the coupling factor k and the load impedance Z_1. Even if the load impedance of the Marchand balun is not matched, the outputs also have equal magnitude and opposite phase.

Most monolithic Marchand baluns are fabricated on the semi-insulating GaAs substrate. A Marchand balun on the high-resistivity (>4000 Ω·cm) silicon substrate had also been demonstrated [71]. Recently, the Marchand balun was practiced using standard silicon processing with a shielding ground plane [50]. However, the shielding ground plane limits the even-mode characteristic impedance and then reduces the balun bandwidth [70]. The operating bandwidth of the Marchand balun increases monotonically when the ratio of the even-mode characteristic impedance to the odd-mode characteristic impedance of the coupled line increases. A high even-mode characteristic impedance is preferred for a wideband Marchand balun.

Thus, the high even-mode characteristic impedance of coupled lines can be achieved in our Marchand balun topology to obtain wide bandwidth. Besides, the higher effective dielectric constant for the balun without the shielding ground plane is good for size reduction.

5.2.3 Lumped-Element Marchand Balun

The lumped-element technique, adding capacitors at three ports and one open end as shown in Fig. 5-5, is utilized for size reduction at the cost of the bandwidth [72], [73]. Thanks to the lumped-element technique, the length of coupled lines is shortened so that the loss of the balun resulting from the substrate loss and the metal loss is alleviated. Transformer-typed coupled lines are employed to shrink the size of the Marchand balun further as shown in Fig. 5-5. The balun implementation directly on the lossy silicon substrate without the ground plane is good for size compactness and wideband operation because of the higher effective dielectric constant as well as the higher ratio of even-mode to odd-mode characteristic impedance. In addition, the balun implementation only needs two interconnect metal layers.
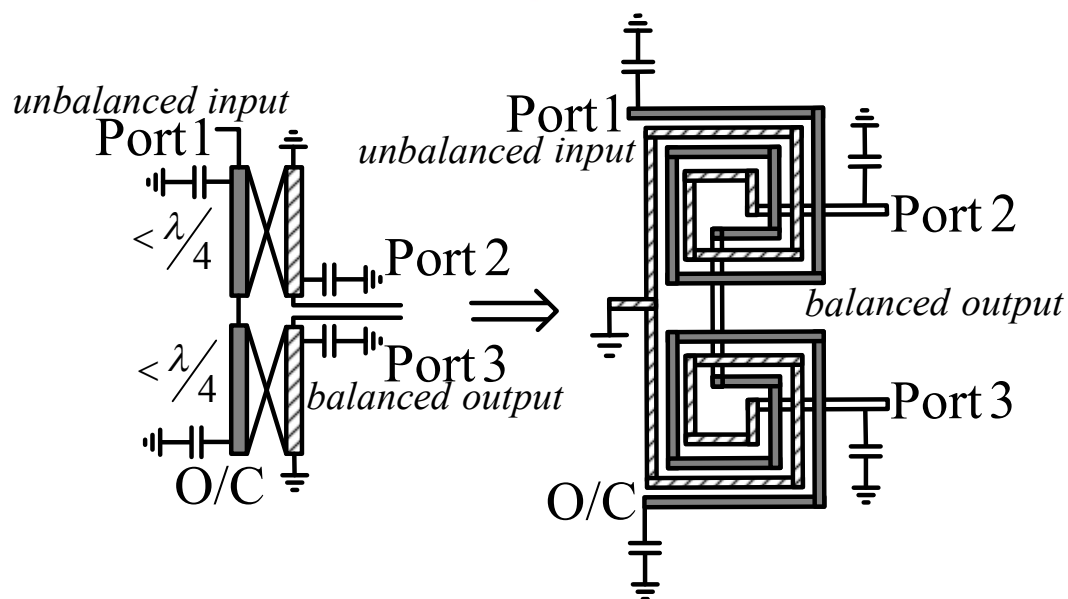
Fig. 5-5   Schematic of the lumped-element Marchand balun

5.3 MEASUREMENT RESULTS

5.3.1 Planar Marchand Balun

The planar Marchand balun, as shown in Fig. 5-6, is implemented directly on the low-resistivity (~10 Ω·cm) silicon substrate with the high even-mode characteristic impedance to hold broadband operation. This Marchand balun is formed by two-section transformer-type coupled lines and is designed at the center frequency of 12 GHz. The size of Marchand balun is approximately 660 μm × 250 μm. It is very compact thanks to the size advantage of the transformer-type coupled lines. The coupled lines are made of the top metal with the thickness of 0.93 μm, the spacing of 5 μm, and the width of 5 μm. The interleave transformer has approximately 3 : 3 turns. The substrate thickness and the top-metal-to-substrate distance are approximately 350 μm and 6.2 μm, respectively, and the length is approximately 2.2 mm. From simulation, the coupling factor of the coupled line is approximately 0.5 at 12 GHz.
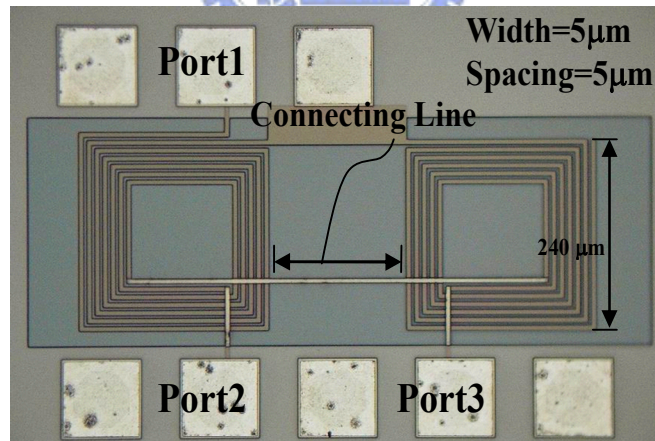
Fig. 5-6   Die photograph of a monolithic Marchand balun. The connecting line is approximately 180 μm and is restricted by the GSGSG probe.

The experimental measured data, IE3D simulation results, and the calculated data from (5.4) based on IE3D simulated C and T of the Marchand balun in Fig. 5-6 are displayed in Fig. 5-7 and Fig. 5-8. The delta plots of the phase and amplitude errors

are presented in Fig. 5-9. The magnitude imbalance in output ports is approximately 2 dB. This magnitude imbalance results from the loss of the connecting line between two transformer-type coupled lines, as shown in Fig. 5-6. The length of the connecting line is approximately 180 μm. The inevitable finite connecting line in the Marchand balun test pattern is constrained by the ground–signal–ground–signal–ground (GSGSG) pad employed for the measurement purpose. The finite connecting line can be minimized in the final fabricated circuit. On the low-resistivity silicon substrate, the signal transmission of the balun is dominated by the first component, i.e., the direct coupled term $C \times T$ of (5.2) and (5.3). However, the voltage wave directly coupled to Port 3 experiences the connecting-line loss. Thus, the transmission magnitude $|S_{31}|$ is lower than $|S_{21}|$. This phenomenon corresponds to the measured results. The outputs are more balanced in magnitude when the connecting line is removed in the IE3D simulation, as shown in Fig. 5-7, but the phase balance is almost unaffected by the connecting line. In other words, the connecting line has high associated loss than phase delay.
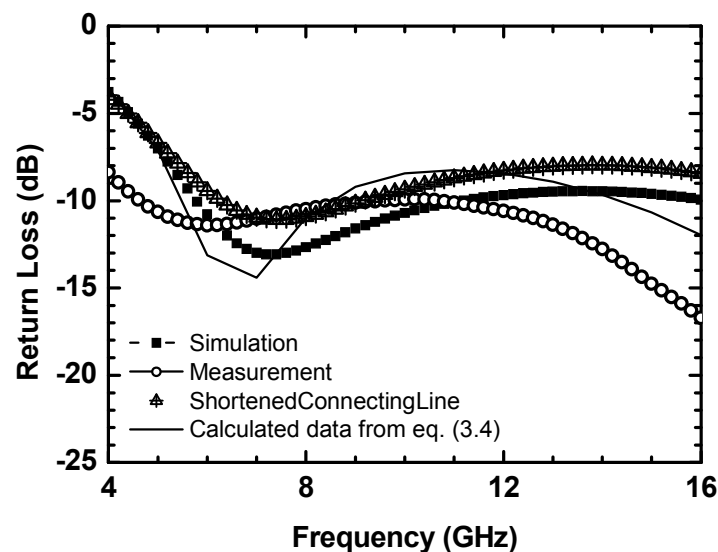
Fig. 5-7   Input return loss of the planar Marchand balun.
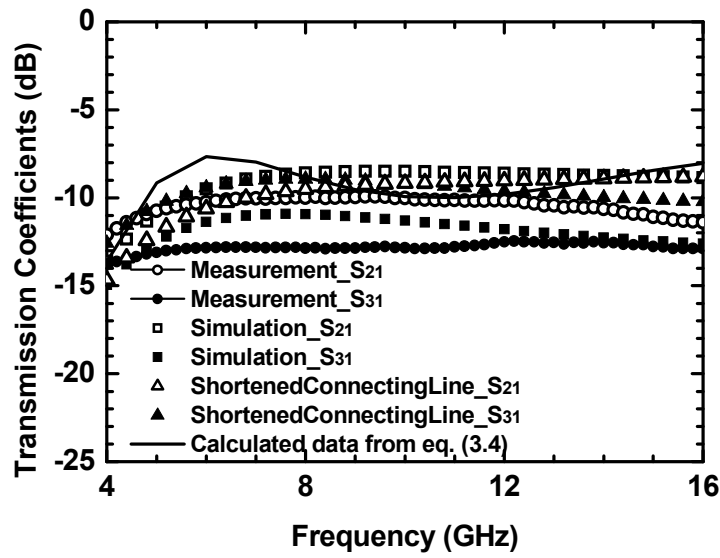
Fig. 5-8   Transmission coefficients of the planar Marchand balun.
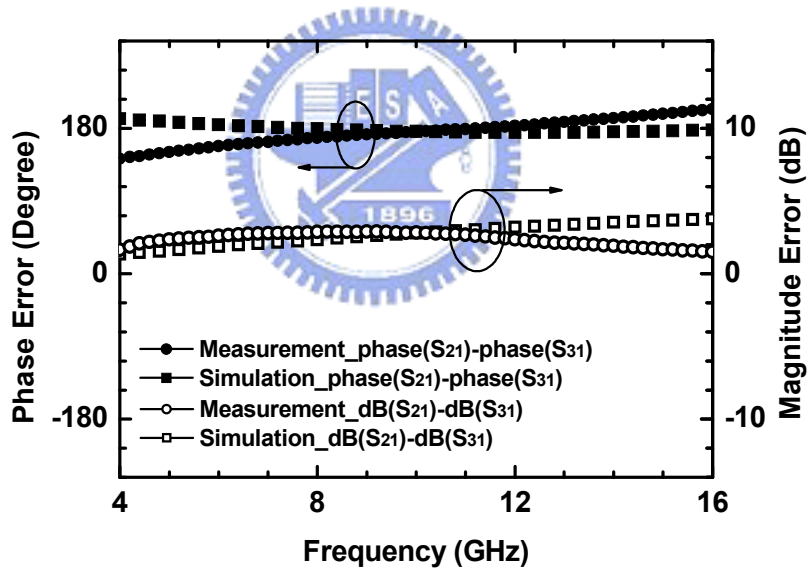
Fig. 5-9   Phase and magnitude errors of the planar Marchand balun.

The dissipated loss of a Marchand balun is defined as

$$Loss = -10\log\left(\left|S_{11}\right|^2 + \left|S_{21}\right|^2 + \left|S_{31}\right|^2\right). \tag{5.6}$$

and is approximately 6 dB, as shown in Fig. 5-10. In our study, the Gilbert mixer with

the integrated Marchand balun has a short connecting line to provide balanced outputs.

The usable bandwidth is more than 10 GHz.
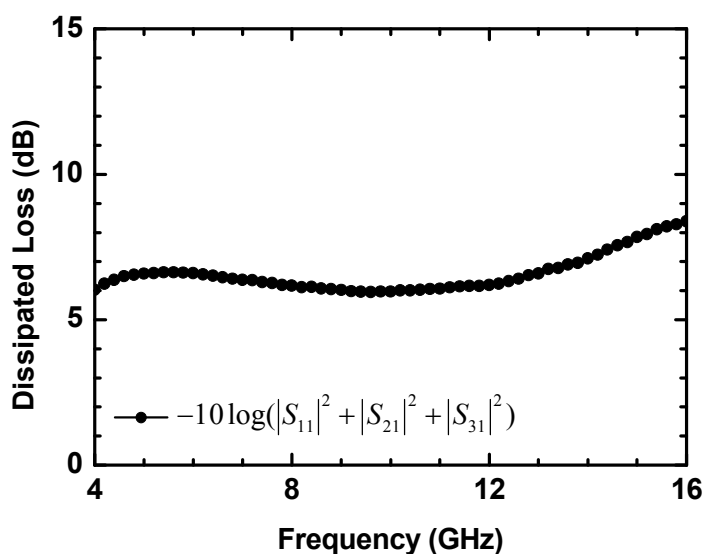
Fig. 5-10   Dissipated loss of the Marchand balun.

The mixer conversion gain is insensitive to the LO power provided that the phase is balanced and the LO power is large enough to commutate the RF current. The reason will be explained by the measured results in Section 5.3.2. The magnitude imbalance resulting from the small connecting line loss is, hence, not a matter of the mixer's operation. This balun is appropriately utilized as a single-to-differential balun at the LO port in this mixer even though the magnitude imbalance occurs.

5.3.2 Micromixer With an Integrated Marchand Balun

The Gilbert mixer along with a compensated Marchand balun was demonstrated on a semi-insulating GaAs substrate by Hamed et al. [74]. In this work, the coupled-line planar Marchand balun is implemented on a low-resistivity standard silicon substrate and, to the best of our knowledge, combined with a micromixer for the first time using 0.35-μm SiGe BiCMOS technology [21]. The active circuitry is

identical to that in Section 2.3, except the LO Marchand balun. Fig. 5-11 illustrates

the schematic and die photograph of the implemented mixer. These three components

(the micromixer, TIA amplifier, and Marchand balun) construct a single-ended

wideband down-converter. Due to the single-ended and wideband matching properties,

this Marchand micromixer with the integrated Marchand balun has a wide range of

usage. The chip size of the micromixer with an integrated Marchand balun is

approximately 1 mm × 1 mm. This integrated Marchand balun is redesigned by taking

away the connecting line described in Fig. 5-6 in order to obtain more balanced

outputs. The Marchand balun only occupies the area of 300 μm × 700 μm and is

designed at the center frequency of 9 GHz. The metal width, metal length, and

line-to-line spacing of the balun are 8 μm, approximately 2.6 mm and 2 μm,

respectively. The Marchand mixer also performs wideband mixing as the same as the

mixer in Section 2.3.

(a) Schematic   (b) Die photograph
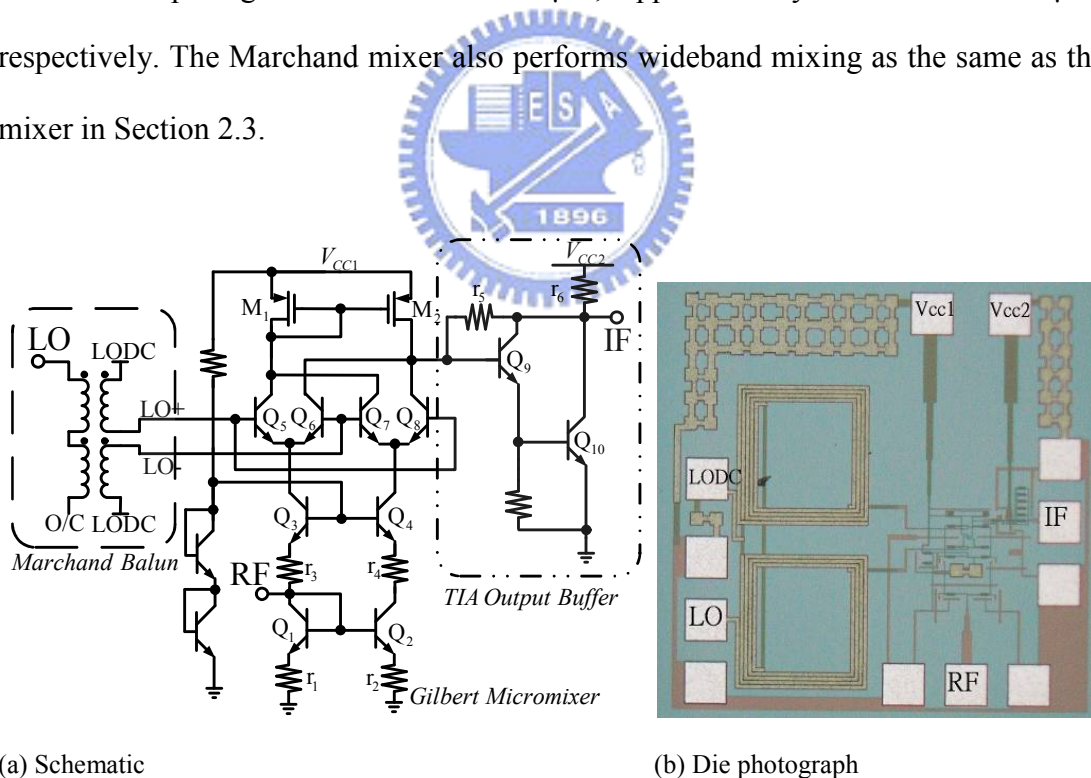
Fig. 5-11   (a) Schematic and (b) die photograph of the micromixer with an LO Marchand balun and a
TIA output buffer. The Marchand balun is designed at the center frequency of 9 GHz.

To form a single-ended mixer, a Marchand balun is utilized at the LO port. This

Marchand balun has a more than 10-GHz bandwidth and is compatible with the wideband property of the micromixer. The measured return loss at the RF, LO, and IF ports is represented in Fig. 5-12. The return-loss performance of the RF input and IF output keeps the same as that of the previous active mixer, while the return loss of the LO input is improved by the Marchand balun. The return loss of the RF, LO, and IF ports is below -14, -6, and -10 dB, respectively. The conversion gain of the micromixer with the LO Marchand balun is measured with a fixed 100-MHz IF when the LO power equals to 6 dB. Fig. 5-13 displays the experimental result. This mixer with the integrated Marchand balun can operate from 3.5 to 14.5 GHz with 11-GHz 3-dB bandwidth. The conversion gain in the 3-dB bandwidth is approximately 15 dB and is the same as that of the mixer without the Marchand balun in Section 2.3.
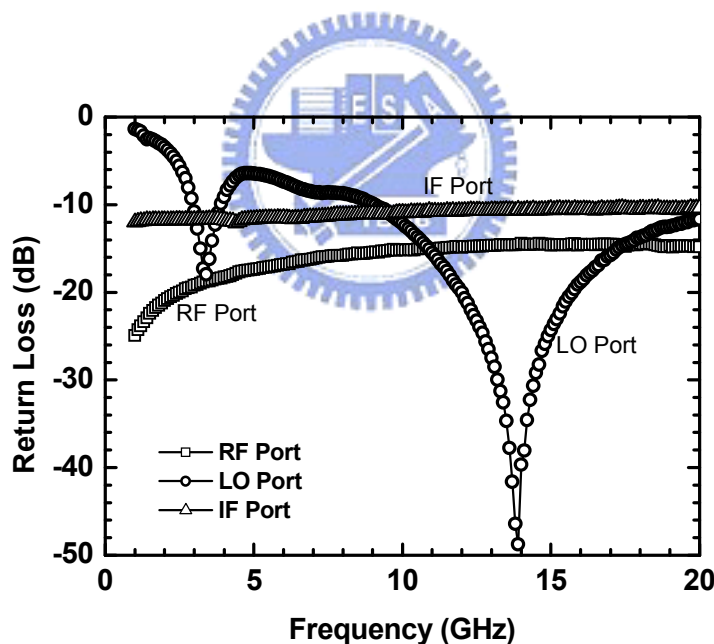
Fig. 5-12   Return loss of the micromixer with an integrated planar Marchand balun.

The low-resistivity substrate of standard silicon IC process introduces the connecting line loss. Even if this loss causes the output magnitude imbalance of the Marchand balun, the magnitude imbalance can be tolerable when a Marchand balun is

employed at the LO part of mixer as a single-to-different balun because LO power does not affect the conversion gain at the flat region, as shown in Fig. 2-7. The switch quad SiGe HBT transistors especially only demand small power to steer the RF current totally from one side to the other side of the differential pair. In other words, there is a wide range of the constant conversion gain region in terms of the LO power. Thus, the wideband Marchand balun is properly used to preserve the wideband mixing even if there is magnitude imbalance. The 3.5-GHz lower bound and 14.5-GHz upper bound of the mixer's frequency response are restricted by the Marchand balun and RF input stage, respectively, according to the measured results of the individual components (the Marchand balun and Gilbert mixer without balun) and the experimental outcome in Fig. 5-13.
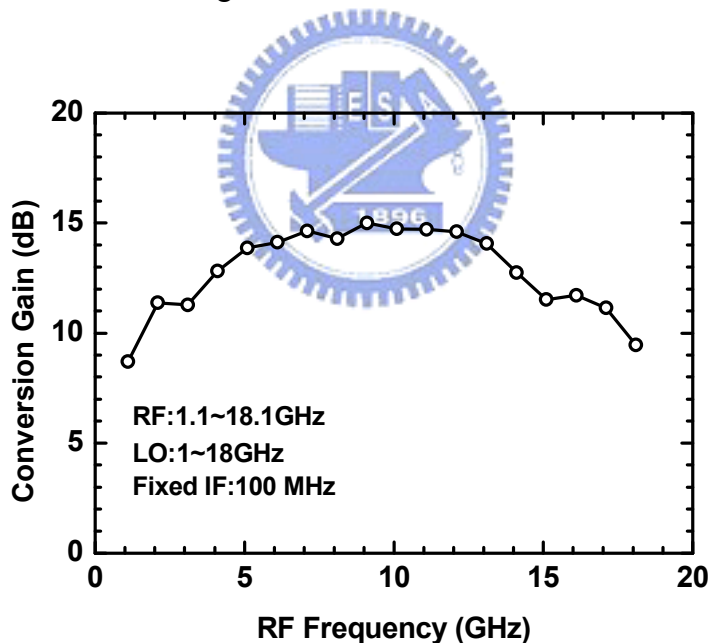
Fig. 5-13   Conversion gain of the micromixer with an integrated planar Marchand balun.

The port-to-port isolations of the Marchand mixer are presented in Fig. 5-14. During the operating frequencies of the Marchand balun, the mixer has the higher LO-to-IF isolation of approximately 35 dB. In addition, the reverse isolation of the

transistors at the input stage provides the higher LO-to-RF isolation, especially at low frequencies. The RF-to-IF isolation is below -20 dB.
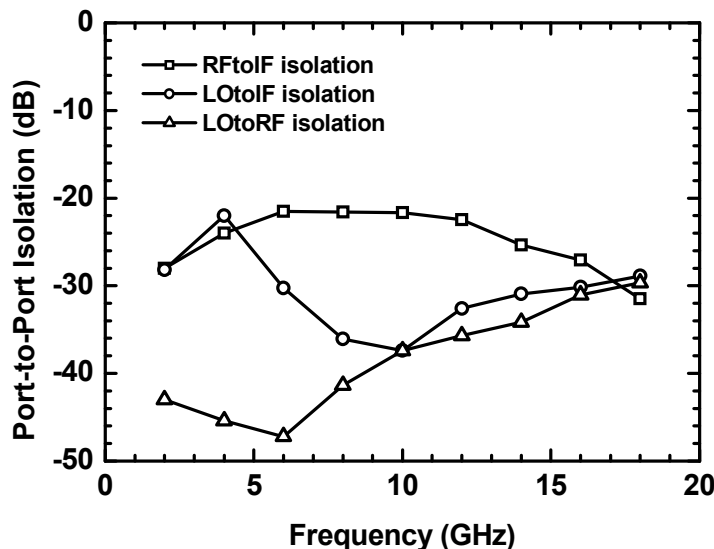
Fig. 5-14   Port-to-port isolations of the micromixer with an integrated planar Marchand balun.

The input 1-dB gain compression point IP_{1dB} and the input third-order intercept point IIP_3 of the micromixer with the integrated Marchand balun as a function of frequency are measured, as shown in Fig. 5-15. IP_{1dB} is approximately -19 dBm, while IIP_3 is approximately -7 dBm. The input signal with the frequency below 7 GHz has harmonics located in the operating frequency range. Hence, the in-band harmonic is measured when the input frequency is 5 GHz and is approximately 12 dBm.

The noise figure of the Marchand mixer is measured at each frequency of 2, 6, 10, and 14 GHz, as shown in Fig. 5-16. When the mixer operates at 6 and 10 GHz, the conversion gain is higher and the noise figure is lower simultaneously. The lowest noise figure is approximately 13 dB. The mixer works with a 5-V supply and has a core power consumption of approximately 60 mW. The additional Marchand balun does not consume any dc power. This wideband Marchand micromixer not only

maintains the performances of the original micromixer without an integrated balun in

Section 2.3, but also provides a single-ended input and output solution.
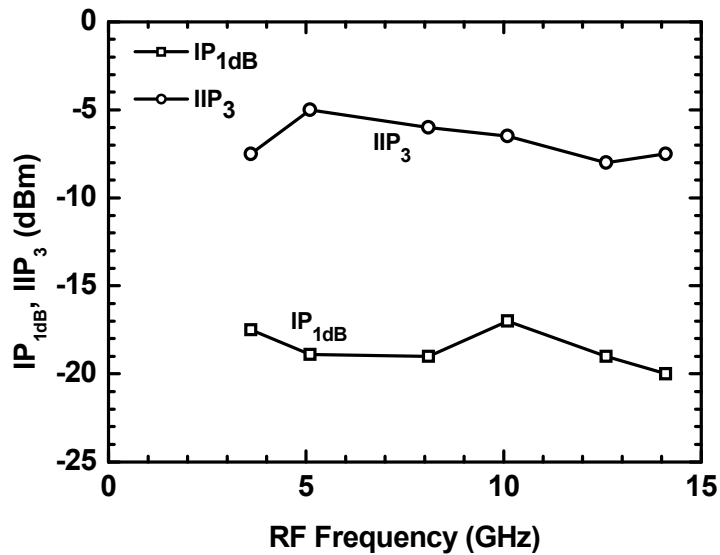
Fig. 5-15 IP_{1dB} and IIP_3 of the micromixer with an integrated planar Marchand balun.
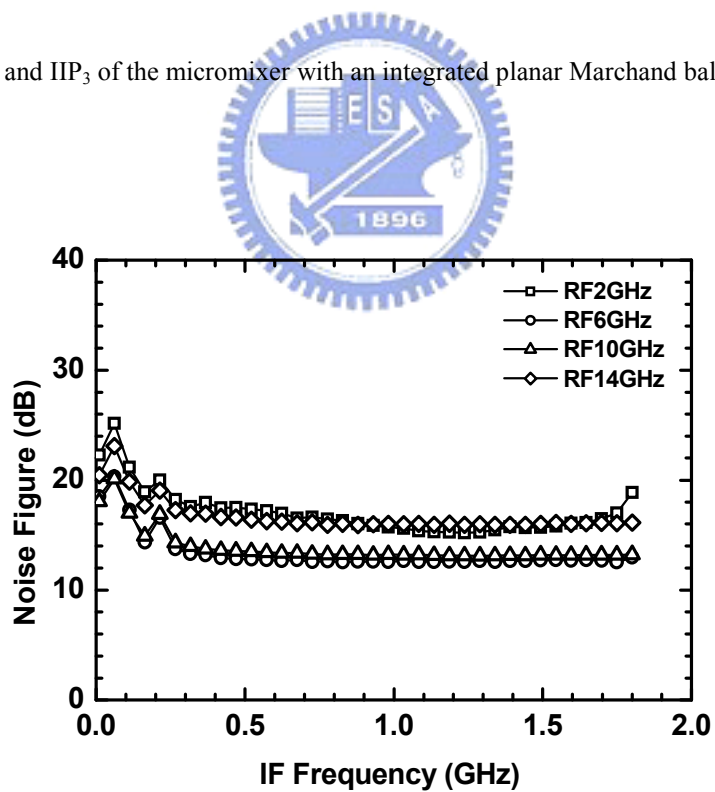
Fig. 5-16   Noise figure of the micromixer with an integrated planar Marchand balun.

5.3.3 Micromixer With a Miniaturized Marchand Balun for UWB Applications

The constituent miniaturized Marchand balun is fabricated using the standard silicon IC process as shown in Fig. 5-17. The compact size of the implemented balun is 0.25×0.5 mm^2. The substrate resistivity is approximately 10 Ω·cm and the substrate thickness is 300 μm. This balun is formed mainly by the top interconnect metal with the thickness of 3.05 μm and the height to the substrate of 4.54 μm. The spacing, width and length of the coupled line are 3 μm, 6 μm, and 1300 μm, respectively.
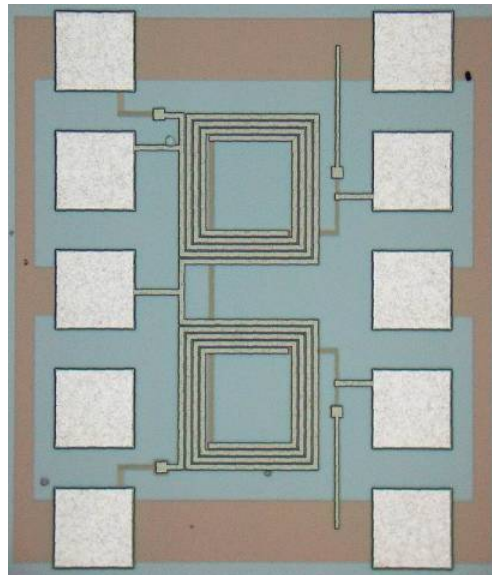
Fig. 5-17   Die photograph of the lumped-element Marchand balun

The measurement results are displayed in Fig. 5-18. The operation frequencies are from 2.5 GHz to 12 GHz. At the center frequency of 7.2 GHz, S_{11}, S_{21}, and S_{31} are -11.6 dB, -6.8 dB, -6.9 dB, respectively. The magnitude imbalance of outputs is below 1 dB up to 12 GHz. By the EM simulation, the Marchand balun without capacitors functions from 8 GHz to 30 GHz. The length reduction of coupled lines is more than 60% because of the lumped-element technique. Fig. 5-19 illustrates that the phase difference of the outputs is approximately 184° and that the dissipated loss is less than

4 dB. Thanks to the balanced structure of the Marchand balun and the shorter coupled-line length, the outputs keep balanced and the dissipated loss is small enough.
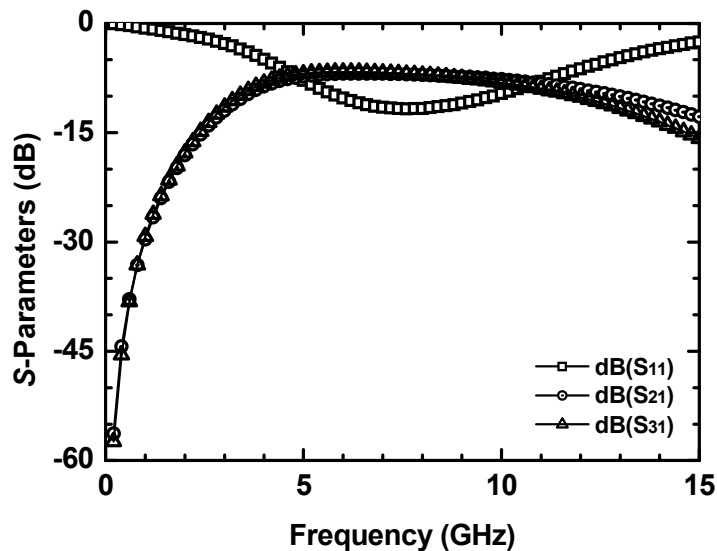
Fig. 5-18   Scattering parameters of the lumped-element Marchand balun.
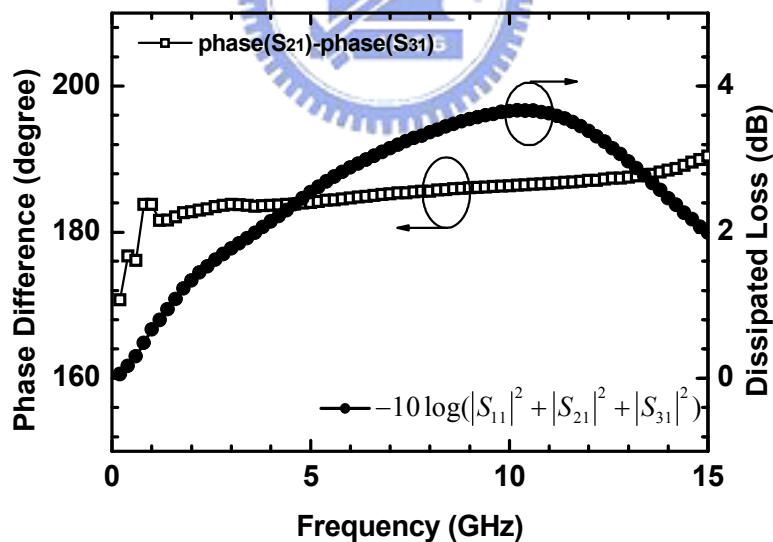
Fig. 5-19   Output phase difference and dissipated loss of the lumped-element Marchand balun.

This section also demonstrates a wideband Gilbert mixer with an integrated lumped-element Marchand balun using the 0.35-μm SiGe BiCMOS technology, as

shown in Fig. 5-20. The die photograph of the mixer is displayed in Fig. 5-21, and its chip size is 1 mm × 0.9 mm. The total current consumption is 13.9 mA at 5 V supply voltage.
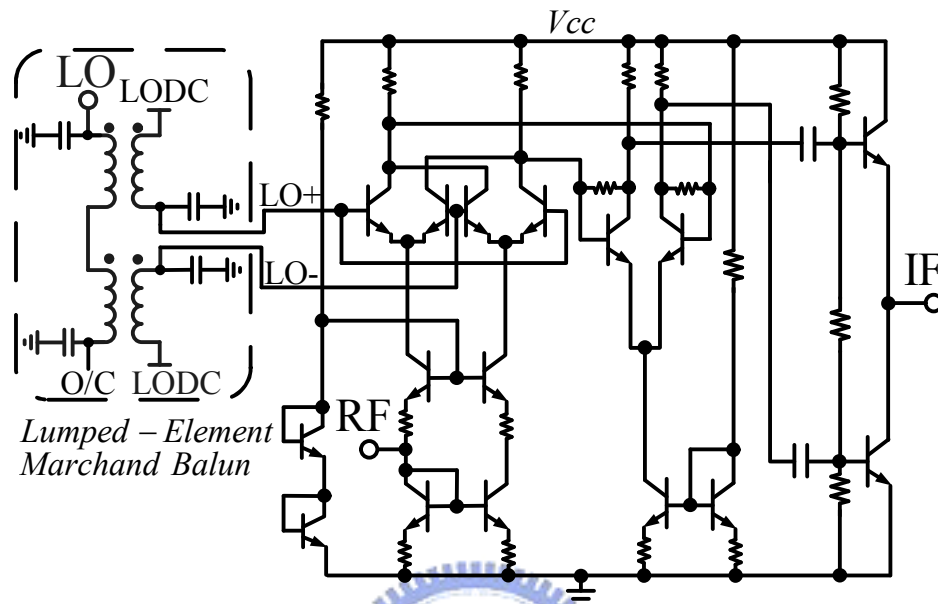
Fig. 5-20   Schematic of the UWB Gilbert down-conversion mixer with an LO lumped-element Marchand balun.
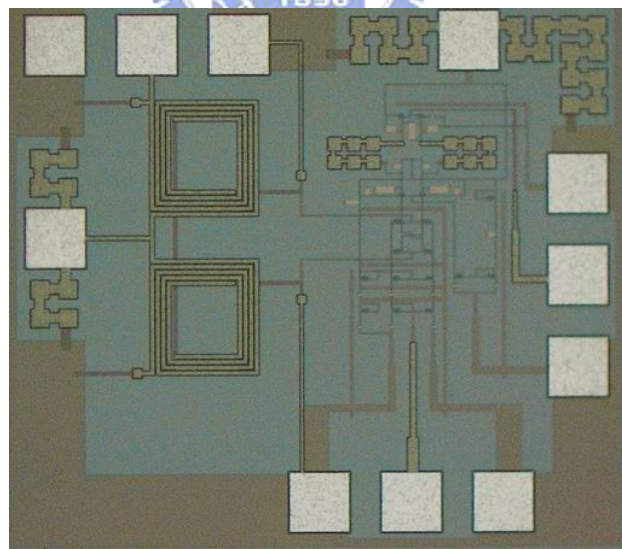
Fig. 5-21   Die photograph of the lumped-element Marchand balun micromixer.

Because of the wideband balanced outputs of the lumped-element Marchand balun and the broadband mixing of the Gilbert cell, this single-ended micromixer has

the property of wideband mixing operation, as shown in Fig. 5-22, and the mixer functions from 3.1 GHz to 10.6 GHz with the conversion gain of around 15.5 dB and within the gain flatness of 1 dB. In UWB applications, the 3.1-10.6 GHz bandwidth is divided into five band groups and 14 bands. Each band group in the first four band groups consists of three bands and the last band group consists of two bands. The power performances are IP_{1dB}=-14.5 dBm and IIP_3=-3.6 dBm at 3.96 GHz (the center frequency for band 2 of band group 1), IP_{1dB}=-14 dBm and IIP_3=-4.2 dBm at 5.544 GHz (the center frequency for band 5 of band group 2), IP_{1dB}=-12.3 dBm and IIP_3=-1.9 dBm at 7.128 GHz (the center frequency for band 8 of band group 3), IP_{1dB}=-13.5 dBm and IIP_3=-3.1 dBm at 8.712 GHz (the center frequency for band 11 of band group 4), and IP_{1dB}=-14.6 dBm and IIP_3=-2.9 dBm at 10.296 GHz (the center frequency for band 14 of band group 5).
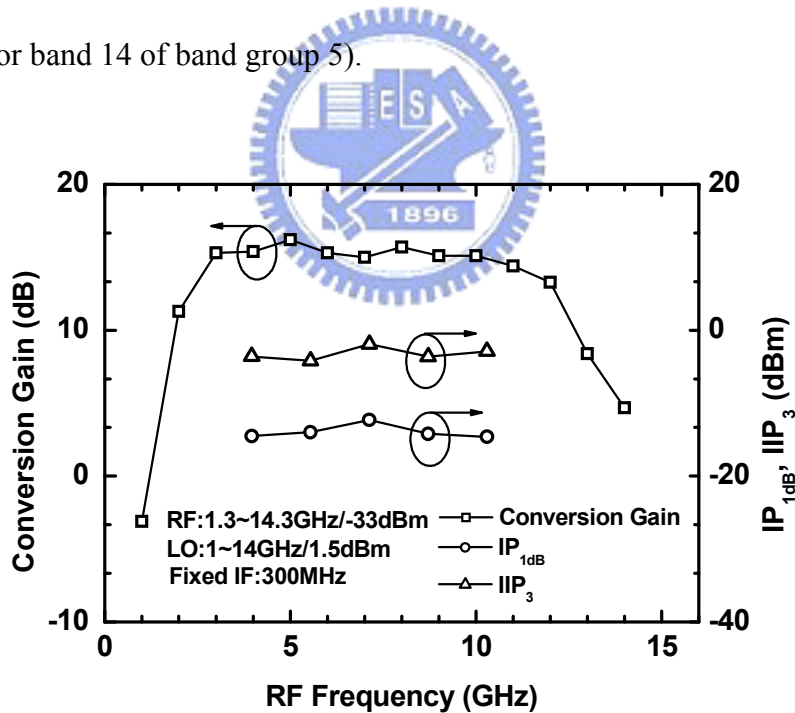
Fig. 5-22   Conversion gain, IP_{1dB} and IIP_3 of the UWB Gilbert down-conversion mixer with an LO lumped-element Marchand balun with respect to RF frequencies.

Fig. 5-23 illustrates the noise figure and conversion gain of the lumped-element Marchand balun micromixer with respect to the IF frequency at the fixed LO

frequency of 4.9 GHz. The LO driven power of only 1.5 dBm agrees well with that the balun loss is acceptable. Here, the output balance is more important than the loss. The noise figure is approximately 15.8 dB and the IF 3-dB bandwidth is approximately 1.5 GHz. The capacitor of 3 pF in the output stage conquers the dc offset and however limits the low IF band operation. The higher capacitance is needed if a lower IF corner frequency is desired.
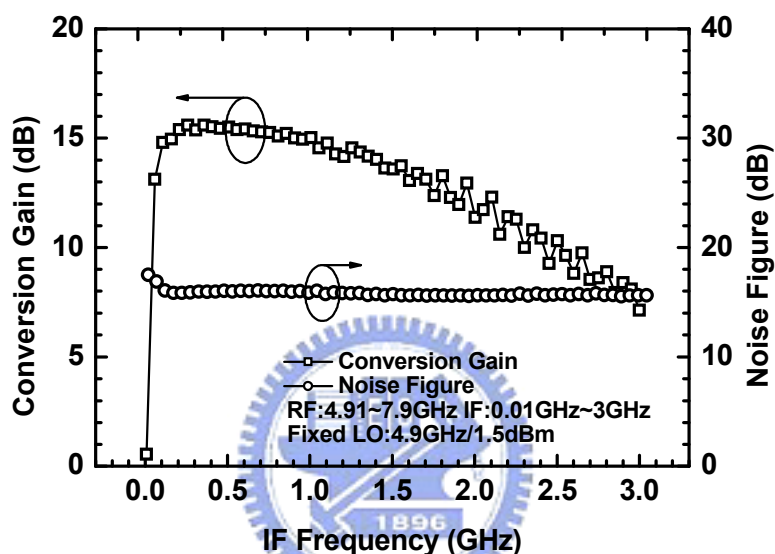
Fig. 5-23   Conversion gain and noise figure of the UWB Gilbert down-conversion mixer with an LO lumped-element Marchand balun with respect to IF frequencies.

The LO-to-IF and LO-to-RF isolations are below -40 dB while the RF-to-IF isolation is approximately -20 dB, as shown in Fig. 5-24. In addition, the RF input return loss and the IF output return loss are less than -20 dB and -10 dB, respectively, among whole UWB bands, as shown in Fig. 5-25. Therefore, this mixer is suitable for 5-group and 14-band UWB applications.
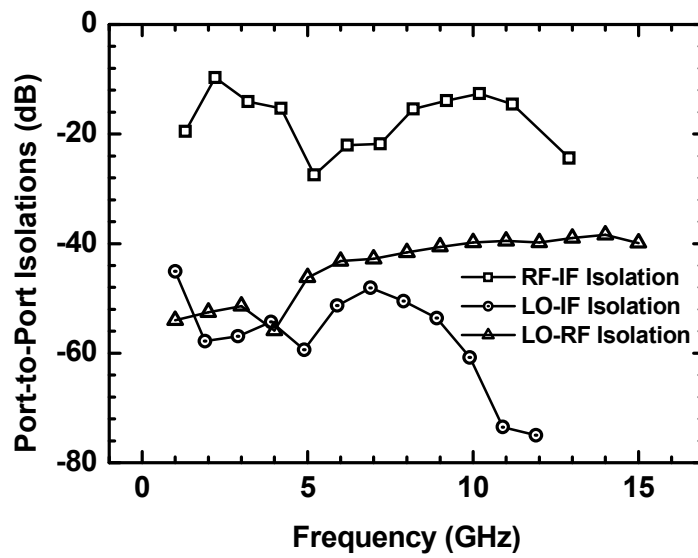
Fig. 5-24   Port-to-port isolations of the UWB Gilbert down-conversion mixer with an LO lumped-element Marchand balun.
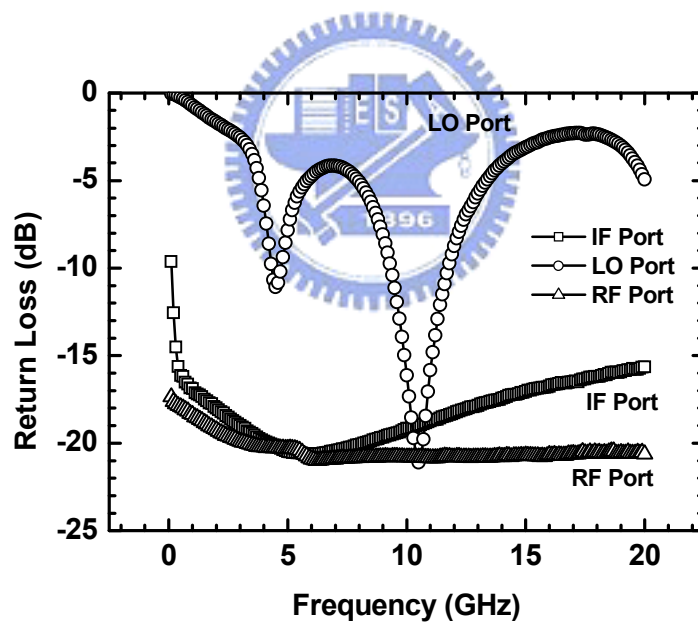
Fig. 5-25   Return loss of the UWB Gilbert down-conversion mixer with an LO lumped-element Marchand balun.

TABLE 5.1 Measurement Results of the Implemented Marchand Baluns and Their Applications in Mixers

Item	TSMC 0.35-µm 2P4M CMOS	TSMC 0.35-µm 3P3M SiGe BiCMOS		
	Planar Marchand Balun	Lumped-Element Balun	Mixer with a Marchand Balun	Mixer with a Lumped-Element Balun
Frequency (GHz)	4 ~ 16	2.5 ~ 12	3.5 ~ 14.5	3.1 ~ 10.6
Phase Error (°)	± 20	3.5 ~ 7		
Magnitude Imbalance (dB)	2 ~ 3	< 1		
Dissipated Loss (dB)	~ 6	< 4		
Max S_{21} (dB)	~ -10	-6.8		
Fractional Bandwidth (3-dB S_{21} Bandwidth) (%)	120	131		
Conversion Gain (dB)			15	15.5
LO Power (dBm)			6	1.5
IF Bandwidth (GHz)			0.4	1.5
IP_{1dB} (dBm)			-19	-13 ~ -14
IIP_3 (dBm)			-7	-2 ~ -4
RF Return Loss (dB)			< -14	< -20
IF Return Loss (dB)			< -10	< -10
Noise Figure (dB)			13	15.8
Supply Voltage (V)			5	5
Power Dissipation (mW)			60 (Core)	69.5 (Total)
Balun/Chip Size (mm × mm)	0.25 ×0.66	0.25 × 0.5	1 × 1	1× 0.9

5.4 SUMMARY

In this chapter, a heuristic approach to derive the three-port scattering parameters of the lossy Marchand balun has been introduced. The appropriate Marchand balun topology with the capability of resisting the loss in the standard silicon IC process has been identified. A single-ended wideband Gilbert mixer with the integrated planar Marchand balun has been demonstrated using 0.35-µm SiGe BiCMOS technology. This wideband mixer with the integrated Marchand balun has the conversion gain of 15 dB, IP_{1dB} of -19 dBm, IIP_3 of -7 dBm, IIP_2 of 12 dBm, a minimum noise figure of 13 dB, and works from 3.5 to 14.5 GHz with 400-MHz IF bandwidth. The lower bound of 3.5 GHz is limited by the LO stage, while the upper bound of 14.5 GHz is limited by the RF stage.

A monolithic lumped-element Marchand balun and a wideband micromixer

integrated with this Marchand balun are also fabricated using the standard 0.35-μm SiGe BiCMOS process. Though the balun is realized on a lossy substrate, the dissipated loss of the balun is still less than 4 dB and the magnitude and phase errors of outputs are below 1 dB and approximately 184°, respectively, thanks to the balanced structure of the Marchand balun and the advantage of the lumped-element technique. Integrating Marchand balun into the standard silicon IC overcomes the imbalance from the external balun and cables as well as reducing production cost due to the high integration. The micromixer has single-ended inputs and output and works from 3.1 to 10.6 GHz with the 15.5-dB conversion gain and within the 1-dB gain flatness. Besides, this mixer is also in possession of the IF 3-dB bandwidth of 1.5 GHz, noise figure of 15.8 dB, IP_{1dB} of approximately -14 dBm, and IIP_3 of approximately -3 dBm.

Chapter 6 Standard Silicon-Based Wideband Balun Design With Coupling Factor and Characteristic Impedance

6.1 INTRODUCTION

Many microwave passive components, such as Marchand baluns, rat-race hybrids, branch-line couplers, and Wilkinson power dividers, are integrated into a chip, not only to reduce the assembly cost, but also to eliminate the signal imbalance caused by external elements, especially at high frequencies. Also, IC technology with multiple metal layers facilitates the implementation of microwave components. Operation bandwidth requirement increases with data throughput and multiple-integrated communication systems, so a wideband balun is demanded. As shown in Fig. 6-1(a), planar Marchand baluns, composed of two back-to-back $\lambda/4$ coupled lines, are commonly used as a wideband single-to-differential converter, thanks to both a more reasonable size as compared with rat-race couplers and to a better performance in comparison with transformer baluns [42], [55], [58], [62]. Recently, the Marchand balun is plentifully employed in ICs [75]–[77]. Though Ang and Lin provided the complete analyses of the planar Marchand balun, all analyses are done under a lossless condition and are based on ideal coupled lines with perfect matching and isolation [63], [77], [78]. Although the balun had successfully been fabricated on a standard silicon substrate for a compact size in Chapter 5, the detailed analysis and the optimal design for a lossy balun are needed [21]. In this study, the baluns are analyzed generally in a homogeneous material, in order to realize a standard silicon-based balun directly on a lossy substrate.
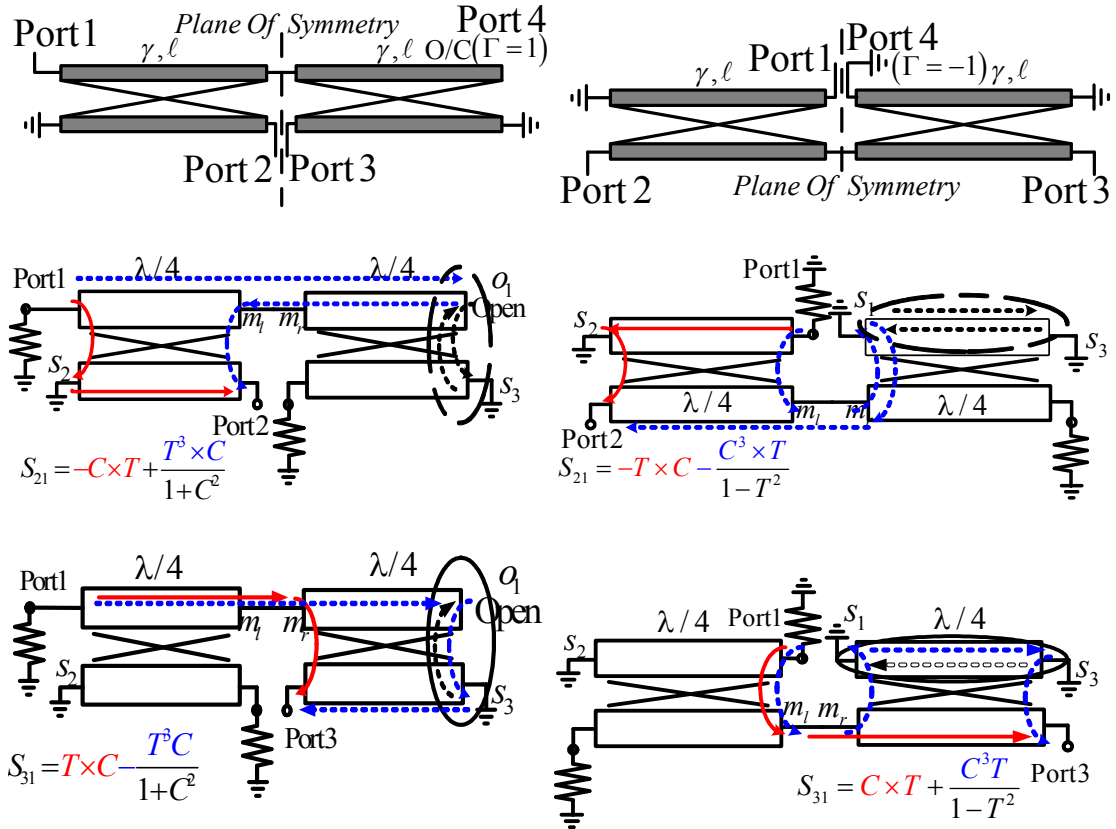
(a) Basic Marchand balun   (b) Modified Marchand balun

Fig. 6-1   Wideband baluns based on two $\lambda/4$ coupled lines. (C $\leftrightarrow$ T; Open $\rightarrow$ Short)

Transmission-line characteristic impedance is applied for the bandwidth optimization of the compensated Marchand balun [59], [76], [79], while the coupling factor of the coupled lines in the planar Marchand balun determinates operation bandwidth [70], [77]. Nonetheless, the coupled-line characteristic impedance is fixed with the terminal impedance in [77] as usual for the perfect matching and isolation of the coupled line. Under this constrain, the coupling factor should equal $\sqrt{1/3}$ for the input matching of the balun [63]. Therefore, a high coupling factor brings about high-operation bandwidth at the cost of the matching degradation and insertion ripples of the Marchand balun [77]. Even when the coupling factor is larger than 0.63, a cavern in the transmission coefficient occurs at the center frequency. In this dissertation, the optimal characteristic impedance is designed with respect to the

coupling factor, and then the balun operation bandwidth increases with the coupling factor without the insertion-loss ripple and the degradation of input matching.

According to our analysis, the modified Marchand balun shown in Fig. 6-1(b), which is a variation of the planar Marchand balun proposed in [80], can be implemented with a much higher operation bandwidth. This type is modified from the conventional planar Marchand balun, by exchanging coupling and through operations and by replacing the open terminal with a short circuit. In this chapter, the complete analysis and implementation of this modified Marchand balun have been done for the first time, to the best of our knowledge. Using the same coupled-line characteristic impedance, this balun is realized with a higher coupling factor in comparison with the basic Marchand balun, and thus the operation bandwidth is larger. Due to the formidable implementation of the high-coupling coupled line on a printed circuit board, the modified Marchand balun is rarely used. However, high coupling is easily achieved in integrated circuits by a broadside-coupling technique. In this study, the silicon-based modified Marchand balun operates from 4 to 25 GHz with the outputs of an 180±5° phase difference and a ±0.5-dB magnitude imbalance, and the measured fractional bandwidth reaches more than 140%. In addition, two wideband balun applications in Gilbert mixers are demonstrated using 0.35-μm SiGe BiCMOS. As compared with the basic Marchand balun mixer, there is more than a 30% bandwidth extension in the Gilbert mixer with an integrated modified balun.

6.2 ANALYSIS AND DESIGN OF BROADBAND BALUNS ON A STANDARD SILICON SUBSTRATE

A broadband balun, implemented on a standard silicon substrate for size reduction, should have a symmetrical structure to provide balanced outputs. A basic

Marchand balun and its variation, denoted as a modified Marchand balun, are fully symmetrical and are shown in Fig. 6-1 [80]. By exchanging coupling and through operations, the modified Marchand balun is reformed from the basic counterpart, and then this new structure can be designed with a high coupling factor, high bandwidth, and practicable characteristic impedance. In this section, we analyze both configurations of baluns in the case of loss, with a coupling factor and its optimized characteristic impedance, and then make a comparison in terms of operation bandwidth.

(a) Even mode of the basic Marchand balun   (b) Even mode of the modified Marchand balun

(c) Odd mode of both baluns
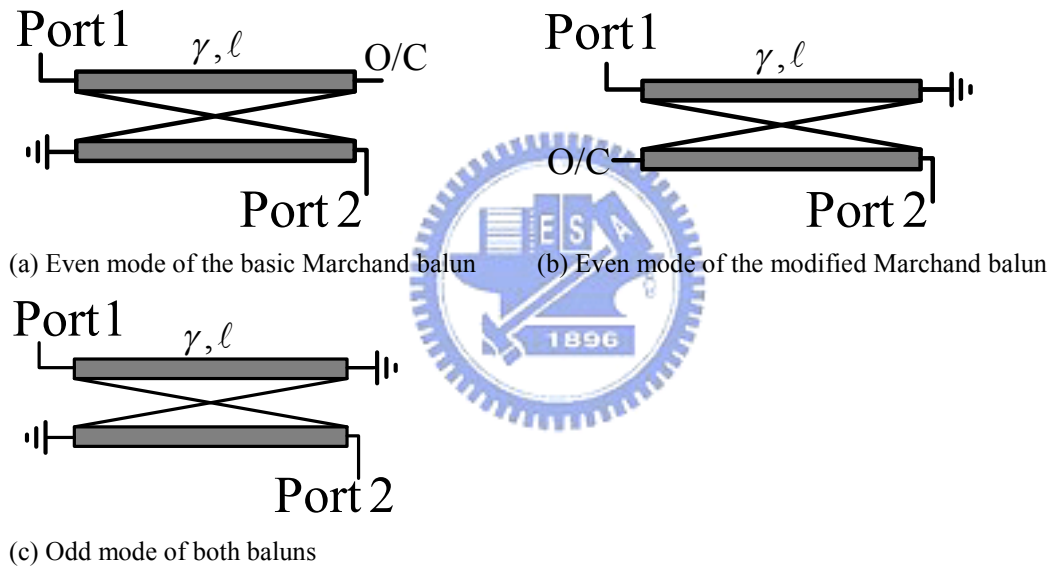
Fig. 6-2   Even- and odd-mode analyses of the basic and modified Marchand baluns.

6.2.1 Analysis in the Case of Loss

First, we start with a lossy coupled line in a homogeneous material. As is derived from Appendix C, the coupled-line S-matrix is defined as

$$[S]_{C.L.} = \begin{bmatrix} R & I & C & T \\ I & R & T & C \\ C & T & R & I \\ T & C & I & R \end{bmatrix} \tag{6.1}$$

where R, I, C, and T are the reflection, isolation, coupling, and through coefficients of

the coupled line, respectively. Fig. 6-1(a) and (b) display that 3-port baluns, based on two coupled lines, can be viewed as a 4-port passive component whose port 4 is short- or open-circuited. Those 4-port passive components is symmetrical and can be analyzed in the even and odd modes, as shown in Fig. 6-2(a), (b), and (c) [51]. Based on (6.1), the even-mode and odd-mode S-matrices of the modified Marchand balun are expressed by

$$
\begin{bmatrix} S_{11}^e & S_{12}^e \\ S_{21}^e & S_{22}^e \end{bmatrix}_{m.M.B.} = \begin{bmatrix} R + \dfrac{2ICT - R(C^2 + T^2) - C^2 + T^2}{R^2 - I^2 - 1} & I + \dfrac{I(C^2 + T^2) - 2RCT}{R^2 - I^2 - 1} \\ I + \dfrac{I(C^2 + T^2) - 2RCT}{R^2 - I^2 - 1} & R + \dfrac{2ICT - R(C^2 + T^2) + C^2 - T^2}{R^2 - I^2 - 1} \end{bmatrix} \quad (6.2)
$$

and

$$
\begin{bmatrix} S_{11}^o & S_{12}^o \\ S_{21}^o & S_{22}^o \end{bmatrix}_{m.M.B.} = \begin{bmatrix} R + \dfrac{2ICT - R(C^2 + T^2) - C^2 - T^2}{(R+1)^2 - I^2} & I + \dfrac{I(C^2 + T^2) - 2(R+1)CT}{(R+1)^2 - I^2} \\ I + \dfrac{I(C^2 + T^2) - 2(R+1)CT}{(R+1)^2 - I^2} & R + \dfrac{2ICT - R(C^2 + T^2) - C^2 - T^2}{(R+1)^2 - I^2} \end{bmatrix}, (6.3)
$$

and its 4-port S-matrix is derived as

$$
[S]_{s4p} = \begin{bmatrix}
\frac{1}{2}(S_{11}^e + S_{11}^o) & \frac{1}{2}(S_{12}^e + S_{12}^o) & \frac{1}{2}(S_{12}^e - S_{12}^o) & \frac{1}{2}(S_{11}^e - S_{11}^o) \\
\frac{1}{2}(S_{21}^e + S_{21}^o) & \frac{1}{2}(S_{22}^e + S_{22}^o) & \frac{1}{2}(S_{22}^e - S_{22}^o) & \frac{1}{2}(S_{21}^e - S_{21}^o) \\
\frac{1}{2}(S_{21}^e - S_{21}^o) & \frac{1}{2}(S_{22}^e - S_{22}^o) & \frac{1}{2}(S_{22}^e + S_{22}^o) & \frac{1}{2}(S_{21}^e + S_{21}^o) \\
\frac{1}{2}(S_{11}^e - S_{11}^o) & \frac{1}{2}(S_{12}^e - S_{12}^o) & \frac{1}{2}(S_{12}^e + S_{12}^o) & \frac{1}{2}(S_{11}^e + S_{11}^o)
\end{bmatrix}.
$$
$$
= \begin{bmatrix}
a & c & d & b \\
c & e & f & d \\
d & f & e & c \\
b & d & c & a
\end{bmatrix}
$$
(6.4)

Port 4 in the modified Marchand balun is a short terminal, and the 3-port S-matrix of the modified balun is finally written as

$$[S]_{m.M.B.} = \begin{bmatrix} a - \dfrac{b^2}{1+a} & c - \dfrac{bd}{1+a} & d - \dfrac{bc}{1+a} \\[3mm] c - \dfrac{bd}{1+a} & e - \dfrac{d^2}{1+a} & f - \dfrac{cd}{1+a} \\[3mm] d - \dfrac{bc}{1+a} & f - \dfrac{cd}{1+a} & e - \dfrac{c^2}{1+a} \end{bmatrix}. \qquad (6.5)$$

Via the manual derivation shown in Appendix D, $S^e_{21,m.M.B}$ equals zero. This is because waves propagating to the other port via a short terminal will be cancelled with those through an open end, as shown in Fig. 6-2(a). Accordingly, c is equal to $-d$ in (6.4), so that $S_{21,m.M.B.}$ is equal to $-S_{31,m.M.B.}$ in all frequencies. This balun always has truly differential outputs even in the case of loss.

The same derivation approach is applied for the basic Marchand balun. In comparison with the modified one, the odd-mode analysis of the basic Marchand balun is the same, but, in the even mode, the reflection coefficients of Ports 1 and 2 are exchanged. In addition, Port 4 of the basic Marchand balun is open-ended, and hence, its 3-port S-matrix is formulized by

$$[S]_{b.M.B.} = \begin{bmatrix} e + \dfrac{f^2}{1-e} & c + \dfrac{fd}{1-e} & d + \dfrac{fc}{1-e} \\[3mm] c + \dfrac{fd}{1-e} & a + \dfrac{d^2}{1-e} & b + \dfrac{cd}{1-e} \\[3mm] d + \dfrac{fc}{1-e} & b + \dfrac{cd}{1-e} & a + \dfrac{c^2}{1-e} \end{bmatrix} = \begin{bmatrix} e + \dfrac{f^2}{1-e} & c - \dfrac{fc}{1-e} & -c + \dfrac{fc}{1-e} \\[3mm] c - \dfrac{fc}{1-e} & a + \dfrac{c^2}{1-e} & b - \dfrac{c^2}{1-e} \\[3mm] -c + \dfrac{fc}{1-e} & b - \dfrac{c^2}{1-e} & a + \dfrac{c^2}{1-e} \end{bmatrix}. \quad (6.6)$$

Similarly, the basic Marchand balun has differential outputs. The fact that the outputs of the homogeneous coupled-line-based baluns were always balanced in magnitude and phase within all frequency ranges was found in this dissertation for the first time to the best of our knowledge. Not only that, but this outcome also supports our previous work in Chapter 5, directly implemented on a lossy silicon substrate [21].

For a special case, the complex characteristic impedance of the coupled line, $\hat{Z}_C = \sqrt{\hat{Z}_{0e}\hat{Z}_{0o}}$, is equal to the terminal impedance Z_0, so that the reflection R and

isolation I of the coupled line are zero. As a consequence, the 3-port S-matrices of the basic and modified Marchand baluns become

$$[S]_{b.M.B.} = \begin{bmatrix} -C^2 + \dfrac{T^4}{1+C^2} & -CT + \dfrac{CT^3}{1+C^2} & CT - \dfrac{CT^3}{1+C^2} \\[2mm] -CT + \dfrac{CT^3}{1+C^2} & -T^2 + \dfrac{C^2T^2}{1+C^2} & C^2 - \dfrac{C^2T^2}{1+C^2} \\[2mm] CT - \dfrac{CT^3}{1+C^2} & C^2 - \dfrac{C^2T^2}{1+C^2} & -T^2 + \dfrac{C^2T^2}{1+C^2} \end{bmatrix} \tag{6.7}$$

and

$$[S]_{m.M.B.} = \begin{bmatrix} -T^2 - \dfrac{C^4}{1-T^2} & -TC - \dfrac{TC^3}{1-T^2} & TC + \dfrac{TC^3}{1-T^2} \\[2mm] -TC - \dfrac{TC^3}{1-T^2} & -C^2 - \dfrac{T^2C^2}{1-T^2} & T^2 + \dfrac{T^2C^2}{1-T^2} \\[2mm] TC + \dfrac{TC^3}{1-T^2} & T^2 + \dfrac{T^2C^2}{1-T^2} & -C^2 - \dfrac{T^2C^2}{1-T^2} \end{bmatrix}, \tag{6.8}$$

respectively. (6.7) is well-known [69], while (6.8) has been first reported in this dissertation. (6.7) and (6.8) are similar, apparently because these two structures have duality in coupling and through operations.

6.2.2 Analysis in Bandwidth

For the purpose of realizing the operation bandwidth of baluns, we start with the analysis in the case of lossless. In order to achieve the input matching of the modified Marchand balun at the center frequency, $S_{11,m.M.B.}=0$, $S^e_{11,m.M.B.}$ and $S^o_{11,m.M.B.}$ should equal 1 and -1/3, respectively, based on (6.2)–(6.5) and $S^e_{21,m.M.B.} = 0$ [81]. As is derived from Appendix E, the optimized characteristic impedance of the modified Marchand balun is designed as

$$Z_{C,m.M.B.} = \frac{k}{\sqrt{2\left(1-k^2\right)}} Z_0, \tag{6.9}$$

with the coupling factor k and the terminal impedance Z_0. For the basic Marchand

balun, the input matching is achieved at the center frequency when $S^e_{11,b.M.B.} = -1$ and

$S^o_{11,b.M.B.} = 1/3$. According to the derivation shown in Appendix E, the characteristic

impedance of the prototype balun is figured out as

$$Z_{C,b.M.B.} = \sqrt{\frac{2}{(1-k^2)}} k Z_0 \,, \tag{6.10}$$

Fig. 6-3 and Fig. 6-4 clearly illustrate that a high coupling factor results in a high

operation bandwidth, because R, I, C, and T with high coupling factors are insensitive

to operation frequency [77], [82]. The fractional bandwidth stands for $(f_{max}-f_{min})/f_{center}$.

The characteristic impedance of baluns is optimized with high coupling factor for the

bandwidth extension in transmission and input matching simultaneously. The optimal

characteristic impedance settles the insertion-loss ripples, as mentioned in [77] as

well.

The desired characteristic impedance of the modified Marchand balun is a half of

that of the basic one. Therefore, based on the same characteristic impedance, the

modification has a higher coupling factor and wider operation bandwidth than the

prototype. For a special case, $Z_C=Z_0$, and then R, I, C, and T are equal to 0, 0, k, and

$-j\sqrt{1-k^2}$ at the center frequency, respectively. Thus, the S-matrix of the modified

Marchand balun is expressed as

$$[S]_{v.M.B.} = \begin{bmatrix} \dfrac{2-3k^2}{2-k^2} & j\dfrac{2k\sqrt{1-k^2}}{2-k^2} & -j\dfrac{2k\sqrt{1-k^2}}{2-k^2} \\ j\dfrac{2k\sqrt{1-k^2}}{2-k^2} & \dfrac{-k^2}{2-k^2} & \dfrac{2k^2-2}{2-k^2} \\ -j\dfrac{2k\sqrt{1-k^2}}{2-k^2} & \dfrac{2k^2-2}{2-k^2} & \dfrac{-k^2}{2-k^2} \end{bmatrix} . \tag{6.11}$$

When $k = \sqrt{2/3}$, input matching is achieved at the center frequency. With the same

design parameter of $Z_C = Z_0$, the bandwidth enhancement is more than 20% for the modified Marchand balun in comparison with the original type.
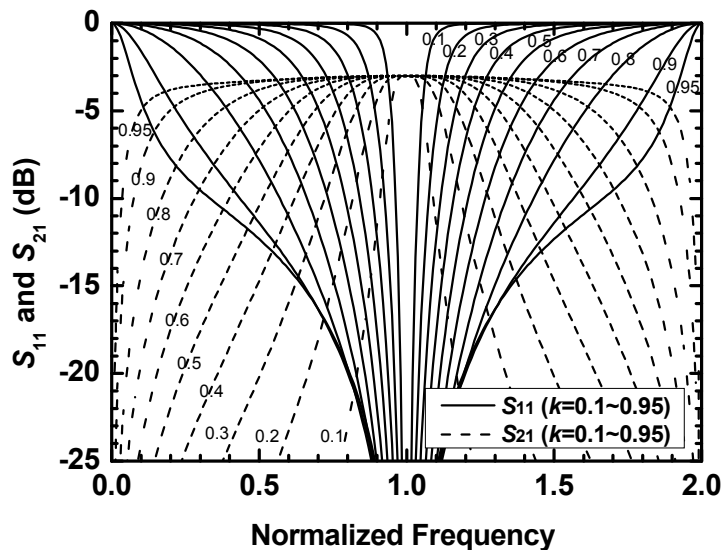
(a) S_{11} and S_{21}
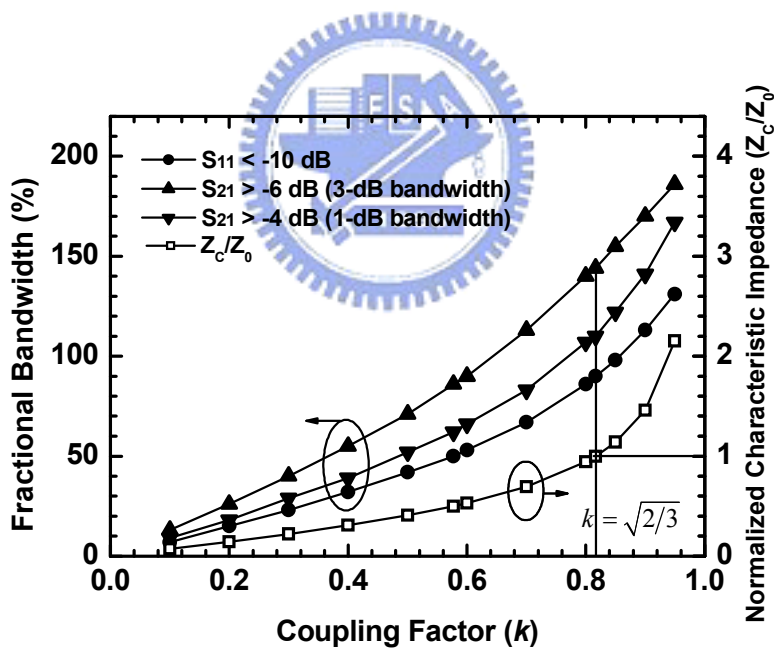
(b) Bandwidth and optimal characteristic impedance for input matching

Fig. 6-3   Operation bandwidth analysis of the lossless modified Marchand balun.
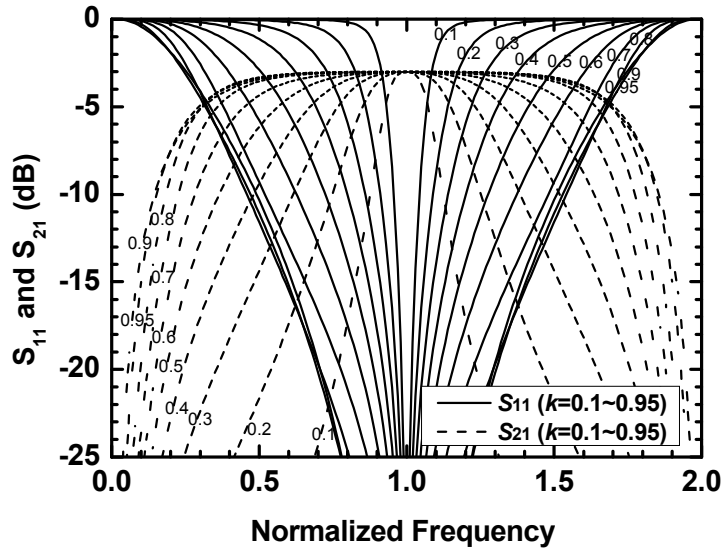
(a) S_{11} and S_{21}
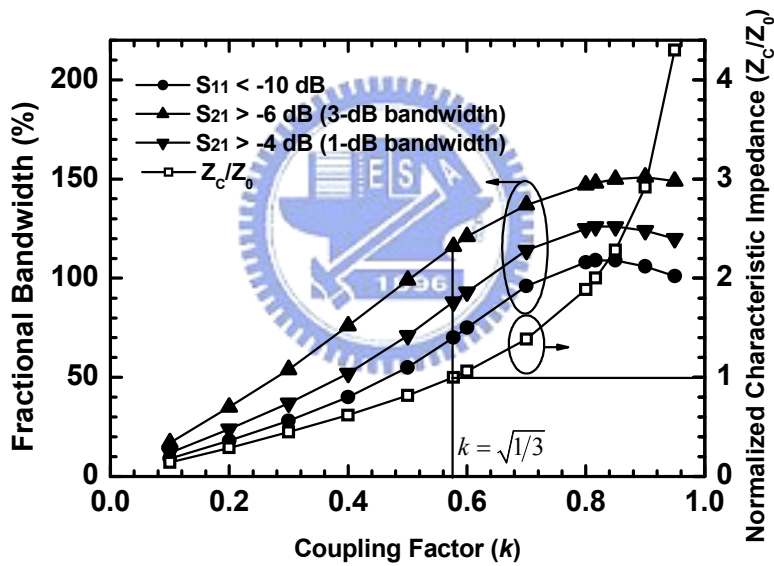
(b) Bandwidth and optimal characteristic impedance for input matching

Fig. 6-4   Operation bandwidth analysis of the lossless basic Marchand balun.

The analysis in a lossy condition becomes more complicated. However, at the center frequency, $\cosh(\gamma \ell)$ and $\sinh(\gamma \ell)$ in (C.4)–(C.7) can be written as

$$\cosh\left(\alpha\ell + j\pi/2\right) = j\sinh\left(\alpha\ell\right) = j\sinh\left(\frac{\pi}{4Q}\right)$$

$$\approx j\frac{\pi}{4Q}, \quad as\ Q > 5$$

(6.12)

and

$$\sinh\left(\alpha\ell + j\pi/2\right) = j\cosh\left(\alpha\ell\right) = j\cosh\left(\frac{\pi}{4Q}\right),$$

$$\approx j, \quad as\ Q > 5$$

(6.13)

respectively, with the transmission-line quality factor $Q = \pi/(4\alpha l)$ [83]. When Q is

large enough, $\cosh\left(\gamma\ell\right)$ and $\sinh\left(\gamma\ell\right)$ approach 0 and j, respectively, and then the

$$Z_{C,m.M.B.} = \frac{k}{\sqrt{2\left(1-k^2\right)}} Z_0$$

optimal characteristic impedance derived in , (6.9)(6.9)

and (6.10) can be applied for the lossy baluns. For simplification, the attenuation

constant α is assumed to be fixed and the propagation constant β is a linear function of

frequency. Then, the scattering parameters of the lossy modified Marchand balun are

calculated in terms of Q, as shown in Fig. 6-5. Fig. 6-6 depicts that the balun with a

high coupling factor also has a stronger ability to resist the insertion loss caused by a

lossy substrate.
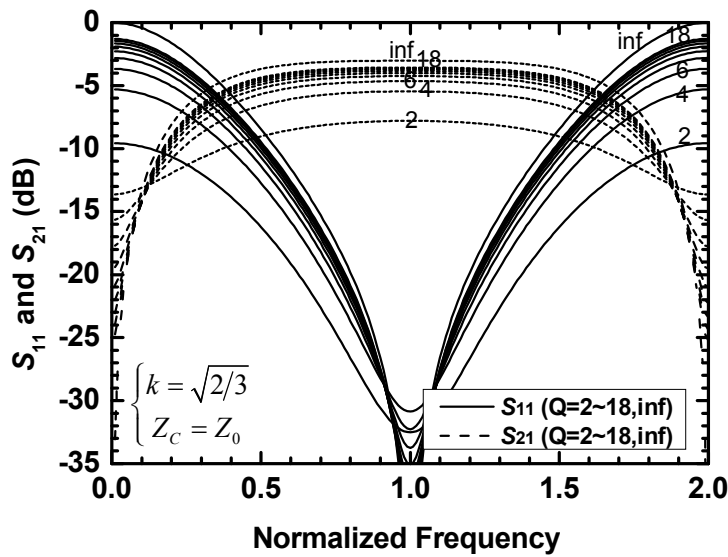
Fig. 6-5 S_{11} and S_{21} of the lossy modified balun with respect to the coupled-line quality factor.
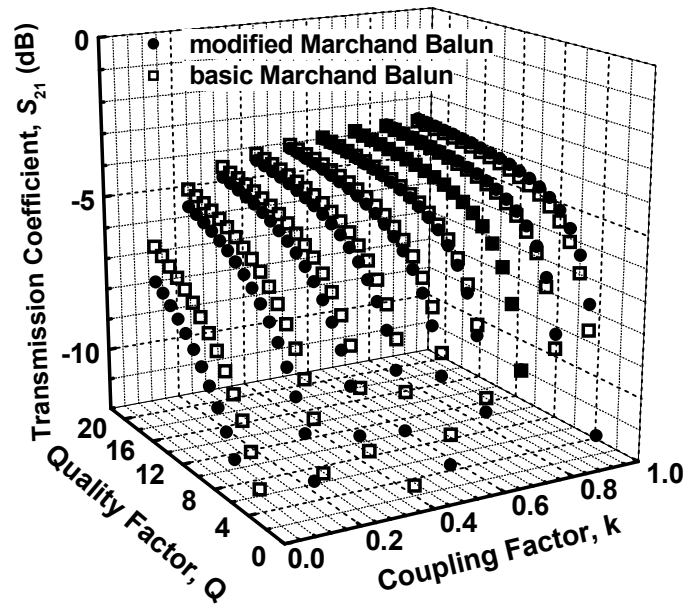
Fig. 6-6   Maximum S_{21} of the lossy baluns with respect to the quality factor and coupling factor.

6.2.3 Implementation

Two kinds of baluns are demonstrated using a standard silicon process. In order to shrink the balun size, the baluns are directly implemented on a lossy silicon substrate without shielding, and a higher dielectric constant is good for size reduction. According to our analysis, substrate loss and metal loss do not influence the balun operation. In IC technology, an edge-coupling technique is utilized for low coupling, while a broadside-coupling technique is employed for high coupling. The distance between two metal layers can be designed as small as 1 μm to achieve the coupling factor of more than 0.8. Furthermore, coupled lines are wound into a spiral shape for compact layout size [69], [71]. For the comparison, two formations of baluns are designed with similar characteristic impedance. Therefore, as shown in Fig. 6-7, in the basic Marchand balun, an interleave transformer with a low coupling factor (0.5~0.7) is used as a coupled line, whereas a stack transformer with a high coupling factor (0.8~0.9) is employed in the modified Marchand balun [84]. Because of the stack

structure of the modified Marchand balun, the balun size is smaller. However, its metal loss is larger due to the usage of thin metals.
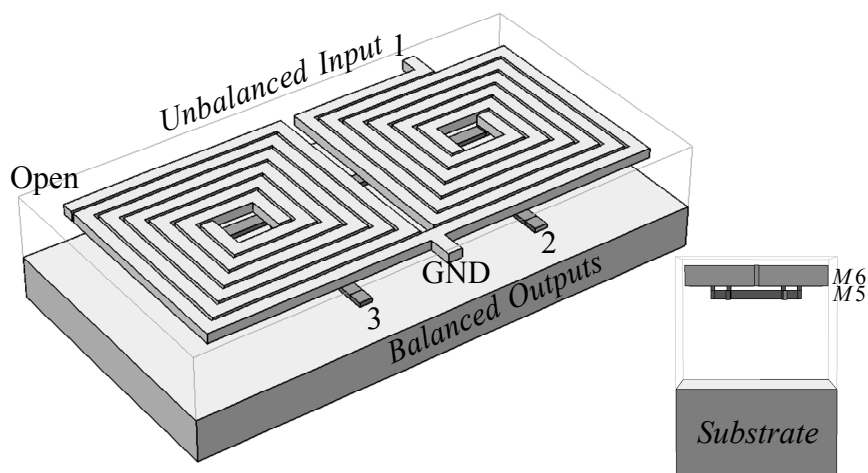
(a) Basic Marchand balun with edge coupling
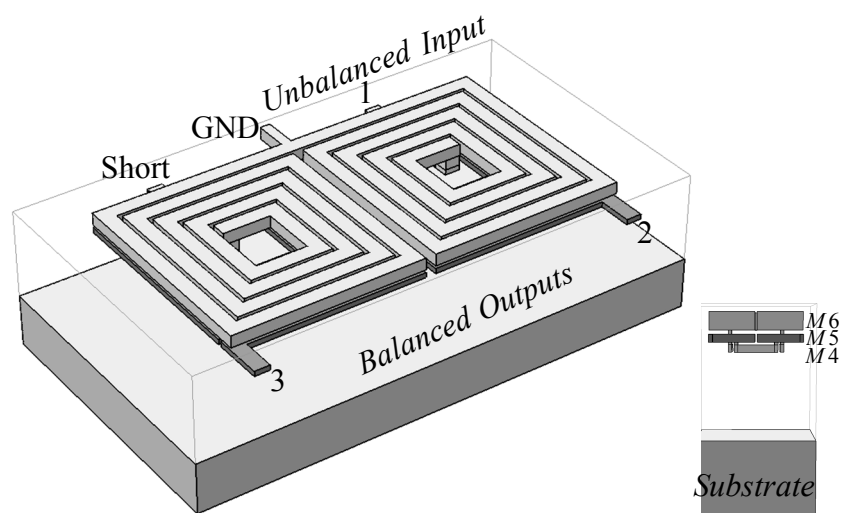
(b) Modified Marchand balun with broadside coupling

Fig. 6-7   3D views of the basic and modified Marchand baluns.

6.3 MEASUREMENT RESULTS

6.3.1 Basic Marchand Balun With Edge Coupling and Its Modification With Broadside Coupling

One basic Marchand balun and its modification are implemented using a standard silicon process with six metal layers, as shown in Fig. 6-8. The size of the original

Marchand balun is 0.17 mm × 0.33 mm, while the modified Marchand balun has an area of 0.13 mm × 0.23 mm.

(a) Prototype Marchand balun.   (b) Modified Marchand balun.
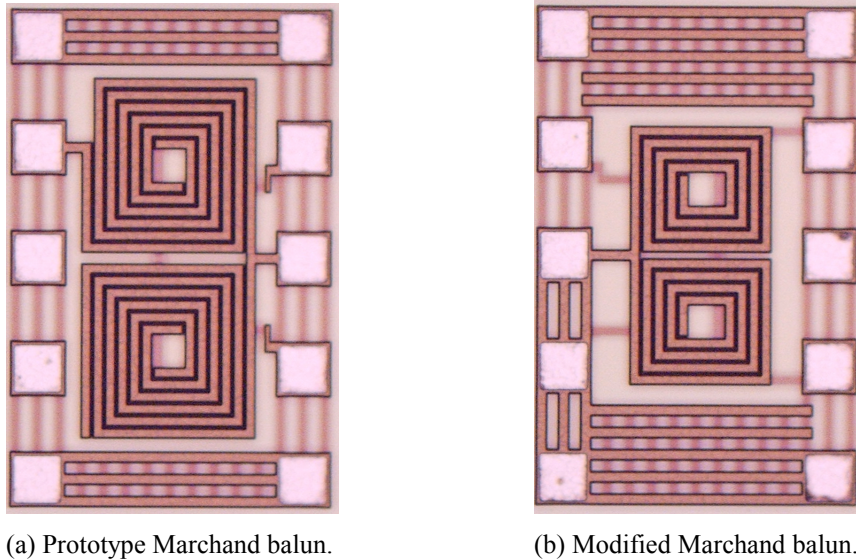
Fig. 6-8   Die photographs of the basic Marchand balun and its modification.

The basic Marchand balun is designed with the conventional design parameters of $k = \sqrt{1/3}$, where the low coupling factor is achieved by an edge-coupling technique. In this balun, two coupled lines are fabricated by the top metal layer with a 2.34-μm thickness and a 9-μm width, and the spacing in the coupled line is 2 μm. The M6-to-substrate distance is 8.15 μm. The measurement, EM simulation, and calculation results are shown in Fig. 6-9. The simulation is done by the EM simulator SONNET as, based on (6.6), the theoretical outcome is calculated with k=0.6, Z_C=65 Ω, and Q=12. The attenuation constant is not constant with frequency so that the transmission coefficient is not flat and S_{21} decreases slightly at high frequencies. The fractional bandwidth is approximately 120% in terms of the 3-dB bandwidth in S_{21}, and the max transmission coefficient is approximately -5 dB.
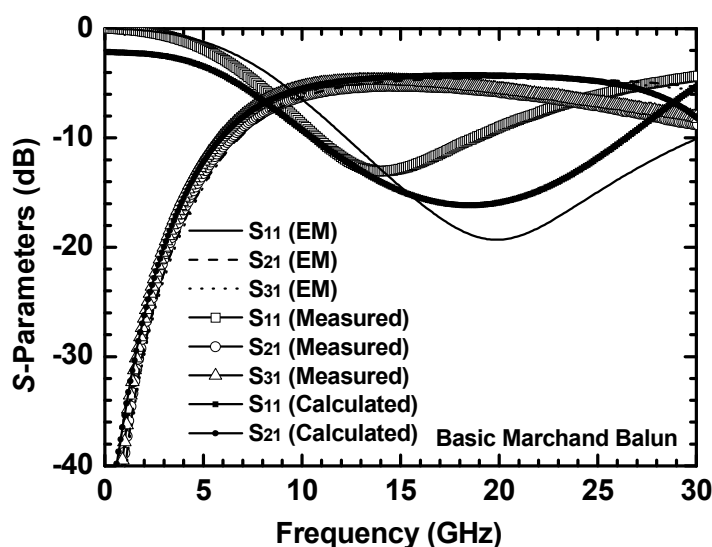
Fig. 6-9   *S*-parameters of the basic Marchand balun.

The coupling factor k is designed as high as $\sqrt{2/3}$ in the modified Marchand balun so that the broadside-coupling technique is used. The modified Marchand balun is formed by the top two metals with thicknesses of 2.34 and 0.53 μm, respectively. The metal width is 9 μm, while the distance between the coupled lines is about 1 μm. The M5-to-substrate distance is 6.62 μm. As shown in Fig. 6-10, the 3-dB S_{21} fractional bandwidth is approximately 147% (6.6:1) and the maximum S_{21} is -6 dB. The theoretical result from (6.5) is calculated with k=0.8, Z_C=50 Ω, and the quality factor is about 4.5.
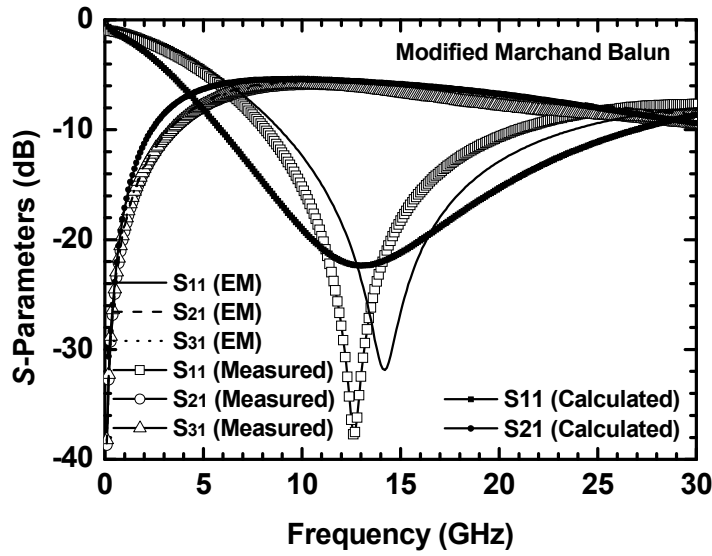
Fig. 6-10   S-parameters of the modified Marchand balun.
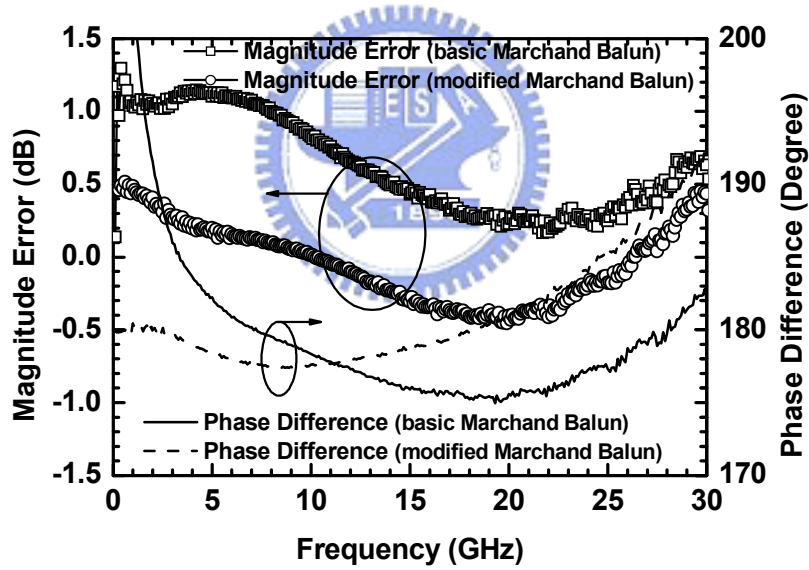
Fig. 6-11   Output imbalance of the basic and modified Marchand baluns.

Fig. 6-11 represents the output balance performances of the conventional Marchand balun and its counterpart. Within 4-25 GHz, the modified Marchand balun has better output performance with a $\pm5°$ phase error and a ±0.5-dB magnitude imbalance. The dissipated loss, $-10\log(|S_{11}|^2+|S_{21}|^2+|S_{31}|^2)$, of the original Marchand balun and the modified Marchand balun is approximately 2 and 3 dB, respectively.

6.3.2 Micromixers With an Integrated LO Wideband Balun

Two applications with a wideband balun in a mixer are also demonstrated in this section. The overall schematic is shown in Fig. 6-12. A basic Marchand balun (or a modified Marchand balun) is employed to generate differential LO signals, while the mixer core is a micromixer with a single-ended RF input and has wideband input-matching [15], [21]. The micromixers with an integrated wideband LO balun are fabricated using 0.35-μm SiGe BiCMOS technology with three metal layers, and they are displayed in Fig. 6-13. The size of the micromixers with a basic Marchand balun and with a modified balun is 0.95×0.86 mm^2 and 0.86×0.71 mm^2, respectively. The latter is smaller thanks to the stack formation in the modified Marchand balun. Each balun size is 0.27×0.5 mm^2 and 0.18×0.35 mm^2, respectively.
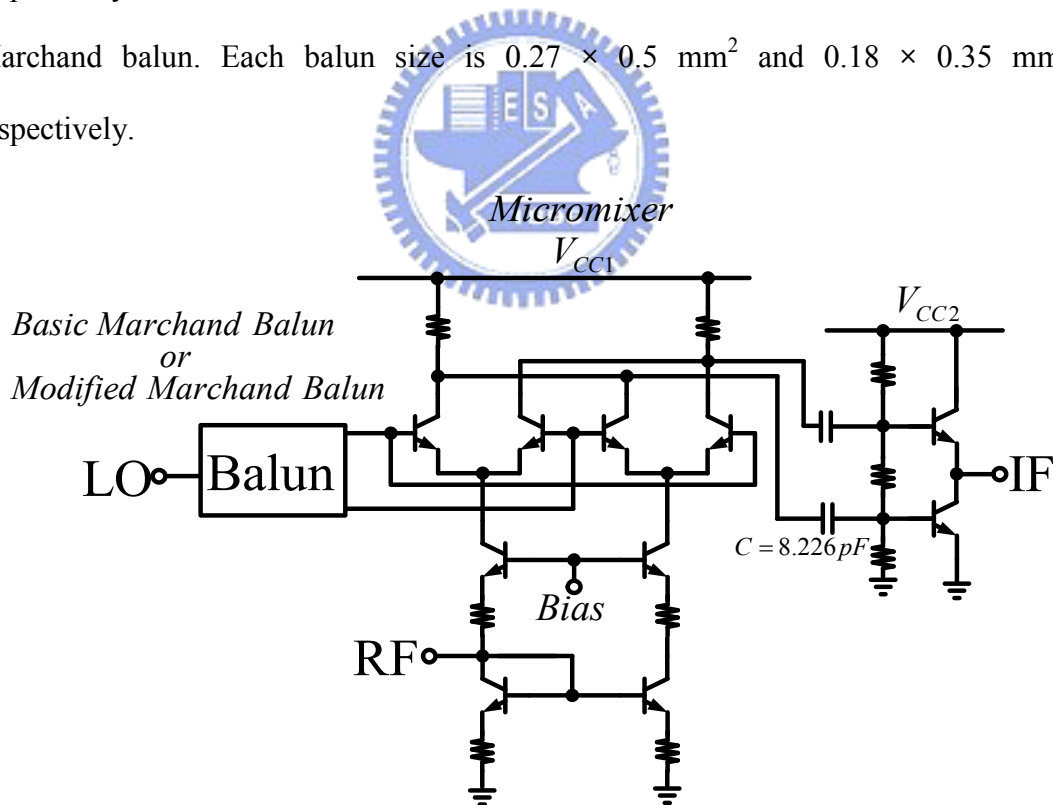
Fig. 6-12   Schematic of the micromixer with an integrated LO wideband balun.
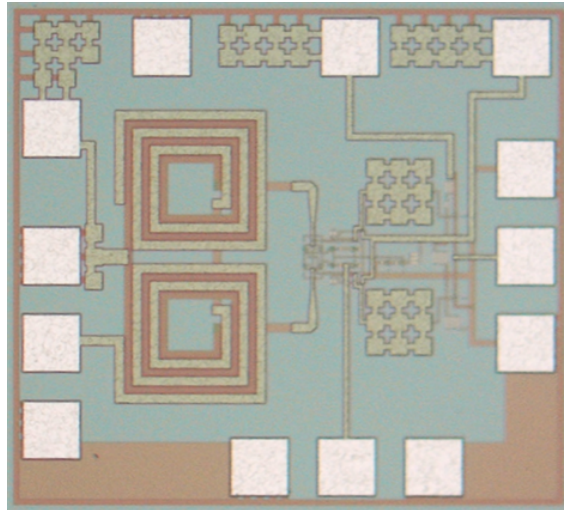
(a) With a basic Marchand balun
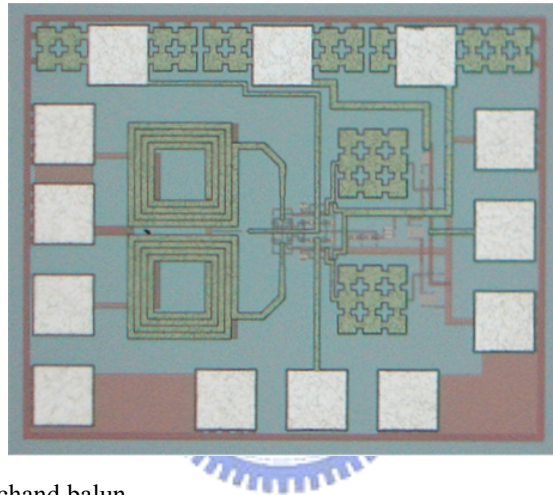
(b) With a modified Marchand balun

Fig. 6-13   Die photographs of the micromixers with a basic Marchand balun and with a modified Marchand balun.

The SiGe HBT devices used in our works are in possession of a 67-GHz peak cut-off frequency. These baluns are different from the individual baluns in Section 6.3.1, and the baluns here are designed with a center frequency of around 7 GHz. The core current consumption of both mixers is almost the same and 2.54 mA at 3.3-V supply voltage. Figs. 14 and 15 illustrate the measured results. Both mixers have the same noise figure of 14 dB and conversion gain of 5 dB at a LO frequency of 6.9 GHz. However, the micromixer with a modified Marchand balun operates up to 15.5 GHz, while the counterpart functions from 2.5 to 12 GHz. The RF 3-dB operation

bandwidth in the modified Marchand balun micromixer is 30% higher than that of the

conventional Marchand balun mixer.
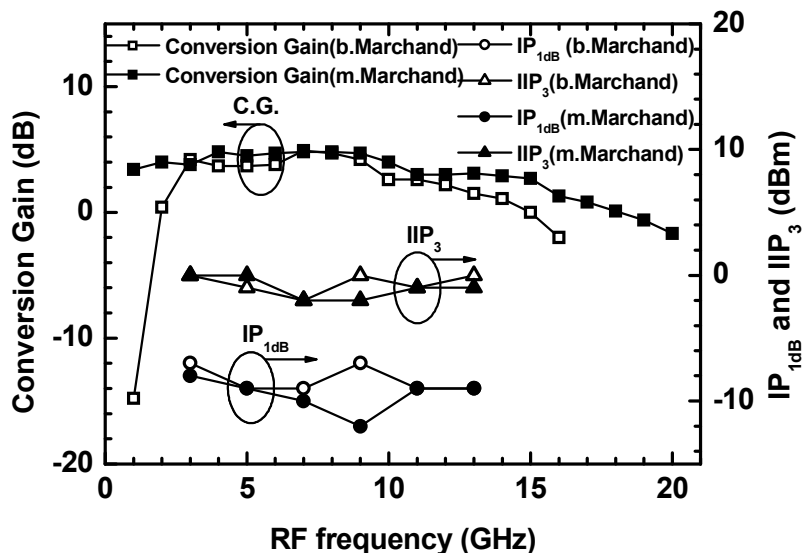
Fig. 6-14   Conversion gain, IP_{1dB}, and IIP_3 of the micromixers with a basic Marchand balun and with a modified Marchand balun.
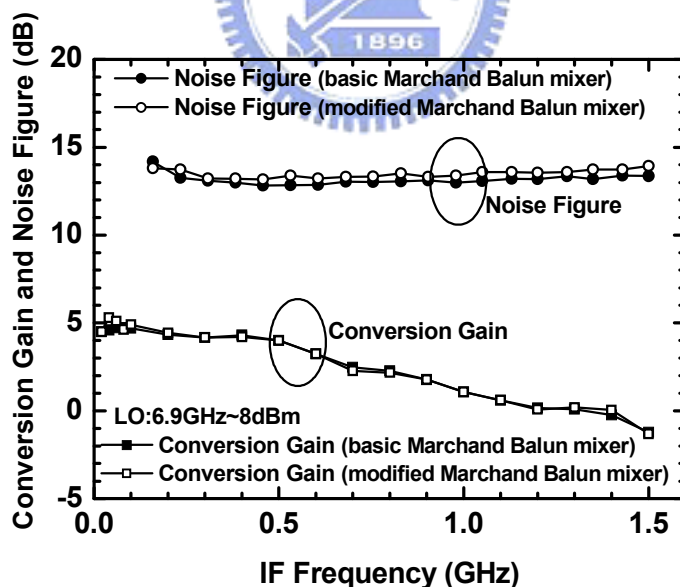
Fig. 6-15   Noise figure and conversion gain of the micromixers with a basic Marchand balun and with a modified Marchand balun.

The LO-to-IF, LO-to-RF, and RF-to-IF isolations are below -25, -25, and -20 dB,

respectively, for both mixers, as shown in Fig. 6-16. Moreover, the RF input matching

is achieved within entire operation frequency ranges, as shown in Fig. 6-17.
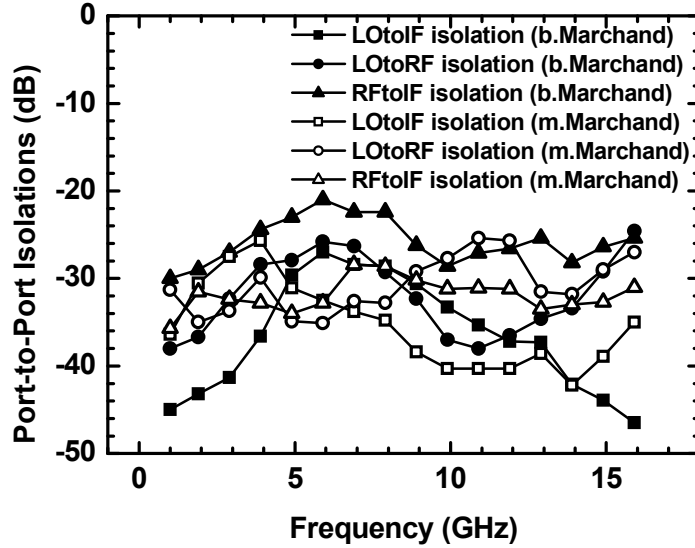
Fig. 6-16   Port-to-port isolations of the micromixers with a basic Marchand balun and with a modified Marchand balun.
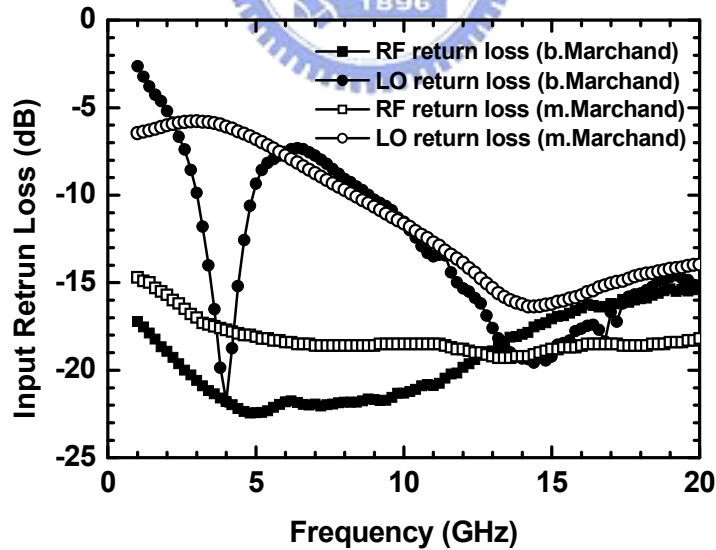
Fig. 6-17   Return loss of the micromixers with a basic Marchand balun and with a modified Marchand balun.

TABLE 6.1 Comparison between Basic Marchand Balun and Modified Marchand Balun

Item	TSMC 0.18-μm 1P6M CMOS		TSMC 0.35-μm 3P3M SiGe BiCMOS	
	Basic Marchand Balun	Modified Marchand Balun	Mixer with a Basic Balun	Mixer with a Modified Balun
Frequency (GHz)	7 ~ 27	4.1 ~ 27	2.5 ~ 12	Up to 15 .5
Phase Error (°)	0 ~ -5	-3~ 7		
Magnitude Imbalance (dB)	< 1	< 0.5		
Dissipated Loss (dB)	~2	~3		
Max S_{21} (dB)	-4.8	-5.8		
Fractional Bandwidth (3-dB S_{21} Bandwidth) (%)	117.6	147.3		
Conversion Gain (dB)			5	5
LO Power (dBm)			5	5
IF Bandwidth (MHz)			900	900
IP_{1dB} (dBm)			-7 ~ -9	-8 ~ -10
IIP_3 (dBm)			0 ~ -2	0 ~ -2
Noise Figure (dB)			14.2	13.8
RF Return Loss (dB)			< -10	< -10
Supply Voltage (V)			3.3	3.3
Core Power Dissipation (mW)			8.382	8.25
Balun/Chip Size (mm × mm)	0.17× 0.33	0.13 × 0.23	0.95 × 0.86	0.86 × 0.71

TABLE 6.2 Comparison in Theory between Basic Marchand Balun and Modified Marchand Balun

Type	Basic Marchand Balun	Modified Marchand Balun
General Condition $\gamma_e=\gamma_o=\gamma$	$\begin{bmatrix} e+\dfrac{f^2}{1-e} & c-\dfrac{fc}{1-e} & -c+\dfrac{fc}{1-e} \\ c-\dfrac{fc}{1-e} & a+\dfrac{c^2}{1-e} & b-\dfrac{c^2}{1-e} \\ -c+\dfrac{fc}{1-e} & b-\dfrac{c^2}{1-e} & a+\dfrac{c^2}{1-e} \end{bmatrix}$	$\begin{bmatrix} a-\dfrac{b^2}{1+a} & c+\dfrac{bc}{1+a} & -c-\dfrac{bc}{1+a} \\ c+\dfrac{bc}{1+a} & e-\dfrac{c^2}{1+a} & f+\dfrac{c^2}{1+a} \\ -c-\dfrac{bc}{1+a} & f+\dfrac{c^2}{1+a} & e-\dfrac{c^2}{1+a} \end{bmatrix}$
Matched Coupled Line $Z_{0e}=Z_{0o}=Z_0^2$ (R=0, I=0)	$\begin{bmatrix} -C^2+\dfrac{T^4}{1+C^2} & -CT+\dfrac{CT^3}{1+C^2} & CT-\dfrac{CT^3}{1+C^2} \\ -CT+\dfrac{CT^3}{1+C^2} & -T^2+\dfrac{C^2T^2}{1+C^2} & C^2-\dfrac{C^2T^2}{1+C^2} \\ CT-\dfrac{CT^3}{1+C^2} & C^2-\dfrac{C^2T^2}{1+C^2} & -T^2+\dfrac{C^2T^2}{1+C^2} \end{bmatrix}$	$\begin{bmatrix} -T^2-\dfrac{C^4}{1-T^2} & -TC-\dfrac{TC^3}{1-T^2} & TC+\dfrac{TC^3}{1-T^2} \\ -TC-\dfrac{TC^3}{1-T^2} & -C^2-\dfrac{T^2C^2}{1-T^2} & T^2+\dfrac{T^2C^2}{1-T^2} \\ TC+\dfrac{TC^3}{1-T^2} & T^2+\dfrac{T^2C^2}{1-T^2} & -C^2-\dfrac{T^2C^2}{1-T^2} \end{bmatrix}$
Optimal Z_c for Input Matching at Center Frequency	$Z_{C,b.M.B.}=\sqrt{\dfrac{2}{\left(1-k^2\right)}}kZ_0$	$Z_{C,m.M.B.}=\dfrac{k}{\sqrt{2\left(1-k^2\right)}}Z_0$

6.4 SUMMARY

This chapter has completely analyzed the basic Marchand balun and its

modification under a lossy condition in terms of a coupling factor and characteristic

impedance. Based on our theory and experiment outcomes, loss caused by a silicon substrate and metals does not deteriorate the operation of coupled-line-based baluns. Moreover, the optimal design in the characteristic impedance is provided here with respect to a corresponding coupling factor for the input-matching of the balun at the center frequency. Since high coupling results in high operation bandwidth, the improved Marchand balun has an advantage over the original type when both baluns are designed with the same characteristic impedance. Therefore, in this study, the modified Marchand balun has a better performance with the outputs of an 180±5° phase difference and a ±0.5-dB magnitude imbalance from 4 to 25 GHz. The fractional bandwidth is more than 140%. Finally, two wideband balun applications in a Gilbert micromixer are demonstrated using 0.35-μm SiGe BiCMOS technology. A 30% operation bandwidth enhancement of the mixer is attributed to the improvement of the Marchand balun.

Chapter 7 Conclusion

This research opens a new area for implementing microwave components on a lossy silicon substrate. From the RFIC era to the millimeter-wave regime, new design concepts for silicon ICs arise in devices like Schottky diode [85]-[87] and in passive components like Marchand baluns and rat-race couplers. Size reduction of the passives is achieved by high dielectric constant when transmission lines are formed directly on a lossy silicon substrate. A lossy transmission line is formed by absorbing the parasitic capacitance of an inductor, as shown in Fig. 7-1 and thus is not limited by the Q_{max} and f_{res}. In this dissertation, we completely analyze a planar Marchand balun, a modified Marchand balun, and a phase-inverter phase inverter under the lossy condition. These passive components are implemented directly on a standard low-resistivity (~10 Ω·cm) silicon substrate and merged into ICs for wideband applications. Integrating baluns or hybrids into the standard silicon IC overcomes the imbalance from the external balun and cables as well as reducing production cost due to the high integration. In addition, the optimal characteristic impedance is proposed in this dissertation for the first time, to the best of our knowledge, for perfect input matching of these lossy microwave components. The coupled-line coupling factor and optimal characteristic impedance are utilized in the wideband balun design, while the distortionless line concept is employed in the rat-race coupler design. Based on our theory and experiment outcomes, loss caused by a silicon substrate and metals does not deteriorate the operation of coupled-line-based baluns and phase-inverter rat-race couplers thanks to the symmetrical structure of the baluns and rat-race couplers.
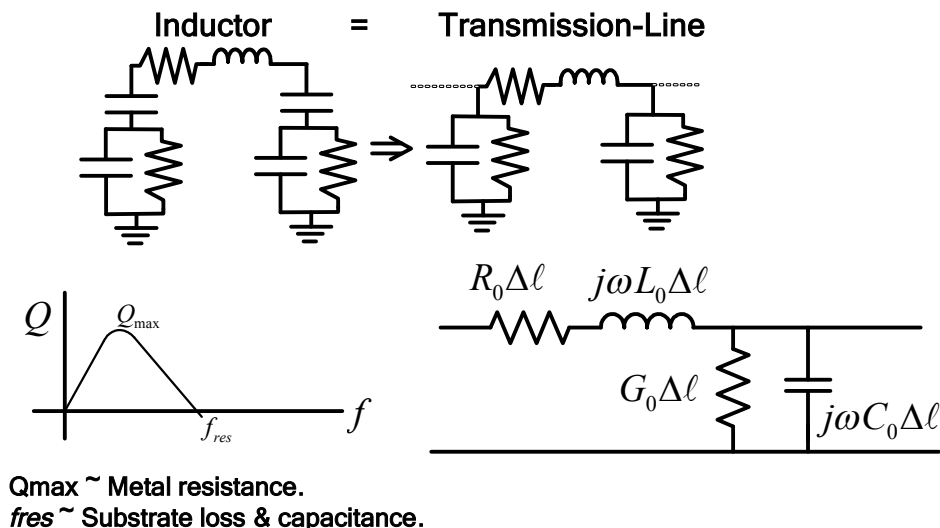
Fig. 7-1   From Inductors to Lossy Transmission Lines.

First, a single-ended wideband Gilbert mixer has been demonstrated using 0.35-μm SiGe BiCMOS technology. A systematic approach to measure the frequency response of the RF, IF, and LO stages of a Gilbert mixer has been developed. The developed frequency response measurement technique can be employed to identify the frequency-limiting mechanism.

Moreover, a reactive constant-resistance quadrature generator is proposed. The adjustable I/Q generator is in possession of quadrature phase property and constant input resistance at all frequencies. Dual band is achieved because the magnitude balance of the I/Q generator occurs at two designed frequencies. The 2.4/5.2 GHz I/Q down-converter and 2.4/5.7 GHz SSB up-converter implemented using 0.35-μm SiGe BiCMOS present the excellent quadrature performance of the dual-band adjustable I/Q generator. In comparison with the polyphase filter, there is no resistive loss in this generator and multiband quadrature mechanism is feasible by increasing the order of the L-C networks.

Since high coupling results in high operation bandwidth, the modified Marchand balun has an advantage over the original type when both baluns are designed with the

same characteristic impedance. Therefore, in this study, the modified Marchand balun has a better performance and its fractional bandwidth is more than 140%. This balun integrated into the Gilbert micromixer offers more than a 30% operation bandwidth than the conventional Marchand balun does.

In the comparison between wideband Marchand baluns and phase-inverter rat-race couplers, shown in TABLE 7.1, all implemented passive components function well on a standard lossy substrate, and the modified Marchand balun has the best performances in terms of bandwidth, size, and magnitude imbalance. Nevertheless, the rat-race coupler with four ports can achieve all-port matching as is compared with the other three-port elements. This rat-race coupler provides not only differential signals but also in-phase signals. Thanks to the high (~10) effective dielectric constant, the size of silicon-based passive components without shielding is compact.

TABLE 7.1 Comparison between Marchand Baluns and Phase-Inverter Rat-Race Couplers

Technology	0.18-μm 1P6M CMOS (Sec. 6.3.1)		0.35-μm 3P3M SiGe BiCMOS (Sec. 5.3.3)	0.35-μm 2P4M SiGe BiCMOS (Sec. 4.3.2)
Item	Basic Marchand Balun	Modified Marchand Balun	Lumped-Element Marchand Balun	Phase-Inverter Rat-Race Coupler
Frequency (GHz)	7 ~ 27	4.1 ~ 27	2.5 ~ 12	5 ~ 23
Ratio	1 : 3.9	1 : 6.6	1 : 4.8	1 : 4.6
Center Frequency (GHz)	17	15.6	7.2	14.5
Phase Error (°)	0 ~ -5	-3 ~ 7	3.5 ~ 7	-2 ~ -8.5
Magnitude Imbalance (dB)	< 1	< 0.5	< 1	< 1.6
Dissipated Loss (dB)	~2	~3	< 4	~5.5
Max S_{21} (dB)	-4.8	-5.8	-6.8	-7.96
Fractional Bandwidth (3-dB S_{21} Bandwidth) (%)	117.6	147.3	131	128
Chip Size (mm × mm)	0.17× 0.33	0.13 × 0.23	0.25 × 0.5	0.707 × 0.707
Design Parameters				
Metal Width (μm)	9	9	6	15
Line-to-Line Spacing (μm)	2	1	3	5
Metal Thickness (μm)	2.34	2.34 / 0.53	3.05	0.925
Metal-to-Substrate (μm)	8.15	6.62	4.54	6.155
Length (μm)	~ 1200	~ 1400	~ 1300	~ 1800

Because of the advanced transistors and successful passive component implementations, silicon technologies provide a new choice for millimeter-wave applications in the future, as shown in Fig. 7-2. The demonstrated passive components will be more useful at the millimeter-wave regime because of the size and loss reduction. They can be integrated with novel silicon-based Schottky diodes, proposed by K.K. O, to form a high-speed and high-performance passive mixer for millimeter-wave and microwave applications [85]. Further, the Schottky diodes can be implemented in low-cost silicon technologies and a low-cost solution is obtained for millimeter-wave and microwave transceivers.
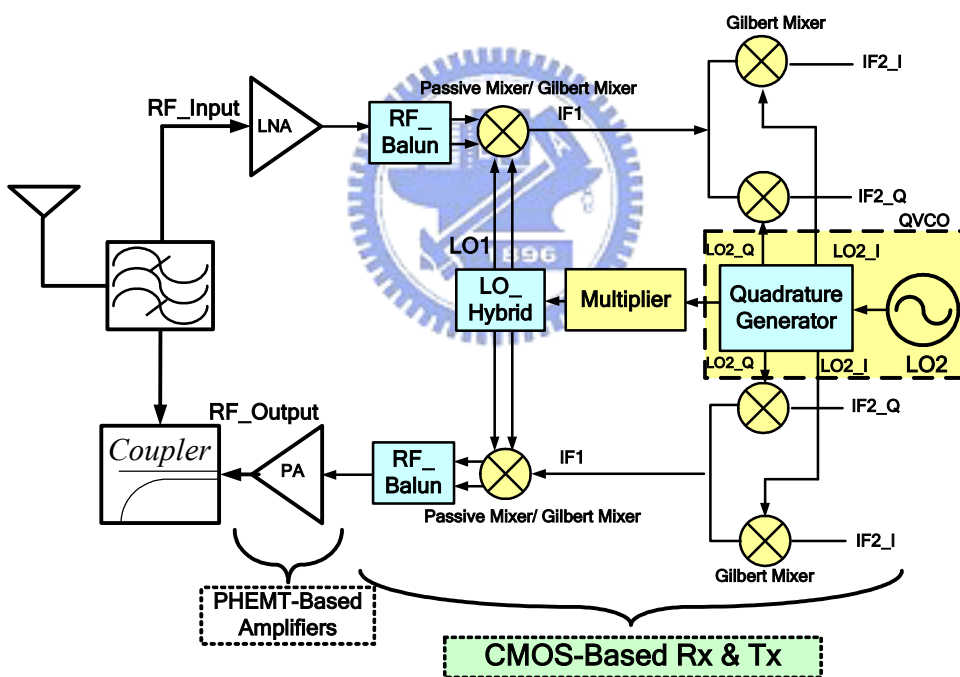
Fig. 7-2   Millimeter-wave and microwave silicon-based transceiver.

References

[1] K. R. Rao, J. Wilson, and M. Ismail, "A CMOS RF front-end for a multistandard WLAN receiver," *IEEE Microw. Wireless Compon. Lett.*, vol. 15, no. 5, pp. 321–323, May 2005.

[2] P. Heydari, "A study of low-power ultra wideband radio transceiver architectures," *IEEE Wireless Communications and Networking Conference*, vol. 2, pp. 758–763, Mar. 2005.

[3] A. Ghosh, D. R. Wolter, J. G. Andrews, and R. Chen, "Broadband wireless access with WiMAX/802.16: current performance benchmarks and future potential," *IEEE Commun. Mag.*, vol. 43, no. 2, pp. 129–136, Feb. 2005.

[4] C. H. Doan, S. Emami, A. M. Niknejad, and R. W. Brodersen, "Millimeter-wave CMOS design," *IEEE J. Solid-State Circuits*, vol. 40, no. 1, pp. 144–155, Jan. 2005.

[5] J. R. Long, "A low-voltage 5.1-5.8-GHz image-reject downconverter RF IC," *IEEE J. Solid-State Circuits*, vol. 35, no. 9, pp. 1320–1328, Sep. 2000.

[6] K. Masu, K. Okada, and H. Ito, "RF passive components using metal line on Si CMOS," *IEICE Trans. Electron.*, vol. E89-C, no. 6, pp. 681–691, Jun. 2006.

[7] T. S. D. Cheung and J. R. Long, "Shielded passive devices for silicon-based monolithic microwave and millimeter-wave integrated circuits," *IEEE J. Solid-State Circuits*, vol. 41, no. 5, pp. 1183–1200, May 2006.

[8] J. Y.-C. Chang, A. A. Abidi, and M. Gaitan, "Large suspended inductors on silicon and their use in a 2-μm CMOS RF amplifier," *IEEE Electron Device Lett.*, vol. 14, no. 5, pp. 246–248, May 1993.

[9] Jose M. Lopez-Villegas, Josep Samitier, Charles Cane, Pere Losantos, and Joan Bausells, "Improvement of the quality factor of RF integrated inductors by layout optimization," *IEEE Trans. Microw. Theory Tech.*, vol. 48, no. 1, pp. 76–83, Jan. 2000.

[10] T. Wang, H.-C. Chen, H.-W. Chiu, Y.-S. Lin, G. W. Huang, and S.-S. Lu, "Micromachined CMOS LNA and VCO by CMOS-compatible ICP deep trench technology," *IEEE Trans. Microw. Theory Tech.*, vol. 54, no. 2, pp. 580–588, Feb. 2006.

[11] Y. J. Yoon, Y. Lu, R. C. Frye, and P. R. Smith, "A silicon monolithic spiral transmission line balun with symmetrical design," *IEEE Electron Device Lett.*, vol. 20, no. 4, pp. 182–184, Apr. 1999.

[12] K. T. Chan, A. Chin, S. P. McAlister, C. Y. Chang, J. Liu, S. C. Chien, D. S. Duh, and W. J. Lin, "Low RF noise and power loss for ion-implanted Si having an improved implantation process," *IEEE Electron Device Lett.*, vol. 24, no. 1, pp. 28–30, Jan. 2003.

[13] K. T. Chan, C. H. Huang, A. Chin, M. F. Li, D.-L. Kwong, S. P. McAlister, D. S. Duh, and W. J. Lin, "Large Q-factor improvement for spiral inductors on silicon using proton implantation," *IEEE Microw. Wireless Compon. Lett.*, vol. 13, no. 11, pp. 460–462, Nov.

2003.

[14] C. P. Yue and S. S. Wong, "On-chip spiral inductors with patterned ground shields for Si-based RF ICs," *IEEE J. Solid-State Circuits*, vol. 33, no. 5, pp. 743–752, May 1998.

[15] B. Gilbert,, "The MICROMIXER: a highly linear variant of the Gilbert mixer using a bisymmetric Class-AB input stage," *IEEE J. Solid-State Circuits*, vol. 32, no. 9, pp. 1412–1423, Sep. 1997.

[16] E. M. Cherry and D. E. Hooper, "The design of wide-band transistor feedback amplifiers," *Proc. IEE*, vol. 110, no. 2, pp. 375–389, Feb. 1963.

[17] B. Razavi, *Design of Integrated Circuits for Optical Communications*, New York, NY: McGraw-Hill, 2003, ch. 5, sec. 5.2.3, pp. 136–140.

[18] C. C. Meng, T. H. Wu, T. H. Wu, and G. W. Huang, "A 5.2 GHz 16 dB gain CMFB Gilbert downconversion mixer using 0.35μm deep trench isolation SiGe BiCMOS technology," *in IEEE MTT-S Int. Microw. Symp. Dig.*, Fort Worth, TX, Jun. 2004, pp.975–978.

[19] A. S. Sedra and K. C. Smith, *Microelectronic Circuits*, 5th ed., New York, NY: Oxford University Press, 2004, pp. 637–638.

[20] S.-C. Tseng, C. C. Meng, C.-H. Chang, C.-K. Wu, and G.-W. Hung, "Broadband Gilbert micromixer with an LO Marchand balun and a TIA output buffer," *in IEEE MTT-S Int. Microw. Symp. Dig.*, San Francisco, CA, Jun. 2006, pp. 1509–1512.

[21] S.-C. Tseng, C. C. Meng, C.-H. Chang, C.-K. Wu, and G.-W. Huang, "Monolithic broadband Gilbert micromixer with an integrated Marchand balun using standard silicon IC process," *IEEE Trans. Microw. Theory Tech.*, vol. 54, no. 12, pp. 4362–4371, Dec. 2006.

[22] H. Hashemi and A. Hajimiri, "Concurrent multiband low-noise amplifiers-theory, design, and applications," *IEEE Trans. Microw. Theory Tech.*, vol. 50, no. 1, pp. 288–301, Jan. 2002.

[23] L. Sheng, J.C. Jensen and L.E. Larson, "A wide-bandwidth Si/SiGe HBT direct conversion sub-harmonic mixer/downconverter," *IEEE J. Solid-State Circuits*, vol. 35, no. 9, pp.1329–1337, Sep. 2000.

[24] K. Hettak, G. A. Morin, and M. G. Stubbs, "A novel miniature multilayer MMIC CPW single side band CPW mixer for up conversion at 44.5 GHz," *IEEE Microw. Wireless Compon. Lett.*, vol. 15, no. 9, pp. 606–608, Sep. 2005.

[25] J. C. Rundell, J.-J. Ou, T. B. Cho, G. Chien, F. Brianti, J. A. Weldon, and P. R. Gray, "A 1.9 GHz wide-band IF double conversion CMOS integrated receiver for cordless telephone applications," *IEEE J. Solid-State Circuits*, vol. 32, no. 12, pp. 2071–1088, Dec. 1997.

[26] F. Behbahani, Y. Kishigami, J. Leete, and A. A. Abidi, "CMOS mixers and polyphase filters for large image rejection," *IEEE J. Solid-State Circuits*, vol. 36, no. 6, pp.

873–887, Jun. 2001.

[27] D. I. Sanderson, R. M. Svitek, and S. Raman, "A 5-6-GHz polyphase filter with tunable I/Q phase balance," *IEEE Microw. Wireless Compon. Lett.*, vol. 14, no. 7, pp. 364–366, Jul. 2004.

[28] J. D. van der Tang, D. Kasperkovitz, and A. van Roermund, "A 9.8-11.5-GHz quadrature ring oscillator for optical receivers," *IEEE J. Solid-State Circuits*, vol. 37, no. 3, pp. 438-442, Mar. 2002.

[29] Z. Zhang, Z. Chen, L. Tsui and J. Lau, "A 930 MHz CMOS DC-offset-free direct-conversion 4-FSK receiver," in *IEEE Int. Solid-Stage Circuits Conf. Dig. Tech. Papers*, Feb. 2001, pp.290-291.

[30] A. A. Abidi, "Phase noise and jitter in CMOS ring oscillators," *IEEE J. Solid-State Circuits*, vol. 41, no. 8, pp. 1803–1816, Aug. 2006.

[31] F. Gruson, G. Gaborit, P. Abele, and H. Schumacher, "A broadband SiGe mixer for 5-GHz WLAN applications with X-band quadrature generation and high image-rejection," in *IEEE Radio Freq. Integrated Circuits Symp.*, Fort Worth, TX, Jun. 2004, pp. 523–526.

[32] C.-Y. Chi, and G. M. Rebeiz, "Design of Lange-couplers and single-sideband mixers using micromachining techniques," *IEEE Trans. Microw. Theory Tech.*, vol. 45, no. 2, pp. 291–294, Feb. 1997.

[33] R. C. Frye, S. Kapur, and R. C. Melville, "A 2-GHz quadrature hybrid implemented in CMOS technology," *IEEE J. Solid-State Circuits*, vol. 38, no. 3, pp. 550–555, Mar. 2003.

[34] H.-C. Chen, T. Wang, S.-S. Lu, and G.-W. Huang, "A monolithic 5.9-GHz CMOS I/Q direct-down converter utilizing a quadrature coupler and transformer-coupled subharmonic mixers," *IEEE Microw. Wireless Compon. Lett.*, vol. 16, no. 4, pp. 197–199, Apr. 2006.

[35] P. Andreani and X.Wang, "On the phase-noise and phase-error performances of multiphase LC CMOS VCOs," *IEEE J. Solid-State Circuits*, vol. 39, no. 11, pp. 1883–1893, Nov. 2004.

[36] P. Andreani, A. Bonfanti, L. Ramano, and C. Samori, "Analysis and design of a 1.8-GHz CMOS LC quadrature VCO," *IEEE J. Solid-State Circuits*, vol. 37, no. 12, pp. 1737–1747, Dec. 2002.

[37] S. L. J. Gierkink, S. Levantino, R. C. Frye, C. Samori, and V. Boccuzzi, "A low-phase-noise 5-GHz CMOS quadrature VCO using superharmonic coupling," *IEEE J. Solid-State Circuits*, vol. 38, no. 7, pp. 1148–1154, Jul. 2003.

[38] Y. Itoh, M. Nii, Y. Kohno, M. Mochizuki, and T. Takagi, "A 4 to 25 GHz 0.5 W monolithic lossy match amplifier," in *IEEE MTT-S Int. Microw. Symp. Dig.*, San Diego, CA, May 1994, pp. 257–260.

[39] C. C. Meng, S. K. Hsu, A. S. Peng, S. Y. Wen, and G. W. Huang, "A fully integrated 5.2 GHz GaInP/GaAs HBT upconversion micromixer with output LC current combiner and oscillator," in *IEEE MTT-S Int. Microw   Symp. Dig.*, Philadelphia , PA, Jun. 2003, pp. A205–A208.

[40] S.-C. Tseng, C. C. Meng, and Y.-T. Lee, "Dual-band adjustable and reactive I/Q generator with constant resistance for down- and up-converters," *IEEE Trans. Microw. Theory Tech.*, vol. 56, no. 8, pp. 1861–1868, Aug. 2008.

[41] J. Janssens and M. Steyaert, *CMOS Cellular Receiver Front-Ends*. Boston: Kluwer Academic Publishers, 2002, ch. 3, sec. 3.5.5, pp. 43–44.

[42] T. Wang and K. Wu, "Size-reduction and band-broadening design technique of uniplanar hybrid ring coupler using phase inverter for M(H)MIC's," *IEEE Trans. Microw. Theory Tech.*, vol. 47, no. 2, pp. 198–206, Feb. 1999.

[43] S. March, "A wideband stripline hybrid ring," *IEEE Trans. Microw. Theory Tech.*, vol. 16, no. 6, p. 361, Jun. 1968.

[44] M.-H. Murgulescu, E. Moisan, P. Legaud, E. Penard, and I. Zaquine, "New wideband, 0.67λg circumference 180° hybrid ring coupler," *Electron. Lett.*, vol. 30, no. 4, pp. 299–300, Feb. 1994.

[45] B. R. Heimer, L. Fan, and K. Chang, "Uniplanar hybrid couplers using asymmetrical coplanar striplines," *IEEE Trans. Microw. Theory Tech.*, vol. 45, no. 12, pp. 2234–2240, Dec. 1997.

[46] C.-Y. Chang and C.-C. Yang, "A novel broad-band Chebyshev-response rat-race ring coupler," *IEEE Trans. Microw. Theory Tech.*, vol. 47, no. 4, pp. 455–462, Apr. 1999.

[47] M. K. Chirala, and C. Nguyen, "Multilayer design techniques for extremely miniaturized CMOS microwave and millimeter-wave distributed passive circuits," *IEEE Trans. Microw. Theory Tech.*, vol. 54, no. 12, pp. 4218–4224, Dec. 2006.

[48] M.-J. Chiang, H.-S. Wu, and C.-K. C. Tzuang, "Design of synthetic quasi-TEM transmission Line for CMOS compact integrated circuit," *IEEE Trans. Microw. Theory Tech.*, vol. 55, no. 12, pp. 2512–2520, Dec. 2006.

[49] M. K. Chirala and B. A. Floyd, "Millimeter-wave Lange and ring hybrid couplers in a silicon technology for E-band applications," in *IEEE MTT-S Int. Microw. Symp. Dig.*, San Francisco, CA, Jun. 11–16, 2006, pp. 1547–1550.

[50] H.-Y. Chang, P.-S. Wu, T.-W. Huang, H. Wang, C.-L. Chang, and J. G. J. Chern, "Design and analysis of CMOS broad-band compact high-linearity modulators for gigabit microwave/millimeter-wave applications," *IEEE Trans. Microw. Theory Tech.*, vol. 54, no. 1, pp. 20–30, Jan. 2006.

[51] J. Reed and G. J. Wheeler, "A method of analysis of symmetrical four-port networks," *IEEE Trans. Microw. Theory Tech.*, vol. 4, no. 4, pp. 246–252, Oct. 1956.

[52] D. K. Cheng, *Field and Wave Electromagnetics*, 2nd ed. Reading, MA: Addison-Wesley,

1989, pp. 437-444.

[53] Y. Eo and W. R. Eisenstadt, "High-Speed VLSI Interconnect Modeling Based on *S*-Parameter Measurements," *IEEE Trans. Comp., Hybrids, Manufact. Technol,* vol. 16, no. 5, pp. 555–562, Aug. 1993.

[54] S.-C. Tseng, C. C. Meng, C.-H. Chang, S.-H. Chang and G.-W. Huang, "A silicon monolithic phase-inverter rat-race coupler using spiral coplanar striplines and its application in a broadband Gilbert mixer," *IEEE Trans. Microw. Theory Tech.*, vol. 56, no. 8, pp. 1879–1888, Aug. 2008.

[55] K. Ma, J.-G. Ma, L. Jia, B. Ong, M. A. Do, and K. S. Yeo, "800MHz~2.5GHz miniaturized multi-layer symmetrical stacked baluns for silicon based RF ICs," in *IEEE MTT-S Int. Microw. Symp.Dig.*, Long Beach , CA, Jun. 2005, pp. 283–286.

[56] W. R. Brinlee, A. M. Pavio, and K. R. Varian, "A novel planar double-balanced 6-18 GHz MMIC mixer," *in IEEE MTT-S Int. Microw. Symp. Dig.*, San Diego, CA, May 1994, pp. 9–12.

[57] S. A. Maas and Y. Ryu, "A broadband, planar, monolithic resistive frequency doubler," *in IEEE MTT-S Int. Microw. Symp. Dig.*, vol. 1, San Diego, CA, May 1994, pp. 443–446.

[58] N. Marchand, "Transmission-line conversion transformers," *Electronics*, vol. 17, no. 12, pp. 142–145, 1944.

[59] G. Oltman, "The compensated balun," *IEEE Trans. Microw. Theory Tech.*, vol. 14, no. 3, pp. 112–119, Mar. 1966.

[60] A. M. Pavio and A. Kikel, "A monolithic or hybrid broadband compensated balun," *in IEEE MTT-S Int. Microw. Symp. Dig.*, vol. 1, Dallas, TX, May 1990, pp. 483–486.

[61] T. Gokdemir, S. B. Economides, A. Khalid, A. A. Rezazadeh, and I.D. Robertson, "Design and performance of GaAs MMIC CPW baluns using overlaid and spiral couplers," *in IEEE MTT-S Int. Microw. Symp. Dig.*, Denver, CO, Jun. 1997, pp. 401–404.

[62] R. Mongia, I. Bahl, and P. Bhartia, *RF and Microwave Coupled-Line Circuits*, Norwood, MA: Artech House, 1999, pp. 411–438.

[63] K. S. Ang and I. D. Robertson, "Analysis and design of impedance-transforming planar Marchand baluns," *IEEE Trans. Microw. Theory Tech.*, vol. 49, no. 2, pp. 402–406, Feb. 2001.

[64] C. Nguyen and D. Smith, "Novel miniaturised wideband baluns for MIC and MMIC applications," *Electron. Lett.*, vol. 29, no. 12, pp. 1060–1061, Jun. 1993.

[65] M. C. Tsai, "A new compact wideband balun," *in IEEE MTT-S Int. Microw. Symp. Dig.*, vol. 1, Atlanta, GA, Jun. 1993, pp. 141–143.

[66] T.-H Chen, K. W. Chang, S. B. Bui, H. Wang, G. S. Dow, L. C. T. Liu, T. S. Lin, and W. S. Titus, "Broadband monolithic passive baluns and monolithic double-balanced mixer,"

IEEE Trans. Microw. Theory Tech., vol. 39, no. 12, pp. 1980–1986, Dec. 1991.

[67] K. Nishikawa, I. Toyoda, and T. Tokumitsu, "Compact and broad-band three-dimensional MMIC balun," *IEEE Trans. Microw. Theory Tech.*, vol. 47, no. 1, pp. 96–98, Jan. 1999.

[68] Y. J. Yoon, Y. Lu; R. C. Frye, and P. R. Smith, "A silicon monolithic spiral transmission line balun with symmetrical design," *IEEE Electron Device Lett.*, vol. 20, no. 4, pp. 182–184, Apr. 1999.

[69] K. S. Ang, S. B. Economides, S. Nam, and I. D. Robertson, "A compact MMIC balun using spiral transformers," *in Asia Pacific Microwave Conference*, Singapore, Nov. 1999, pp. 655–658.

[70] M. Shimozawa, K. Itoh, Y. Sasaki, H. Kawano, Y. Isota, and O. Ishida, "A parallel connected Marchand balun using spiral shaped equal length coupled lines," *in IEEE MTT-S Int. Microw. Symp. Dig.*, Anaheim, CA, Jun. 1999, pp. 1737–1740.

[71] Y. J. Yoon, Y. Lu, R. C. Frye, M. Y. Lau, P. R. Smith, L. Ahlquist, and D. P. Kossives, "Design and characterization of multilayer spiral transmission-line baluns," *IEEE Trans. Microw. Theory Tech.*, vol. 47, no. 9, pp. 1841–1847, Sep. 1999.

[72] K. S. Ang, Y. C. Leong, and C. H. Lee, "Analysis and design of miniaturized lumped-distributed impedance-transforming baluns," *IEEE Trans. Microw. Theory Tech.*, vol. 51, no. 3, pp. 1009–1017, Mar. 2003.

[73] C. W. Tang and C. Y. Chang, "A semi-lumped balun fabricated by low temperature co-fired ceramic," *in IEEE MTT-S Int. Microw. Symp. Dig.*, Seattle, WA, Jun. 2002, pp. 2201–2204.

[74] K. W. Hamed, A. P. Freundorfer, and Y. M. M. Antar, "A monolithic double-balanced direct conversion mixer with an integrated wideband passive balun," *IEEE J. Solid-State Circuits*, vol. 40, no. 3, pp. 622–629, Mar. 2005.

[75] H.-J. Wei, C. C. Meng, P.-Y. Wu, and K.-C. Tsung, "K-band CMOS sub-harmonic resistive mixer with a miniature Marchand balun on lossy silicon substrate," *IEEE Trans. Microw. Wireless Compon. Lett.*, vol. 18, no. 1, pp. 40–42, Jan. 2008.

[76] H.-K. Chiou and T.-Y. Yang "Low-loss and broadband asymmetric broadside-coupled balun for mixer design in 0.18-μm CMOS technology," *IEEE Trans. Microw. Theory Tech.*, vol. 56, no. 4, pp. 835–848, Apr. 2008.

[77] C.-S. Lin, P.-S. Wu, M.-C. Yeh, J.-S. Fu, H.-Y. Chang, K.-Y. Lin and H. Wang, "Analysis of multiconductor coupled-line Marchand baluns for miniature MMIC design," *IEEE Trans. Microw. Theory Tech.*, vol. 55, no. 6, pp. 1190–1199, Jun. 2007.

[78] R. Schwindt and C. Nguyen, "Computer-aided analysis and design of a planar multilayer Marchand balun," *IEEE Trans. Microw. Theory Tech.*, vol. 42, no. 7, pp. 1429–1434, Jul.. 1994.

[79] J.-W. Lee and K.J. Webb, "Analysis and design of low-loss planar microwave baluns

having three symmetric coupled lines," *in IEEE MTT-S Int. Microw. Symp. Dig.*, Seattle, WA, Jun. 2002, pp. 117–120.

[80] Y. C. Leong, K. S. Ang, and C. H. Lee, "A derivation of a class of 3-port baluns from symmetrical 4-port networks," *in IEEE MTT-S Int. Microw. Symp. Dig.*, Seattle, WA, Jun. 2002, pp. 1165–1168.

[81] K.S. Ang, Y.C. Leong, and C.H. Lee, "Multisection impedance-transforming coupled-line baluns," *IEEE Trans. Microw. Theory Tech.*, vol. 51, no. 2, pp. 536–541, Feb. 2003.

[82] L.G. Maloratsky, *Passive RF & Microwave Integrated Circuits*, Burlington, MA: Newnes, 2004, pp.140–149.

[83] D. M. Pozar, *Microwave Engineering*, 3rd ed., USA: John Wiley & Sons, 2005, pp. 275–276.

[84] J. R. Long, "Monolithic transformers for silicon RF IC design," *IEEE J. Solid-State Circuits*, vol. 35, no. 9, pp. 1368–1382, Sep. 2000.

[85] S. Sankaran and K. K. O, "A ultra-wideband amplitude modulation (AM) detector using Schottky barrier diodes fabricated in foundry CMOS technology," *IEEE J. of Solid-State Circuits*, vol. 42, no. 5, pp. 1058-1064, May 2007.

[86] S. Sankaran and K. K. O, "Schottky barrier diodes for millimeter wave detection in a foundry CMOS process," *IEEE Electron Device Letters*, vol. 26, no. 7, pp. 492-494, July 2005.

[87] S. Sankaran and K. K. O, "Schottky diode with cutoff frequency of 400 GHz fabricated in 0.18 um CMOS," *Electronics Letters*, Vol. 41, No. 8, April 2005.

[88] R. Mongia, I. Bahl, and P. Bhartia, *RF and Microwave Coupled-Line Circuits*, Norwood, MA: Artech House, 1999, pp. 136–139.

[89] D. M. Pozar, *Microwave Engineering*, 3rd ed., USA: John Wiley & Sons, 2005, pp. 416–420.

Appendix A   Derivation of S_{21}=-S_{41} in the Phase-Inverter Rat-Race Coupler

The complex scattering parameters of the coupler are written in (4.5). Under the condition of $\ell_a = 2\ell_b = \ell$, $\hat{z}_a = \hat{z}_b = \hat{z}$, and $\gamma_a = \gamma_b = \gamma$, the numerator of S_{21} is simplified to

$$\frac{\hat{z}_a}{\hat{z}_b}\sinh(\gamma_a\ell_a)\left[\tanh(\gamma_b\ell_b) - \coth(\gamma_b\ell_b)\right]$$

$$= \sinh(\gamma\ell)\left[\tanh\left(\frac{\gamma\ell}{2}\right) - \coth\left(\frac{\gamma\ell}{2}\right)\right]$$

$$= \sinh(\gamma\ell)\left[\frac{\sinh^2\left(\frac{\gamma\ell}{2}\right) - \cosh^2\left(\frac{\gamma\ell}{2}\right)}{\sinh\left(\frac{\gamma\ell}{2}\right)\cosh\left(\frac{\gamma\ell}{2}\right)}\right] \qquad (A.1)$$

$$= \sinh(\gamma\ell)\left[-2\operatorname{csch}(\gamma\ell)\right]$$

$$= -2$$

where

$$\sinh^2\left(\frac{\gamma\ell}{2}\right) - \cosh^2\left(\frac{\gamma\ell}{2}\right) = -1 \qquad (A.2)$$

and

$$\sinh\left(\frac{\gamma\ell}{2}\right)\cosh\left(\frac{\gamma\ell}{2}\right) = \frac{1}{2}\sinh(\gamma\ell). \qquad (A.3)$$

Therefore, S_{21} is equal to -S_{41}.

Appendix B   Derivation of the Normalized Characteristic Impedance and S_{21} of the CPSs for the Perfect Port-Matching

At the center frequency, the numerator of S_{11} can be derived in terms of $\ell_a = 2\ell_b = \ell = \lambda/4$, $\hat{z}_a = \hat{z}_b = \hat{z}$, and $\gamma_a = \gamma_b = \gamma$,

$$\sinh\left(\gamma_a \ell_a\right)\left(\hat{z}_a - \frac{1}{\hat{z}_a} - \frac{\hat{z}_a}{\hat{z}_b^2}\right) - \frac{1}{\hat{z}_b}\cosh\left(\gamma_a \ell_a\right)\left[\tanh\left(\gamma_b \ell_b\right) + \coth\left(\gamma_b \ell_b\right)\right]$$

$$= j\cosh\left(\frac{\lambda}{4}\alpha\right)\left(\hat{z} - \frac{2}{\hat{z}}\right) - j\frac{2}{\hat{z}}\sinh\left(\frac{\lambda}{4}\alpha\right)\tanh\left(\frac{\lambda}{4}\alpha\right)$$

$$= j\frac{\hat{z}^2\cosh^2\left(\frac{\lambda}{4}\alpha\right) - 2\left[\cosh^2\left(\frac{\lambda}{4}\alpha\right) + \sinh^2\left(\frac{\lambda}{4}\alpha\right)\right]}{\hat{z}\cosh\left(\frac{\lambda}{4}\alpha\right)} \qquad (B.1)$$

$$= \frac{j}{\hat{z}\cosh\left(\frac{\lambda}{4}\alpha\right)}\left\{\hat{z}^2\cosh^2\left(\frac{\lambda}{4}\alpha\right) - 2\cosh\left(\frac{\lambda}{2}\alpha\right)\right\}$$

where

$$\begin{cases} \sinh\left(\frac{\lambda}{4}\gamma\right) = \sinh\left(\frac{\lambda}{4}\alpha + j\frac{\pi}{2}\right) = j\cosh\left(\frac{\lambda}{4}\alpha\right) \\ \cosh\left(\frac{\lambda}{4}\gamma\right) = \cosh(\frac{\lambda}{4}\alpha + j\frac{\pi}{2}) = j\sinh\left(\frac{\lambda}{4}\alpha\right) \\ \tanh\left(\frac{\lambda}{8}\gamma\right) + \coth\left(\frac{\lambda}{8}\gamma\right) = 2\tanh\left(\frac{\lambda}{4}\alpha\right) \\ \cosh^2\left(\frac{\lambda}{4}\alpha\right) + \sinh^2\left(\frac{\lambda}{4}\alpha\right) = \cosh\left(\frac{\lambda}{2}\alpha\right) \end{cases} . \qquad (B.2)$$

When

$$\hat{z} = \frac{\sqrt{2\cosh\left(\frac{\lambda\alpha}{2}\right)}}{\cosh\left(\frac{\lambda\alpha}{4}\right)} \qquad (B.3)$$

this numerator is equal to zero and the port matching of the coupler is achieved at the center frequency. Under the matching condition, S_{21} at the center frequency can be

obtained as

$$S_{21} = -\frac{2}{D}$$

$$= -20\log\left[2\sinh\left(\frac{\lambda\alpha}{4}\right) + \sqrt{2\cosh\left(\frac{\lambda\alpha}{2}\right)} \right] \quad (\text{dB})$$

(B.4)

where

$$D = 2\cosh\left(\gamma_a \ell_a\right) + \frac{1}{\hat{z}_b}\left[\hat{z}_a \sinh\left(\gamma_a \ell_a\right) + \cosh\left(\gamma_a \ell_a\right)\right]\left[\tanh\left(\gamma_b \ell_b\right) + \coth\left(\gamma_b \ell_b\right)\right]$$

$$+ \sinh\left(\gamma_a \ell_a\right)\left(\hat{z}_a + \frac{1}{\hat{z}_a} + \frac{\hat{z}_a}{\hat{z}_b^2}\right)$$

$$= j2\sinh\left(\frac{\alpha\lambda}{4}\right) + \frac{1}{\hat{z}}\left[\hat{z}j\cosh\left(\frac{\alpha\lambda}{4}\right) + j\sinh\left(\frac{\alpha\lambda}{4}\right)\right]\left[2\tanh\left(\frac{\alpha\lambda}{4}\right)\right] + j\cosh\left(\frac{\alpha\lambda}{4}\right)\left(\hat{z} + \frac{2}{\hat{z}}\right)$$

$$= j4\sinh\left(\frac{\alpha\lambda}{4}\right) + \frac{j2\sinh^2\left(\frac{\alpha\lambda}{4}\right) + j2\cosh^2\left(\frac{\alpha\lambda}{4}\right)}{\sqrt{2\cosh\left(\frac{\alpha\lambda}{2}\right)}} + j\sqrt{2\cosh\left(\frac{\alpha\lambda}{2}\right)}$$

$$= j4\sinh\left(\frac{\alpha\lambda}{4}\right) + j2\sqrt{2\cosh\left(\frac{\alpha\lambda}{2}\right)}$$

(B.5)
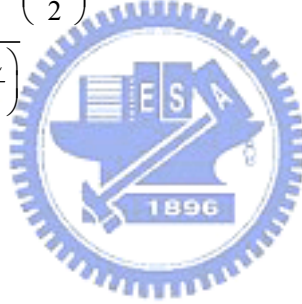
Appendix C   *S*-Parameter Derivation of a Lossy Coupled Line

Coupled lines are the main components used to form a basic Marchand balun and a modified Marchand balun in Chapter 5 and Chapter 6. The even- and odd-mode *ABCD* matrix method is employed to analyze the lossy coupled line, as shown in Fig. C-1. Half of the coupled line can be considered as a lossy transmission line. Then, the even- and odd-mode *ABCD* matrices are denoted as

$$\begin{bmatrix} A & B \\ C & D \end{bmatrix}_e = \begin{bmatrix} \cosh(\gamma\ell) & \hat{Z}_{0e}\sinh(\gamma\ell) \\ \hat{Y}_{0e}\sinh(\gamma\ell) & \cosh(\gamma\ell) \end{bmatrix} \tag{C.1}$$

and

$$\begin{bmatrix} A & B \\ C & D \end{bmatrix}_o = \begin{bmatrix} \cosh(\gamma\ell) & \hat{Z}_{0o}\sinh(\gamma\ell) \\ \hat{Y}_{0o}\sinh(\gamma\ell) & \cosh(\gamma\ell) \end{bmatrix}, \tag{C.2}$$

respectively.
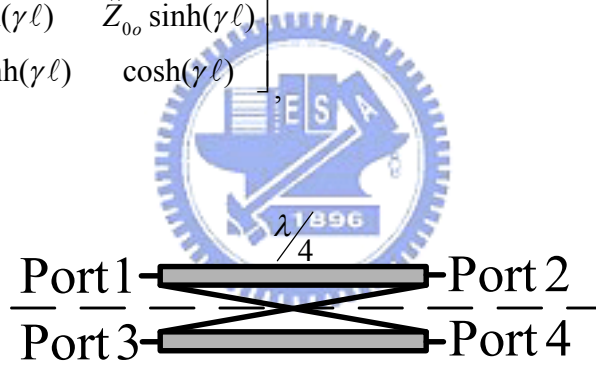
Fig. C-1   Four-port network of the coupled line.
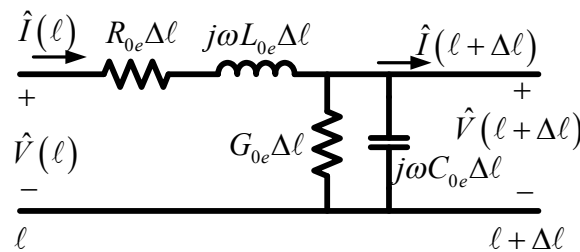
Fig. C-2   Electric circuit model of a transmission line for the even mode

A lossy transmission line for the even mode is shown in Fig. C-2 and the even-mode characteristic impedance is expressed as

$$\hat{Z}_{0e} = \sqrt{(R_{0e} + j\omega L_{0e}) \Big/ (G_{0e} + j\omega C_{0e})} \tag{C.3}$$

with the per-unit-length resistance R_{0e}, inductance L_{0e}, conductance G_{0e}, and capacitance C_{0e}, [52]. $\hat{Z}_{0o}$ is the odd-mode characteristic impedance and can be defined similarly to $\hat{Z}_{0e}$ with its associated R, L, G, and C. The even- and odd-mode propagation constants are assumed to be equal for simplicity and are defined as γ [88]. In other words, $\hat{Z}_{0e}$ and $\hat{Z}_{0o}$ are complex numbers for the lossy transmission line. The coupled line length is ℓ. Then, the even- and odd-mode S-parameters of the lossy coupled line are obtained as follows:

$$S_{11,C}^{e} = \frac{\left(\dfrac{\hat{Z}_{0e}}{Z_0} - \dfrac{Z_0}{\hat{Z}_{0e}}\right)\sinh(\gamma\ell)}{2\cosh(\gamma\ell) + \left(\dfrac{\hat{Z}_{0e}}{Z_0} + \dfrac{Z_0}{\hat{Z}_{0e}}\right)\sinh(\gamma\ell)}, \tag{C.4}$$

$$S_{21,C}^{e} = \frac{2}{2\cosh(\gamma\ell) + \left(\dfrac{\hat{Z}_{0e}}{Z_0} + \dfrac{Z_0}{\hat{Z}_{0e}}\right)\sinh(\gamma\ell)}, \tag{C.5}$$

$$S_{11,C}^{o} = \frac{\left(\dfrac{\hat{Z}_{0o}}{Z_0} - \dfrac{Z_0}{\hat{Z}_{0o}}\right)\sinh(\gamma\ell)}{2\cosh(\gamma\ell) + \left(\dfrac{\hat{Z}_{0o}}{Z_0} + \dfrac{Z_0}{\hat{Z}_{0o}}\right)\sinh(\gamma\ell)}, \tag{C.6}$$

and

$$S_{21,C}^{o} = \frac{2}{2\cosh(\gamma\ell) + \left(\dfrac{\hat{Z}_{0o}}{Z_0} + \dfrac{Z_0}{\hat{Z}_{0o}}\right)\sinh(\gamma\ell)}, \tag{C.7}$$

where Z_0 is terminal impedance. Finally, the scattering parameter matrix of the lossy coupled line is written as

$$[S]_{C.L.} = \begin{bmatrix} R & I & C & T \\ I & R & T & C \\ C & T & R & I \\ T & C & I & R \end{bmatrix}$$

$$= \frac{1}{2} \begin{bmatrix} S_{11,C}^e + S_{11,C}^o & S_{21,C}^e - S_{21,C}^o & S_{11,C}^e - S_{11,C}^o & S_{21,C}^e + S_{21,C}^o \\ S_{21,C}^e - S_{21,C}^o & S_{11,C}^e + S_{11,C}^o & S_{21,C}^e + S_{21,C}^o & S_{11,C}^e - S_{11,C}^o \\ S_{11,C}^e - S_{11,C}^o & S_{21,C}^e + S_{21,C}^o & S_{11,C}^e + S_{11,C}^o & S_{21,C}^e - S_{21,C}^o \\ S_{21,C}^e + S_{21,C}^o & S_{11,C}^e - S_{11,C}^o & S_{21,C}^e - S_{21,C}^o & S_{11,C}^e + S_{11,C}^o \end{bmatrix}$$

(C.8)

R, I, C, and T stand for the reflection, isolation, coupling, and through coefficients of the coupled line, respectively.

Under the matching condition of $\hat{Z}_{0e}\hat{Z}_{0o} = Z_0^2$, the coupled line has perfect matching and excellent isolation. Therefore, the scattering parameters for the coupled and transmitted ports C and T are

$$C = \frac{\left(\dfrac{\hat{Z}_{0e}}{Z_0} - \dfrac{Z_0}{\hat{Z}_{0e}} \right)\sinh(\gamma\ell)}{2\cosh(\gamma\ell) + \left(\dfrac{\hat{Z}_{0e}}{Z_0} + \dfrac{Z_0}{\hat{Z}_{0e}} \right)\sinh(\gamma\ell)}$$

(C.9)

and

$$T = \frac{2}{2\cosh(\gamma\ell) + \left(\dfrac{\hat{Z}_{0e}}{Z_0} + \dfrac{Z_0}{\hat{Z}_{0e}} \right)\sinh(\gamma\ell)},$$

(C.10)

respectively [88]. The Marchand balun analysis in Section 5.2 is developed based on these scattering parameters. As shown in (C.3), the lossy characteristic impedances $\hat{Z}_{0e}$ and $\hat{Z}_{0o}$ vary with frequencies in the presence of loss and the coupled line is dispersive. In our analysis of the Marchand balun formula on a standard lossy silicon substrate in Section 5.2, the values of C and T can be substituted by (C.9) and (C.10). The matching condition of $\hat{Z}_{0e}\hat{Z}_{0o} = Z_0^2$ is designed at the center frequency. Thus, the heuristic analysis, as shown in Fig. 5-2 and Fig. 5-3, is valid at the center frequency for a Marchand balun on a lossy substrate. Under the lossless condition, the complex

characteristic impedances $\hat{Z}_{0e}$ and $\hat{Z}_{0o}$ become real numbers Z_{0e} and Z_{0o}, respectively. The matching condition can be designed for all frequencies and, thus, the analysis in Fig. 5-2 and Fig. 5-3 is valid for all frequencies. At the frequency where $\beta l = \pi/2$, (C.9) and (C.10) become well-known formulas as

$$C = k \tag{C.11}$$

and

$$T = -j\sqrt{1-k^2} \tag{C.12}$$

where the coupling factor k is equal to

$$k = \frac{Z_{0e} - Z_{0o}}{Z_{0e} + Z_{0o}}. \tag{C.13}$$

Appendix D   Derivation of the Even-Mode Transmission Coefficient of the Baluns

Obviously, the even-mode transmission coefficients, S_{21}^e, of the basic Marchand balun and its modification are the same, as shown in Fig. 6-2(a) and (b). This is a kind of all-stop coupled-line filter [89]. According to the coupled-line S-matrix in (C.8) and the even-mode analysis of the balun, the transmission coefficient is expressed as

$$S_{21}^e = I + \frac{I(C^2 + T^2) - 2RCT}{R^2 - I^2 - 1}.$$
(D.1)

Substituting (C.4)–(C.8) in (D.1), the numerator of S_{21}^e is derived as

$$
\begin{aligned}
&= -4\left(\frac{S_{11,C}^e}{2}\right)^2 \frac{S_{21,C}^o}{2} + 4\left(\frac{S_{11,C}^o}{2}\right)^2 \frac{S_{21,C}^e}{2} + 4\left(\frac{S_{21,C}^e}{2}\right)^2 \frac{S_{21,C}^o}{2} - 4\left(\frac{S_{21,C}^o}{2}\right)^2 \frac{S_{21,C}^e}{2} - \frac{S_{21,C}^e}{2} + \frac{S_{21,C}^o}{2} \\
&= \sinh^3(\gamma\ell)\left[\left(y - \frac{1}{y}\right)^2\left(x + \frac{1}{x}\right) - \left(x - \frac{1}{x}\right)^2\left(y + \frac{1}{y}\right)\right] \\
&\quad + \sinh^3(\gamma\ell)\left[\left(y + \frac{1}{y}\right)\left(x + \frac{1}{x}\right)^2 - \left(x + \frac{1}{x}\right)\left(y + \frac{1}{y}\right)^2\right] \\
&\quad + 4\sinh(\gamma\ell)\left[\left(y + \frac{1}{y}\right) - \left(x + \frac{1}{x}\right)\right] + 4\sinh(\gamma\ell)\cosh^2(\gamma\ell)\left[\left(x + \frac{1}{x}\right) - \left(y + \frac{1}{y}\right)\right] \\
&= \sinh^3(\gamma\ell)\left[-4\left(x + \frac{1}{x}\right) + 4\left(y + \frac{1}{y}\right)\right] + 4\sinh(\gamma\ell)\left[\left(y + \frac{1}{y}\right) - \left(x + \frac{1}{x}\right)\right] \\
&\quad + 4\sinh(\gamma\ell)\left[1 + \sinh^2(\gamma\ell)\right]\left[\left(x + \frac{1}{x}\right) - \left(y + \frac{1}{y}\right)\right] \\
&= 0
\end{aligned}
$$
(D.2)

with $x = \widehat{Z}_{0e}/Z_0$ and $y = \widehat{Z}_{0o}/Z_0$. Therefore, $S_{21}^e = 0$ no matter what the frequency is, and the original Marchand balun and the reformation have truly differential outputs, based on (6.2)–(6.6).

Appendix E   Input Matching Criteria for the Basic and Modified Marchand Baluns in the Lossless Case

From (C.4)–(C.8)

$$[S]_{C.L.} = \begin{bmatrix} R & I & C & T \\ I & R & T & C \\ C & T & R & I \\ T & C & I & R \end{bmatrix}$$

$$= \frac{1}{2} \begin{bmatrix} S_{11,C}^e + S_{11,C}^o & S_{21,C}^e - S_{21,C}^o & S_{11,C}^e - S_{11,C}^o & S_{21,C}^e + S_{21,C}^o \\ S_{21,C}^e - S_{21,C}^o & S_{11,C}^e + S_{11,C}^o & S_{21,C}^e + S_{21,C}^o & S_{11,C}^e - S_{11,C}^o \\ S_{11,C}^e - S_{11,C}^o & S_{21,C}^e + S_{21,C}^o & S_{11,C}^e + S_{11,C}^o & S_{21,C}^e - S_{21,C}^o \\ S_{21,C}^e + S_{21,C}^o & S_{11,C}^e - S_{11,C}^o & S_{21,C}^e - S_{21,C}^o & S_{11,C}^e + S_{11,C}^o \end{bmatrix}$$

(C.8), at the center frequency, $\ell = \lambda/4$ and R, I, C, and T are written as

$$R = \frac{\left[Z_C^4 - Z_0^4\right]\left(1 - k^2\right)}{D}$$

$$I = \frac{-2\left[Z_C^2 - Z_0^2\right]Z_C Z_0 k\sqrt{1-k^2}}{jD}$$

$$C = \frac{4Z_C^2 Z_0^2 k}{D}$$

(E.1)

$$T = \frac{2\left[Z_C^2 + Z_0^2\right]Z_C Z_0 \sqrt{1-k^2}}{jD}$$

with $D = \left[Z_C^4 + Z_0^4\right]\left(1-k^2\right) + Z_C^2 Z_0^2 2\left(1+k^2\right)$ and the coupling factor, $k = \left(Z_{0e} - Z_{0o}\right)/\left(Z_{0e} + Z_{0o}\right)$. The coupled-line characteristic impedance Z_C and its even-/odd-mode impedance, Z_{0e} and Z_{0o}, are real in the case of lossless. We can obtain

$$RC = \frac{4\left[Z_C^4 - Z_0^4\right]Z_C^2 Z_0^2 k\left(1-k^2\right)}{D^2} = IT,$$

(E.2)

thanks to the principle of the power conservation of the coupled-line even and odd modes, $\left(S_{11,C}^e\right)^2 - \left(S_{21,C}^e\right)^2 = \left(S_{11,C}^o\right)^2 - \left(S_{21,C}^o\right)^2 = 1$, and

---

$$R^2 - I^2 - T^2 + C^2 = 1, \tag{E.3}$$

because of the principle of the power conservation of the coupled line. According to (6.2), (E.2), and (E.3), $S^e_{11,m.M.B.}$ and $S^e_{11,b.M.B.}$ are always equal 1 and -1, respectively.

For solving $S^o_{11,m.M.B.} = -1/3$, we find

$$4R^2 - C^2 - 2T^2 - I^2 + 4R = 0, \tag{E.4}$$

and then

$$\left[2Z_C^2\left(1-k^2\right) - Z_0^2 k^2\right] \times \left[Z_C^2\left(1-k\right) + Z_0^2\left(1+k\right)\right] \times \left[Z_C^2\left(1+k\right) + Z_0^2\left(1-k\right)\right] = 0. \tag{E.5}$$

Therefore, the optimal characteristic impedance of the coupled line for the modified Marchand balun is decided as

$$Z_{C,m.M.B.} = \frac{k}{\sqrt{2\left(1-k^2\right)}} Z_0 \tag{E.6}$$

in terms of the coupling factor k and the terminal impedance Z_0. For $S^o_{11,b.M.B.} = 1/3$, we get

$$2R^2 - 2C^2 - T^2 + I^2 + 2R = 0, \tag{E.7}$$

and then

$$\left[Z_C^2\left(1-k^2\right) - Z_0^2 2k^2\right] \times \left[Z_C^2\left(1-k\right) + Z_0^2\left(1+k\right)\right] \times \left[Z_C^2\left(1+k\right) + Z_0^2\left(1-k\right)\right] = 0. \tag{E.8}$$

Therefore, the characteristic impedance is designed as

$$Z_{C,b.M.B.} = \sqrt{\frac{2}{\left(1-k^2\right)}} k Z_0 \tag{E.9}$$

for the input-matching of the basic Marchand balun at the center frequency.

Appendix F   Mathematics

$$\begin{bmatrix} V_1 \\ I_1 \end{bmatrix} = \begin{bmatrix} A & B \\ C & D \end{bmatrix} \begin{bmatrix} V_2 \\ -I_2 \end{bmatrix}$$

$$\begin{bmatrix} b_1 \\ b_2 \end{bmatrix} = \begin{bmatrix} S_{11} & S_{12} \\ S_{21} & S_{22} \end{bmatrix} \begin{bmatrix} a_1 \\ a_2 \end{bmatrix}$$

$$\begin{bmatrix} S_{11} & S_{12} \\ S_{21} & S_{22} \end{bmatrix} = \begin{bmatrix} \dfrac{AZ_2 + B - CZ_1Z_2 - DZ_1}{AZ_2 + B + CZ_1Z_2 + DZ_1} & \dfrac{2(AD-BC)\sqrt{Z_1Z_2}}{AZ_2 + B + CZ_1Z_2 + DZ_1} \\ \dfrac{2\sqrt{Z_1Z_2}}{AZ_2 + B + CZ_1Z_2 + DZ_1} & \dfrac{-AZ_2 + B - CZ_1Z_2 + DZ_1}{AZ_2 + B + CZ_1Z_2 + DZ_1} \end{bmatrix}$$

$$= \begin{bmatrix} \dfrac{A + BY_0 - CZ_0 - D}{A + BY_0 + CZ_0 + D} & \dfrac{2(AD-BC)}{A + BY_0 + CZ_0 + D} \\ \dfrac{2}{A + BY_0 + CZ_0 + D} & \dfrac{-A + BY_0 - CZ_0 + D}{A + BY_0 + CZ_0 + D} \end{bmatrix}$$

$$\sinh(\frac{\lambda}{4}\alpha + j\frac{\pi}{2}) = j\cosh(\frac{\lambda}{4}\alpha)$$

$$\cosh(\frac{\lambda}{4}\alpha + j\frac{\pi}{2}) = j\sinh(\frac{\lambda}{4}\alpha)$$

$$\tanh(\frac{\lambda}{4}\alpha + j\frac{\pi}{2}) = \coth(\frac{\lambda}{4}\alpha)$$

$$\coth(\frac{\lambda}{4}\alpha + j\frac{\pi}{2}) = \tanh(\frac{\lambda}{4}\alpha)$$

$$\coth(\frac{\lambda}{8}\gamma) = \coth(\frac{1}{2}\times\frac{\lambda}{4}\gamma) = \frac{\sinh(\frac{\lambda}{4}\alpha) - j\sin(\frac{\pi}{2})}{\cosh(\frac{\lambda}{4}\alpha) - \cos(\frac{\pi}{2})}$$

$$\tanh(\frac{\lambda}{8}\gamma) = \tanh(\frac{1}{2}\times\frac{\lambda}{4}\gamma) = \frac{\sinh(\frac{\lambda}{4}\alpha) + j\sin(\frac{\pi}{2})}{\cosh(\frac{\lambda}{4}\alpha) + \cos(\frac{\pi}{2})}$$

$$\tanh(\frac{\lambda}{8}\gamma) + \coth(\frac{\lambda}{8}\gamma) = 2\tanh(\frac{\lambda}{4}\alpha)$$

$$\coth(\frac{\lambda}{8}\gamma) - \tanh(\frac{\lambda}{8}\gamma) = \frac{-2j}{\cosh(\frac{\lambda}{4}\alpha)}$$

$z = x + iy$

$$\sinh(z) \equiv \frac{e^z - e^{-z}}{2} = -\sinh(-z)$$

$$\cosh(z) \equiv \frac{e^z + e^{-z}}{2} = \cosh(-z)$$

$$\tanh(z) \equiv \frac{\sinh(z)}{\cosh(z)}$$

$$\sinh(iz) = i\sin(z)$$

$$\cosh(iz) = \cos(z)$$

$$\cosh(z) = 1 + \frac{z^2}{2!} + \frac{z^4}{4!} + \frac{z^6}{6!} + \cdots = \sum_{n=0}^{\infty} \frac{z^{2n}}{(2n)!}$$

$$\sinh(z) = z + \frac{z^3}{3!} + \frac{z^5}{5!} + \frac{z^7}{7!} + \cdots = \sum_{n=0}^{\infty} \frac{z^{2n+1}}{(2n+1)!}$$

$$\cosh^2(z) - \sinh^2(z) = 1$$

$$\tanh\left(\frac{z}{2}\right) = \frac{\sinh(x) + i\sin(y)}{\cosh(x) + \cos(y)}$$

$$\coth\left(\frac{z}{2}\right) = \frac{\sinh(x) - i\sin(y)}{\cosh(x) - \cos(y)}$$

$$\sinh(2z) = 2\sinh(z)\cosh(z)$$

$$\cosh(2z) = 2\cosh^2(z) - 1 = 1 + 2\sinh^2(z)$$
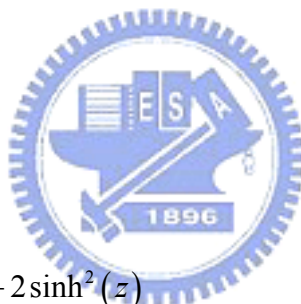
$$\sinh(z_1 + z_2) = \sinh(z_1)\cosh(z_2) + \cosh(z_1)\sinh(z_2)$$

$$\cosh(z_1 + z_2) = \cosh(z_1)\cosh(z_2) + \sinh(z_1)\sinh(z_2)$$

$$\sinh(x + jy) = \sinh(x)\cos(y) + i\cosh(x)\sin(y)$$

$$\cosh(x + jy) = \cosh(x)\cos(y) + i\sinh(x)\sin(y)$$

Appendix G   Properties of Material and Metals

Material	Dielectric Constant	Resistivetiy Ω-cm	$\tan\delta$ (25°C)	Thickness μm
Si Substrate	11.9	~10	0.004	~300

Metal	Resistivity Ω-cm	Normalized Skin Depth $\delta\sqrt{f}\times10^3\,\mu\,\text{in}$	Skin Depth δ @ 10 GHz $\times10^3\,\mu\,\text{in}$
Coppler	1.72	82	25.9
Silver	1.62	79.7	25.2
Gold	2.44	97	30.7
Aluminum	2.62	102.4	32.4
Nickel	7.4	164	52
Tantalum	13.5	244	77.2
Platinum	10.6	204	64.5
Vanadium	19.6	147.5	46.6
TIN	11.4		

About the Author

姓　名：曾聖哲

性　別：男

出生年月日：民國 69 年 12 月 28 日

籍　貫：台北

學　歷：國立交通大學 電信工程學系 學士 1999~2003

國立交通大學 電信工程學系 碩士 2003~

國立交通大學 電信工程學系 博士 2004~2008

獲　獎：

2008　　　　聯發科技獎學金(MediaTek Fellowship)

2003~2007　七次教育部獎學金

2004　　　　直升博士班

2003　　　　班上第一名畢業於國立交通大學電信系

2002~2003　大四代表學校到瑞典 Chalmers University of Technology 當交換學生，研修 Chalmers 碩士班課程

2001　　　　大三榮獲朱順一合勤獎學金

1999~2002　電信工程學系 書卷獎

經　歷：

交通大學	語音實驗室	工讀生	2001/02~2001/09	處理國語語音資料
交通大學	電信系	助教	2003/09~2004/01	類比積體電路課程助教
交通大學	電信系	助教	2004/02~2004/06	微算機實驗助教
交通大學	電信系	助教	2004/07~2004/08	電磁學暑修課程助教
交通大學	電信系	助教	2004/09~2005/01	數位訊號處理實驗助教
交通大學	培訓班	實驗課助教	2004/09~2004/11	教授射頻積體電路實驗課
交通大學	電信系	助教	2005/09~2006/01	數位訊號處理實驗助教
交通大學	培訓班	實驗課助教	2005/09~2005/11	教授射頻積體電路實驗課

Publication List

（A）Significant Journal

[1] **<u>Sheng-Che Tseng</u>**, Chinchun Meng, and Yueh-Ting Lee, "Dual-band adjustable and reactive I/Q generator with constant resistance for down- and up-converters," *IEEE Trans. Microw. Theory Tech.*, vol. 56, no. 8, pp. 1861-1868, Aug. 2008. (Full Paper)

[2] **<u>Sheng-Che Tseng</u>**, Chinchun Meng, Chia-Hung Chang, Shih-Hsien Chang and Guo-Wei Huang, "A silicon monolithic phase-inverter rat-race coupler using spiral coplanar striplines and its application in a broadband Gilbert mixer," *IEEE Trans. Microw. Theory Tech.*, vol. 56, no. 8, pp. 1879-1888, Aug. 2008. (Full Paper)

[3] Tzung-Han Wu, **<u>Sheng-Che Tseng</u>**, Chinchun Meng, and Guo-Wei Huang, "GaInP/GaAs HBT sub-harmonic Gilbert mixers using stacked-LO and leveled-LO topologies," *IEEE Trans. Microw. Theory Tech.*, vol. 55, no. 5, pp. 880-889, May. 2007. (Full Paper)

[4] **<u>Sheng-Che Tseng</u>**, Chinchun Meng, Chia-Hung Chang, Chih-Kai Wu and Guo-Wei Huang, "Monolithic broadband Gilbert micromixer with an integrated Marchand balun using standard silicon IC process," *IEEE Trans. Microw. Theory Tech.*, vol. 54, no. 12, pp. 4362-4371, Dec. 2006. (Full Paper)

[5] C. C. Meng, Y. W. Chang and **<u>S. C. Tseng</u>**, "4.9 GHz low-phase-noise transformer-based superharmonic-coupled GaInP/GaAs HBT QVCO," *IEEE Microw. Wirel. Compon. Lett.*, vol. 16, no. 6, pp. 339-341, Jun. 2006.

（B）International Journal

[1] **<u>S.-C. Tseng</u>**, C. C. Meng, H.-Y. Liao, Y.-C. Lin, and Y.-H. Teng, "Interconnection loss from substrate effects on LNA performance and design accuracy," *MICROWAVE AND OPTICAL TECHNOLOGY LETTERS*, vol. 51, no. 1, pp. -, Jan. 2009.

[2] **<u>Sheng-Che Tseng</u>**, Chinchun Meng, and Guo-Wei Huang, "Seven GHz high gain 0.18 μm CMOS Gilbert downconverter with wide-swing cascode current mirrors," *MICROWAVE AND OPTICAL TECHNOLOGY LETTERS*, vol.50, no.2, pp. 453-457, Feb. 2008.

[3] **<u>S.-C. Tseng</u>**, C. C. Meng and C.-K. Wu, "GaInP/GaAs HBT wideband transformer Gilbert downconverter with low voltage supply," *Electronics Letters*, vol. 44, no. 2, pp. 127-128, Jan. 2008.

[4] **<u>S.-C. Tseng</u>**, C. C. Meng, and G.-W. Huang, "SiGe BiCMOS sub-harmonic Gilbert mixer using lumped-element rat-race couplers," *MICROWAVE AND OPTICAL TECHNOLOGY LETTERS*, vol. 49, no. 8, pp. 2018-2020, Aug. 2007.

[5] **S. C. Tseng**, C. C. Meng, Y. W. Chang, and G. W. Huang, "C-band fully integrated SiGe HBT superharmonic QVCO," *MICROWAVE AND OPTICAL TECHNOLOGY LETTERS*, vol. 49, no. 4, pp. 867-869, Apr. 2007.

[6] C. C. Meng, **S. C. Tseng**, Y. W. Chang, J. Y. Su, and G. W. Huang, "Low-phase-noise transformer-based top-series QVCO using GaInP/GaAs HBT technology," *MICROWAVE AND OPTICAL TECHNOLOGY LETTERS*, vol. 49, no. 1, pp. 215-218, Jan. 2007.

[7] **Sheng-Che Tseng**, Chinchun Meng and Guo-Wei Huang, "A 2.4, 5.2 and 5.7 GHz CMFB Gilbert downconverter with low voltage cascode current mirror input stage," *MICROWAVE AND OPTICAL TECHNOLOGY LETTERS*, vol. 48, no. 11, pp. 2345-2349, Nov. 2006.

[8] Jen-Yi Su, Chinchun Meng, Yang-Han Li, **Sheng-Che Tseng**, and Guo-Wei Huang, "Gain enhancement techniques for CMOS LNA and mixer," *MICROWAVE AND OPTICAL TECHNOLOGY LETTERS*, vol. 48, no. 10, pp. 2067-2070, Oct. 2006.

[9] **Sheng-Che Tseng**, Chinchun Meng, Shao-Yu Li, Jen-Yi Su and Guo-Wei Huang, "Single-ended frequency divider with moduli of 256~271," *MICROWAVE AND OPTICAL TECHNOLOGY LETTERS*, vol. 48, no. 10, pp. 2096-2100, Oct. 2006.

[10] **S. C. Tseng**, C. C. Meng and W. Y. Chen, "SSH and SHH GaInP/GaAs HBT divide-by-3 prescalers with true 50% duty cycle," *Electronics Letters*, vol. 42, no. 14, pp. 796-797, Jul. 2006.

[11] **Sheng-Che Tseng**, Chinchun Meng, and Wei-Yu Chen, "True 50% duty-cycle SSH and SHH SiGe BiCMOS divide-by-3 prescalers," *IEICE Trans. Electron.*, vol.E89-C, no. 6, pp. 725-731, Jun. 2006. (Full Paper)

[12] **Sheng-Che Tseng**, Chinchun Meng, Yang-Han Li and Guo-Wei Huang, "The port-to-port isolation of the downconversion p-type micromixer using different n-well topologies," *IEICE Trans. Electron.*, vol.E89-C, no. 4, pp. 482-487, Apr. 2006. (Full Paper)

[13] **S.-C. Tseng**, C. C. Meng, W.-Y. Chen, and J.-Y. Su, "A modified HICUM model for GaInP/GaAs HBT devices," *MICROWAVE AND OPTICAL TECHNOLOGY LETTERS*, vol. 48, no. 4, pp. 780-783, Apr. 2006.

[14] Chinchun Meng, Bo-Chen Tsou and **Sheng-Che Tseng**, "Determining GaInP/GaAs HBT device structure by dc measurements on a two-emitter HBT device and high frequency transit time measurements," *IEICE Trans. Electron.*, vol.E88-C, no. 6, pp. 1127-1132, Jun. 2005. (Full Paper)

（C）Significant Conference

[1] Chinchun Meng, Jin-Siang Syu, **Sheng-Che Tseng**, Yu-Wen Chang, and Guo-Wei Huang, "Low-phase-noise SiGe HBT VCOs using trifilar-transformer feedback," *IEEE MTT-S 2008*, pp. 249-252, Jun. 15-20, 2008.

[2] **Sheng-Che Tseng**, Chinchun Meng, and Guo-Wei Huang, "High gain CMOS Gilbert downconverter with wide-swing cascode current-mirror transconductor and Load," *IEEE AP-S 2007*, pp. 4513-4516, Jun. 10-15, 2007.

[3] **Sheng-Che Tseng**, Chinchun Meng, Chia-Hung Chang, and Guo-Wei Huang, "SiGe HBT Gilbert downconverter with an integrated miniaturized Marchand balun for UWB applications," *IEEE MTT-S 2007*, pp. 2141-2144, Jun. 3-8, 2007.

[4] **Sheng-Che Tseng**, Chinchun Meng, Chih-Kai Wu, and Guo-Wei Huang, "Low-voltage GaInP/GaAs HBT wideband Gilbert downconverter using transformer RF balun," *IEEE MTT-S 2007*, pp. 2149-2152, Jun. 3-8, 2007.

[5] **Sheng-Che Tseng**, Chinchun Meng, Chia-Hung Chang, Chih-Kai Wu and Guo-Wei Huang, "Broadband Gilbert micromixer with an LO Marchand balun and a TIA output buffer," *IEEE MTT-S 2006*, pp. 1509-1512, Jun. 11-16, 2006.

[6] C. C. Meng, **S. C. Tseng**, Y. W. Chang, J. Y. Su and G. W. Huang, "4-GHz low-phase-noise transformer-based top-series GaInP/GaAs HBT QVCO," *IEEE MTT-S 2006*, pp. 1809-1812, Jun. 11-16, 2006.

（D）International Conference

[1] Chinchun Meng and **Sheng-Che Tseng**, "Integrating passive components with active circuits using standard silicon process for millimeter-wave applications," *GSMM'2008*, pp. 333-336, Apr. 21-24, 2008. (Invited Paper)

[2] **Sheng-Che Tseng** and Chinchun Meng, "10-GHz 0.35-μm SiGe BiCMOS bottom-LO-sub-harmonic Gilbert mixer with lumped-element rat-races," *APMC'06*, Dec. 13, 2006.

[3] **S. C. Tseng**, C. C. Meng, Y. W. Chang, and G. W. Huang, "4-GHz fully monolithic SiGe HBT QVCO using superharmonic coupling topology," *EuMIC 2006*, pp. 161-164, Sep. 12, 2006.

[4] **ShengChe Tseng**, Chinchun Meng, Shao-Yu Li, Jen-Yi Su, and Guo-Wei Huang, "2.4 GHz divide-by-256~271 single-ended frequency divider in standard 0.35-μm CMOS technology," *APMC'2005*, vol. 2, pp. 856-859, Dec. 4-7, 2005.

[5] **Sheng-Che Tseng**, Chinchun Meng, Wei-Yu Chen, and Jen-Yi Su, "A physics-based transit time model for GaInP/GaAs HBT devices," *APMC'2005*, vol. 2, pp. 1031-1034, Dec. 4-7, 2005.

[6] Jen-Yi Su, Chinchun Meng, Yang-Han Li, **Sheng-Che Tseng**, and Guo-Wei Huang, "2.4 GHz 0.35 μm CMOS single-ended LNA and mixer with gain enhancement techniques," *APMC'2005*, vol. 3, pp. 1550-1553, Dec. 4-7, 2005.

[7] **<u>Sheng-Che Tseng</u>**, C.C. Meng and G.W. Huang, "A C band downconversion Gilbert mixer with improved single-to-differential RF transconductance stage and active IF loads," *APMC'04*, APMC/04/C/483, Dec. 15-18, 2004.